DOCTORAL THESIS

Observational and Modeling Studies of Charge Exchange X-ray Emission Associated with the Earth's Magnetosphere

A thesis submitted in partial fulfillment of the requirements
for the degree of Doctor of Philosophy
by

Daiki ISHI

Department of Physics
Graduate School of Science
Tokyo Metropolitan University

February 20, 2023

Abstract

Highly charged solar wind ions such as O^{7+} produce soft X-rays via charge exchange with neutral materials in the Earth's exosphere or geocorona (mainly H atoms). This phenomenon is called geocoronal solar wind charge exchange (SWCX). All the soft X-ray observations from Earth-orbiting satellites must contend with a persistent foreground emission from geocoronal SWCX. However, it remains difficult to predict some observational properties such as time series and overall flux levels for arbitrary spacecraft look directions. Making the most of instrumental and orbital advantages, we analyzed five Suzaku detections of bright geocoronal SWCX events. For each observation, we selected regions outside astronomical source(s) and extracted X-ray light curves in the 0.5–0.7 keV band. A clear enhancement significantly correlated with solar wind fluxes measured by WIND and ACE satellites. The enhanced spectra contained six emission lines from C, N, and O. Some minor emission lines from Ne, Mg, and Si were also detected. The strongest oxygen emission lines, i.e., O VII and O VIII, showed intensities of several tens of photons s^{-1} cm^{-2} str^{-1}. Then, combining an exospheric neutral hydrogen distribution model, charge exchange cross sections, solar wind data taken with WIND and ACE satellites, and Earth's magnetic field models, we built an empirical model of geocoronal SWCX emission. The sum of model uncertainties was a factor of 3–5. The modeled average intensities of O VII emission lines were consistent with the observed ones within a factor of three except for an event probably affected by solar wind injections during intense geomagnetic storms. Those of O VIII emission lines were underestimated by a factor of three or more. Unknown systematic uncertainties might exist in solar wind data that describe highly stripped ion states. The modeled O VII and O VIII light curves after scaling were consistent with the observed ones including some spike behaviors due to line-of-sight directions passing through polar cusps during an orbital motion. Our model can provide a new estimation of geocoronal SWCX emission including light curves for future X-ray astronomy missions as well as X-ray imaging missions of the Earth's magnetosphere.

Contents

List of Figures

List of Tables

Chapter 1

Introduction

Thanks to the progress of science and technology, people have launched many rockets and satellites to explore and utilize space around the Earth. The near-Earth space is called “geospace.” Human activities using geospace have become necessary since the mid-20th century. For example, space-based infrastructures such as meteorological satellites for weather forecasts and global positioning satellites for navigation systems are essential for our daily lives.

The Earth is continuously exposed to solar particles accelerated from a few tens of keV up to GeV energies and solar radiation ranging from radio waves to γ-rays. These particles and radiation would damage our bodies when directly hitting us. The Earth’s magnetosphere shields us from such direct attacks but varies spatially and temporally depending on solar activities, e.g., solar flares and coronal mass ejections (CMEs). Astronauts aboard the International Space Station are always alert to occurrences of such phenomena. While the sphere of our activities is about to expand from geospace to cislunar space, e.g., the Lunar Orbital Platform-Gateway (formerly known as the Deep Space Gateway), space weather involving various natural and artificial phenomena such as active auroras, satellite communication blackouts, and spacecraft malfunctions has become critical for our future deep space activities.

Exploration satellites have been launched from the United States, Europe, and Japan since the beginning of the space age in the 1960s. Most knowledge about solar-terrestrial interactions has been revealed through collections of in-situ observations by individual spacecrafts. These observations do not provide a global view to investigate overall interaction processes, e.g., transport routes of solar wind plasma and energies during geomagnetic storms, but a statistical picture of such processes. The global dynamics of the Earth's magnetosphere are not well known due to technical challenges of simultaneous observations by multiple spacecrafts at multiple positions. If covering such global scales, more than hundreds of formation flight satellites would be needed.

Remote sensing makes it possible to take global images of various magnetospheric phenomena. The mapping of ultraviolet (UV) auroral ovals provides spatial and temporal information on precipitation particles along magnetic field lines. Extreme ultraviolet (EUV) images visualize a torus of cold and dense plasma surrounding the Earth. The imaging of the Earth's plasmasphere was first demonstrated by the EUV scanner onboard the first Japanese Mars explorer Nozomi. Energetic neutral atoms (ENAs) trace energetic ring current ions in the Earth's magnetosphere. These imaging techniques have contributed to magnetospheric studies as means of complementing in-situ measurements of particles and electromagnetic fields. In recent years, X-ray astronomical observations have attracted much attention from solar-terrestrial researchers as a novel method to study global magnetospheric activities.

The history of X-ray astronomy began in 1962 with a rocket experiment by Dr. Riccardo Giacconi, Nobel laureate known as the "father of X-ray astronomy." This experiment first intended to investigate scatted solar X-rays on the Moon but serendipitously detected X-rays from Scorpius X-1, the brightest X-ray source in the entire sky, leading to the birth of X-ray astronomy. To date, during the past 60 years, millions of astronomical objects emitting X-rays have been detected. Among these objects, comet Hyakutake (C/1996 B2) is one of the most surprising discoveries in the history of X-ray astronomy. This object taught us that X-rays are produced not only in "hot" objects, with temperatures often higher than 10^6 K, but also in "cold" objects like comets due to "charge exchange."

Charge exchange occurs anywhere "hot" plasma comes into contact with "cold" materials, i.e., it is a ubiquitous phenomenon from the nearby solar system to the distant universe. The strong Coulomb force of highly charged ions can strip an electron from neutral atoms or molecules. The electron first enters into an excited state but soon cascades to the ground state through all possible transitions, thereby producing emission lines in the EUV to soft X-ray regime. This process is characterized by a large cross section on the order of 10^{-16} cm^{-2}, which is about four orders of magnitude larger than that of ion-ion Coulomb collisions, thus enabling us to probe plasma-neutral interactions, e.g., tenuous atmospheres surrounding comets, moons, and planets.

The Earth's exosphere or geocorona is undergoing charge exchange with solar winds blowing through the Earth's magnetosphere (generally called geocoronal solar wind charge exchange, SWCX). The hydrogen geocorona has a typical density of $\sim$25 cm^{-3} at 10 Earth radii (R_{E}) and extends well beyond the orbit of the Moon ($\sim$60 R_{E}). The Earth's magnetosphere is formed as a consequence of interactions between solar wind particles and Earth's magnetic fields. Global X-ray imaging of geospace using charge exchange emitters gives us new views of physical phenomena taking place in the Earth's magnetosphere and exosphere.

Geocoronal SWCX is important not only for solar-terrestrial communities but also for X-ray astronomers because it is a persistent foreground emission and contaminates signals of interest for all the soft X-ray observations from spacecrafts orbiting around the Earth. A prime example is temporally enhanced backgrounds with time scales of several hours to a couple of days (dubbed "long-term enhancements," LTEs) during the German X-ray astronomy satellite ROSAT all-sky survey observations in the 1990s. The LTEs remained a mystery for several years. Shortly after the Hyakutake observation, its origin was soon recognized as geocoronal SWCX.

Since the 2000s, numerous geocoronal SWCX events have been reported by other X-ray astronomy satellites sensitive to soft X-rays (e.g., Chandra, XMM-Newton, and Suzaku). This emitter is an astrophysical nuisance but its nature is still unclear due to its closeness. Figure 1.1 shows a schematic view of geocoronal SWCX.

In this thesis, making the most of instrumental and orbital advantages, we analyze Suzaku observations of bright geocoronal SWCX events and build an empirical model to predict some observational properties such as time series and overall flux levels for

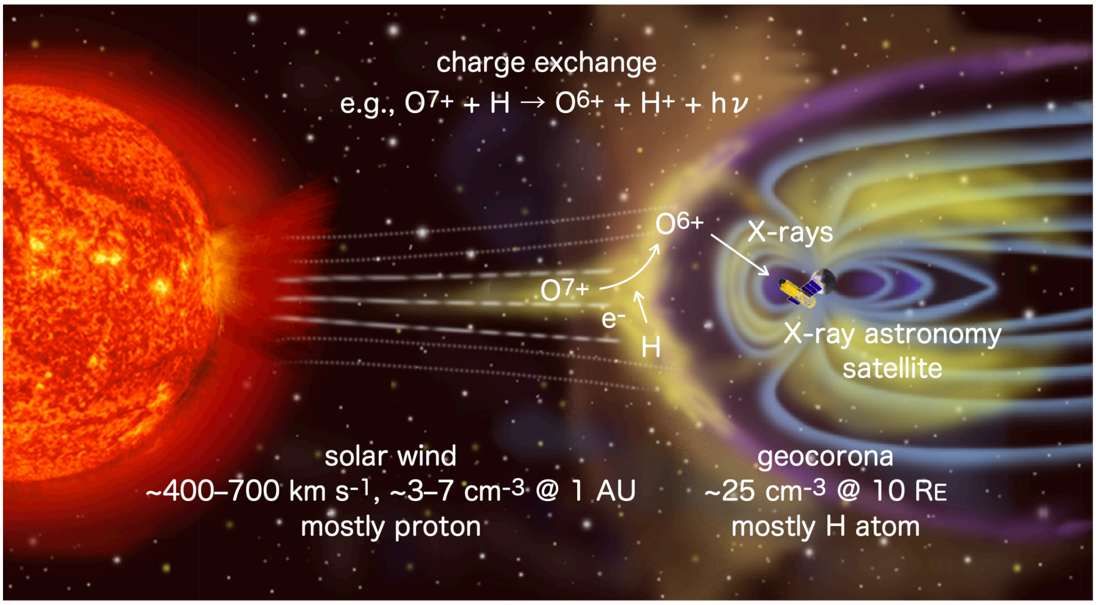

FIGURE 1.1: Schematic view of geocoronal SWCX. The spatial scale is arbitrary. The bright yellow area represents a region where solar wind particles are concentrated through collisions with Earth's magnetosphere (typically located at $\sim$10 R_{E}). It is believed that, mainly in this region, highly charged solar wind ions, e.g., O^{7+}, emit soft X-rays due to charge exchange with hydrogen atoms in Earth's geocorona.[1]

arbitrary spacecraft look directions. We believe that the results described in this thesis are quite valuable not only for X-ray astrophysics but also for solar-terrestrial physics.

---

[1] The illustration is cited from the following website: `https://sci.esa.int/web/cluster/-/41473-solar-wind-hits-earth-s-magnetosphere`.

Chapter 2

Review

This chapter gives descriptions of charge exchange and geocoronal SWCX.

2.1 Charge exchange

Charge exchange (also known as charge transfer) is a fundamental process in atomic physics. The process itself has been studied in various contexts for a long time. There are two main features. One is a large cross section which is several orders of magnitude larger than those of other collisional excitation processes. The other is a characteristic line emission at X-ray energies. Charge exchange is a newcomer to X-ray astrophysics and has attracted much attention as a new-type emission mechanism in a variety of X-ray sources, e.g., solar system objects, starburst galaxies, and supernova remnants. This section describes the principle and observational sites of charge exchange.

2.1.1 Principle

The basic principle of charge exchange is very simple. One or more electrons are transferred from an atom or molecule to an ion. Similar reactions occur between ions but its cross section is very small due to Coulomb repulsion. The ion is referred to as the "projectile" because it usually moves faster than the neutral "target." The reaction can be written symbolically as

$$A^{q+} + B \rightarrow A^{(q-r)+} + B^{(r+s)+} + se^{-}, \tag{2.1}$$

where $r + s$ electrons are lost from the neutral target B, r electrons are captured by the projectile ion A with charge q, and s electrons are lost to the continuum.

At collision energies below ~1–5 keV/atomic mass unit (u), which is typical solar wind speeds, single-electron capture, i.e., $(r, s) = (1, 0)$, is dominant in most collisional systems. The electron can be captured into an excited state of the product ion. The excited state decays to the ground state or through some lower excited states with photon emission. That is

$$A^{q+} + B \rightarrow A^{(q-1)+^{*}} + B^{+}, \tag{2.2}$$

and then

$$A^{(q-1)+^{*}} \rightarrow A^{(q-1)+} + h\nu. \tag{2.3}$$

When the neutral target has more than one electron, i.e., other than atomic hydrogen, multiple electrons may be transferred. In particular, two-electron processes, e.g., $(r, s) = (2, 0)$ and $(1, 1)$, can be important. The former process (known as true double capture) produces a doubly excited ion that can be either radiatively stabilized or autoionized. The probability for autoionization by ejecting an Auger electron,

$$A^{(q-2)+^{**}} \rightarrow A^{(q-1)+^{*}} + e^{-}, \tag{2.4}$$

is usually larger than that for radiative stabilization, resulting in the final state of the latter process, i.e., $(r, s) = (1, 1)$, via an indirect route.

For a detailed theoretical description of charge exchange, several approximation techniques have been developed. The most basic approach is the classical over-barrier (COB) model (Ryufuku and Watanabe, 1979), which is appropriate for collision energies in the range of 100 eV/u up to 10 keV/u. It allows us to estimate an electron capture cross section σ and a principal quantum number n into which the electron is captured. This model describes single-electron capture given in Equation 2.2.

The basic idea is shown in Figure 2.1. When a projectile ion is far enough away from a neutral target, a barrier exists between Coulomb-like potentials created by each nucleus. This barrier gradually falls as the two particles approach each other. When it drops down into a binding energy of an electron on the target side, the electron bound to the target can cross over to the other side. Such a joint potential well is called a quasi-molecular state. When the projectile ion is highly charged, the ground state is much lower than that of the target so that the energy level on the recipient side is quite high.

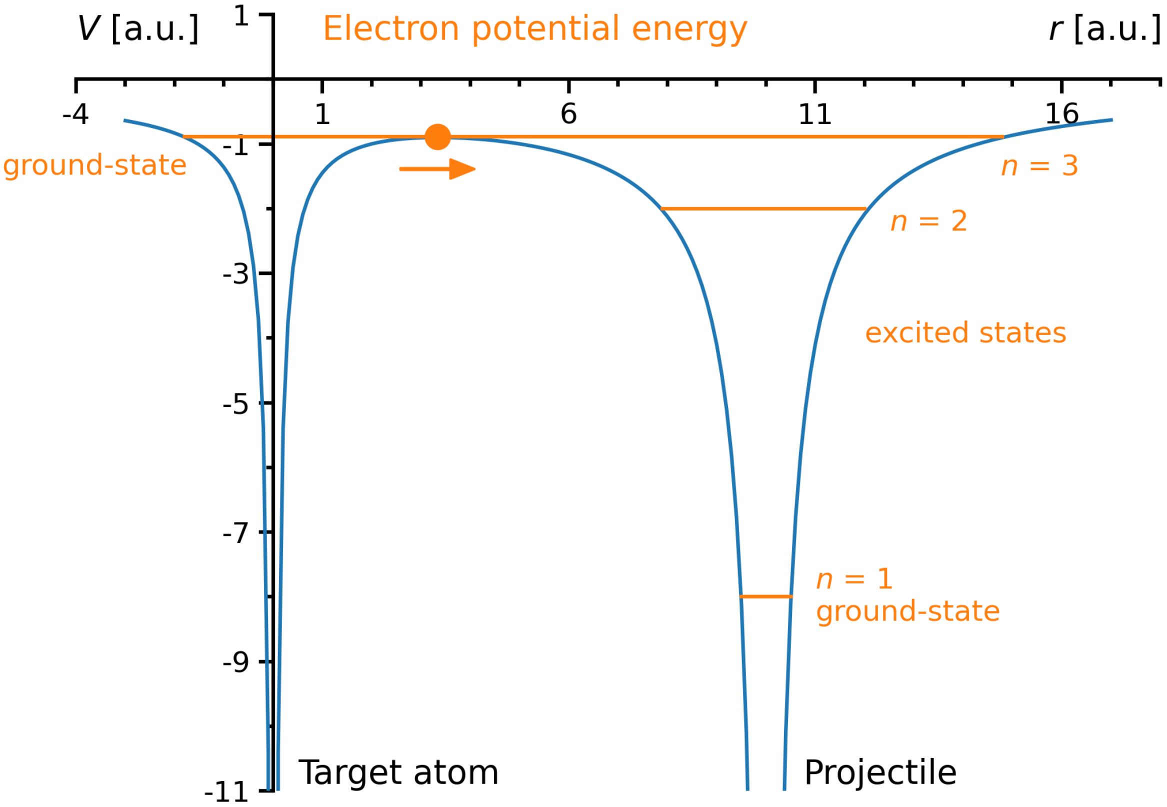

FIGURE 2.1: Electron potential energy V in atomic units (a.u.) versus distances from the nucleus of a target atom B (assumed to be atomic hydrogen) for charge exchange process involving a projectile ion A^{q+} (calculated for Be^{4+}). The inter-nuclear distance of 10 a.u. (1 a.u. $=$ 1 Bohr radius $=$ 5.29×10^{-11} m) is the curve-crossing distance for the $n = 3$ state. The target and product ion (Be^{3+}) energy levels are shown (1 atomic energy unit $=$ 1 hartree $=$ 27.2 eV). The electron can be transferred from the target to the projectile for the favored principal quantum number ($n \approx 3$).[1]

---

[1] The energies of an atomic species with a nuclear charge Z and a principal quantum number n for just one electron are given by the Bohr energy expression: $E_n = -\mathrm{Ry}(Z^2/n^2)$, where Ry is the Rydberg

A step-by-step process of charge exchange can be explained by considering an electron undergoing the following steps. The atomic unit system is used so that the charge and mass of the electron along with the Coulomb constant are set to unity. At an infinite separation, an electron bound to a neutral target has a negative binding energy I_b. As a projectile ion approaches the target, the binding energy of the electron is increased by a Stark shift which is due to the approach of a Coulomb field of the ion:

$$I_\mathrm{b}(R) = I_\mathrm{b}(\infty) - \frac{q}{R}, \tag{2.5}$$

where R is the separation between the projectile ion and the target, and q is the charge of the ion. An electron at a distance r from the target nucleus experiences a total potential energy V, which is the sum of the potential of the ion and that of the target:

$$V(r) = -\frac{q}{|R-r|} - \frac{1}{|r|} \quad \text{for} \quad 0 < |r| < |R|. \tag{2.6}$$

The top of the potential barrier between the ion and the target is reached at a certain distance r_max where the derivative of the potential $V(r)$ is zero:

$$\frac{\mathrm{d}V(r)}{\mathrm{d}r} = -\frac{q}{(R-r)^2} + \frac{1}{r^2} = 0. \tag{2.7}$$

Solving the above equality yields both the distance r_max and the potential V_max:

$$\begin{aligned} r_\mathrm{max} &= \frac{R}{\sqrt{q}+1}, & (2.8) \\ V_\mathrm{max} &= -\frac{q}{R} - \frac{2\sqrt{q}+1}{R} = -\frac{(\sqrt{q}+1)^2}{R}. & (2.9) \end{aligned}$$

---

constant. According to the above equation, a ground state energy for atomic hydrogen ($Z = 1$) is -13.6 eV, while that for Be^{3+} ($Z = 4$) is 16 times for atomic hydrogen, i.e., -217.6 eV.

The electron can be transferred from the target to the ion when the potential V_{max} is smaller than the binding energy of the electron:

$$-\frac{q}{R} - \frac{2\sqrt{q}+1}{R} = I_{\mathrm{b}}(\infty) - \frac{q}{R}, \tag{2.10}$$

which yields a critical distance R_{c} at which charge exchange can occur:

$$R_{\mathrm{c}} = \frac{2\sqrt{q}+1}{-I_{\mathrm{b}}(\infty)}. \tag{2.11}$$

A cross section of charge exchange can be determined by assuming that the electron is captured if the projectile ion passes through the target at a distance smaller than the critical distance R_{c}:

$$\sigma = \pi R_{\mathrm{c}}^2 = \pi \left(\frac{2\sqrt{q}+1}{I_{\mathrm{b}}(\infty)} \right)^2 . \tag{2.12}$$

This cross section should be weighted with the probability where charge exchange occurs, i.e., the electron either stays with the target or moves to the ion. The probability is about 50%.

In the COB model, it is assumed that the binding energy of the electron remains fixed during the quasi-molecular state. As the projectile ion moves away from the target, the potential barrier increases again. The binding energy I_{f} of the captured electron is lowered by a Stark shift induced by the charged target:

$$I_{\mathrm{f}} = I_{\mathrm{b}}(R_{\mathrm{c}}) + \frac{1}{R_{\mathrm{c}}} = I_{\mathrm{b}}(\infty) - \frac{q-1}{R_{\mathrm{c}}}. \tag{2.13}$$

The captured electron has a higher binding energy and is placed in a high energy level of the ion with charge $q-1$. The energy level n where an electron is most likely to be captured can be predicted by converting the binding energy I_{f} into a "classical" energy level n_{cl} based on the hydrogenic approximation:

$$n_{\mathrm{cl}} = \frac{q}{\sqrt{|2I_{\mathrm{f}}|}}. \tag{2.14}$$

A cartoon of a collision between a hydrogen-like O^{7+} ion and a hydrogen atom is shown in Figure 2.2. In the initial state, an electron is bound in the target atom with a binding energy of $I_{\mathrm{b}}(\infty) = -13.6$ eV. At an inter-nuclear distance of $R_{\mathrm{c}} = 12.6$ a.u. ($\sim$6.7 Å), which is equivalent to a cross section of 70×10^{-16} cm^{-2}, the electron can cross a potential barrier between the two particles. The binding energy of the electron in the quasi-molecular state is $I_{\mathrm{b}}(R_{\mathrm{c}}) = -26.6$ eV. Upon a separation, the final binding energy of that in the projectile ion is $I_{\mathrm{f}} = -24.6$ eV. Following Equation 2.14, this results in $n_{\mathrm{cl}} = 5.2$. The most likely principal quantum shell into which the electron is captured is $n = 5$.

Even more than the n-distribution, an angular momentum l-distribution is important for a hydrogen-like spectrum resulting from charge exchange between a fully-stripped ion such as O^{8+} and a neutral target (Otranto et al., 2006). At low energies below $\sim$1 keV/u, the l-distribution peaks around $l = 1$, from which a high-n electron can decay directly to the ground state, thereby yielding a strongly enhanced high-n Lyman photon. On the other hand, at higher energies, higher l-states are preferentially populated. The l-distribution is statistically weighted by $2l + 1$ with a maximum value of $l_{\mathrm{max}} = n - 1$. The electron captured into such high-l states can not decay directly to the ground state because of the $\Delta L = \pm 1$ selection rule. It cascades through the lowest n levels permitted by the selection rules. In most cases, the first decay begins at an l_{max} state, i.e., a maximum angular momentum state for the given n level, from which the electron cascades in steps of $\Delta n = \Delta l = -1$ (known as a "yrast cascade"),[2] finally yielding Lyα photons. High-n Lyman lines become weak.

Helium-like spectra resulting from charge exchange of hydrogen-like ions are more

---

[2] Yrast is the superlative of the Swedish word, yr, which means "whirlingest" or "dizziest." In atomic and nuclear physics, it refers to the largest angular momentum for a given principle quantum number. An example of a yrast cascade is $5g \rightarrow 4f \rightarrow 3d \rightarrow 2p \rightarrow 1s$ (Wargelin et al., 2008).

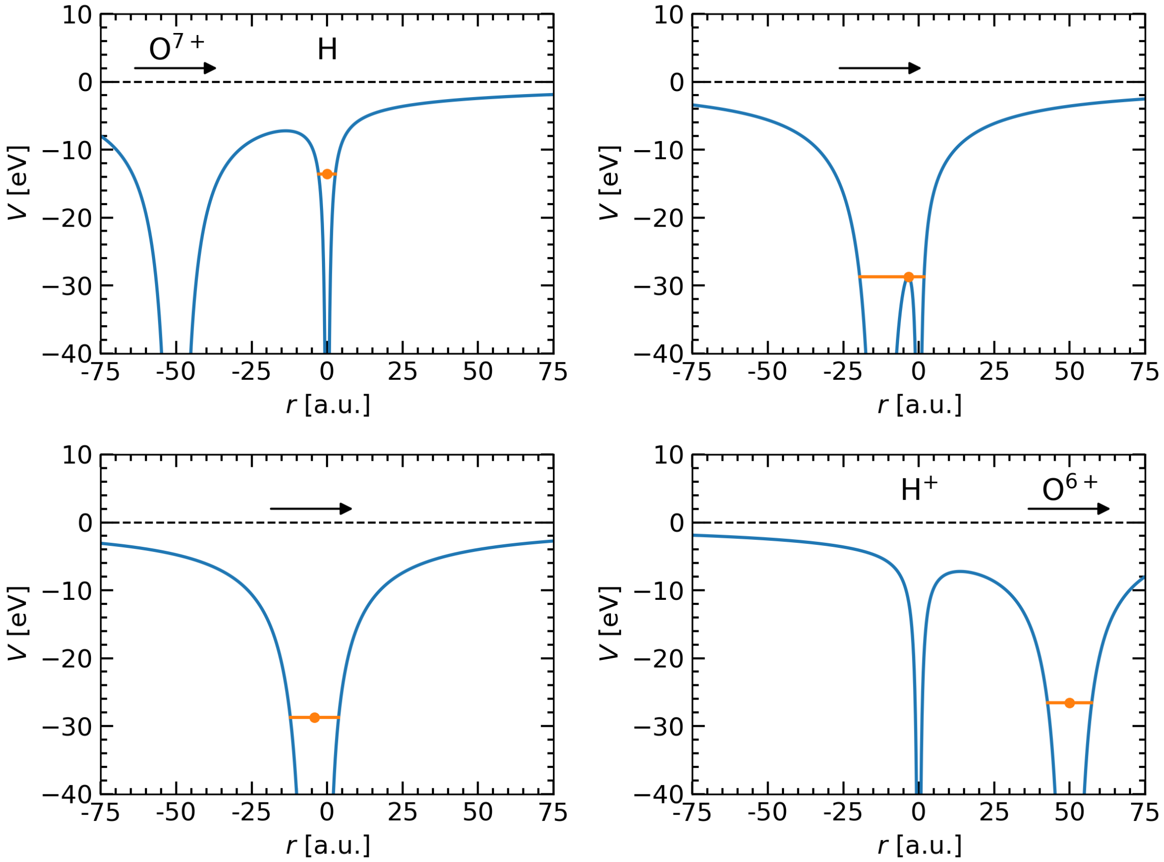

FIGURE 2.2: The COB model for a hydrogen-like O^{7+} ion colliding with a hydrogen atom. Upper left panel: The projectile ion approaches the target atom. The potential barrier is lowered when the two particles approach each other. Upper right panel: At an inter-nuclear distance, the potential barrier becomes lower than the binding energy of the outermost electron of the target atom. Lower left panel: The electron is in a quasi-molecular state. Lower right panel: The quasi-molecular electron is either captured by the projectile ion or recaptured by the target atom.

complicated than hydrogen-like spectra because of the spins of the two electrons in the resultant helium-like ion, which yields either a singlet ($S = 0$) or triplet ($S = 1$) state. From a statistical weight, a probability ratio is usually assumed to be 1:3. The decay of the singlet states is fundamentally the same as for hydrogen-like spectra, producing a strong $n = 2 \to 1$ line, strictly speaking the "resonance" (w, $1s2p\ {}^1P_1 \to 1s^2\ {}^1S_0$) line, and some high-$n$ K-series lines at low collision energies. On the other hand, none of the initial triplet states can decay directly to the ground state because of the $\Delta S = 0$ selection rule that forbids a mixture or "intercombination" of triplet and single states. A high-n electron cascades to one of the $n = 2$ triplet states, i.e., $1s2s\ {}^3S_1$ or $1s2p\ {}^3P_2$, ${}^3P_1$, and ${}^3P_0$, from which it falls back to the ground state through forbidden or quasi-forbidden transitions. The ${}^3P_2$ state can not decay to the ground state because of the $\Delta J = 0$ and ± 1 (but no $J = 0 \to 0$) selection rule. It usually decays to the ${}^3S_1$ state but sometimes decays to the ground state through the $\Delta J = \pm 2$ transition, which is an "intercombination" transition since it involves a change in S, producing the x line. The ${}^3P_1$ state can decay to the ground state through another "intercombination" transition, which stems from J coupling with the ${}^1P_1$ state, producing the y line. The ${}^3P_0$ state can not decay by single-photon emission because the $J = 0 \to 0$ transition is strictly prohibited. It thus translates to the ${}^3S_1$ state, which is the lowest energy level of the triplet states. This metastable state, i.e., ${}^3S_1$, falls back to the ground state by relativistic magnetic dipole emission, producing the "forbidden" (z, $1s2s\ {}^3S_1 \to 1s^2\ {}^1S_0$) line. The above four components constitute the Kα complex (often called the helium-like triplet, i.e., w, the often blended x and y, and z). Figure 2.3 shows an energy level diagram for a helium-like O^{6+} ion illustrating the forbidden, resonant, and intercombination lines for the $n = 2 \to 1$ transition. From a theoretical transition rate and an assumed population of the triplet states, a branching ratio between the forbidden and intercombination lines is roughly estimated to be 0.7:0.3. The forbidden line is the most prominent transition. These spectral features are quite different from those of direct excitation.

The COB model does not predict an exact distribution of the n-states and the l-levels of the resultant ion with charge $q - 1$. There are more complex theoretical models such

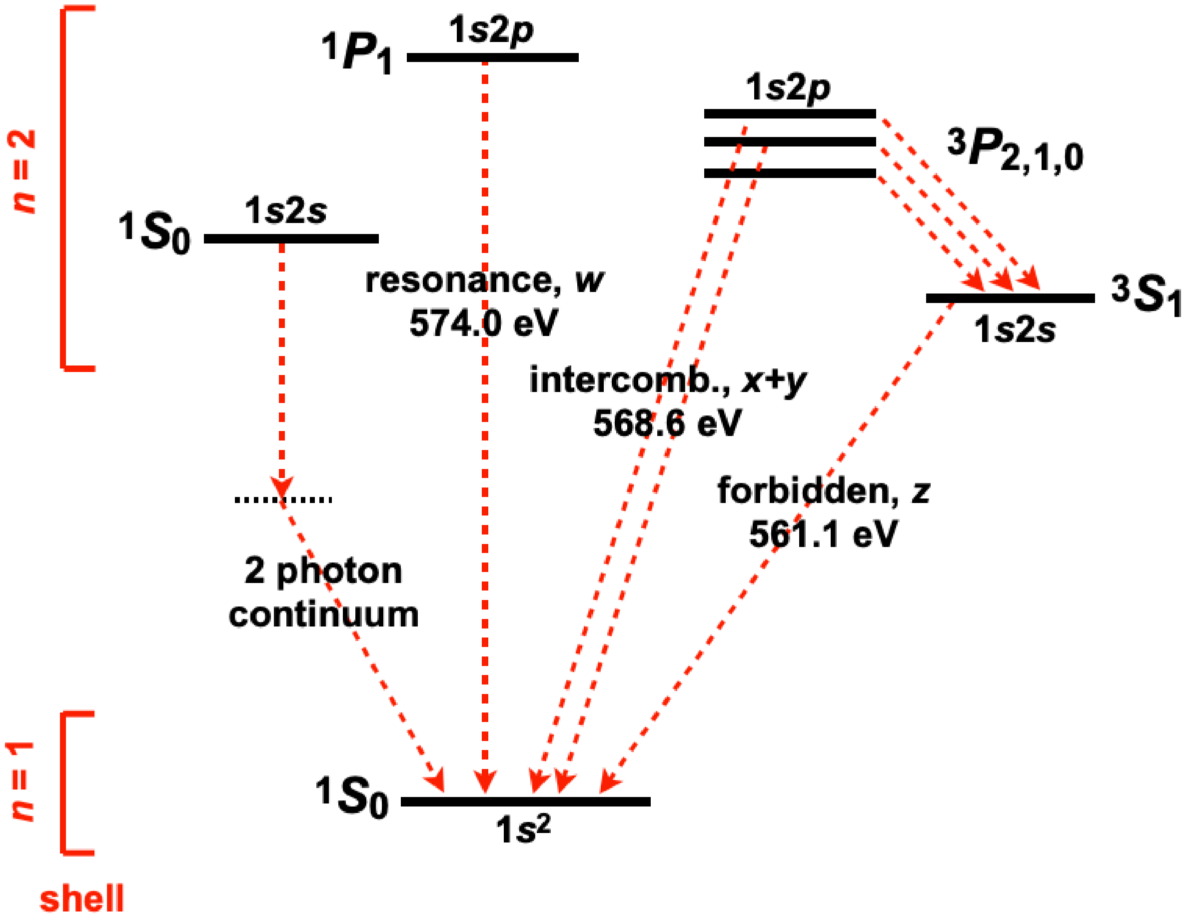

FIGURE 2.3: Schematic diagram of energy levels of a helium-like O^{6+} ion for the $n = 2 \rightarrow 1$ transition.

as the classical trajectory Monte Carlo technique and the Landau-Zener approximation. The quantum-mechanical close-coupling method is the most reliable theoretical approach but suffers from computational resources (Hasan et al., 2001). The Kronos model allows users to generate spectra for many collisional systems between projectile ions (e.g., H-like C, N, O, Ne, Mg, Al, and Si) and neutral targets (e.g., H, H_2O, CO, CO_2, OH, and O) at wide collision energies from 0.01 eV/u up to 100 keV/u.[3] Single-electron capture can be handled. The majority of them use the multichannel Landau-Zener method. Several collision systems provide more accurate results including recommended cross sections.

2.1.2 Observational sites

Charge exchange operates to produce soft X-rays when highly charged ions collide with neutral materials. Solar system objects provide ideal experimental sites for investigating charge exchange processes because detailed in-situ information on both ions and neutrals can be obtained. Below we describe several solar system charge exchange emitters.

Comets

A comet is a mixture of frozen H_2O, CO, CH_4, H_2CO, NH_3, and dust. The nucleus is only a few km in size. The mixture remains frozen when a comet is far from the Sun. The surface heats up and releases volatiles as a comet approaches the Sun. The vapor produced by the active nucleus extends far out into space ($\sim 10^4$–10^6 km). It becomes a cometary coma or atmosphere whose density is inversely proportional to the square of the cometocentric distance. The outflow atom and molecule undergo photodissociation or photoionization by solar radiation, producing various neutral and

---

[3] A series of python and fortran codes is available from the following website: `https://www.physast.uga.edu/research/stancil-group/atomic-molecular-databases/kronos`.

ionic species. Such gas carries large amounts of dust along with it. A so-called "visible" comet is sunlight reflected by the extensive dust coma and tail. Solar radiation pressure pushes dust grains anti-sunward.

Comet Hyakutake, first discovered on 1996 January 31, made the closest approach to Earth late in March of that year. It was a brightly shining comet in the night sky and was visible from many parts of the world. The German RÖentgen SATellite (ROSAT) observed comet Hyakutake with a surprising result (Lisse et al., 1996). The comet emitted a copious flux of soft X-rays. The image is shown in Figure 2.4. This result confused scientists because comets are not associated with hot plasma, energetic particles, and optically thick materials that scatter solar X-rays like the Moon. No satisfactory explanations were found at that time.

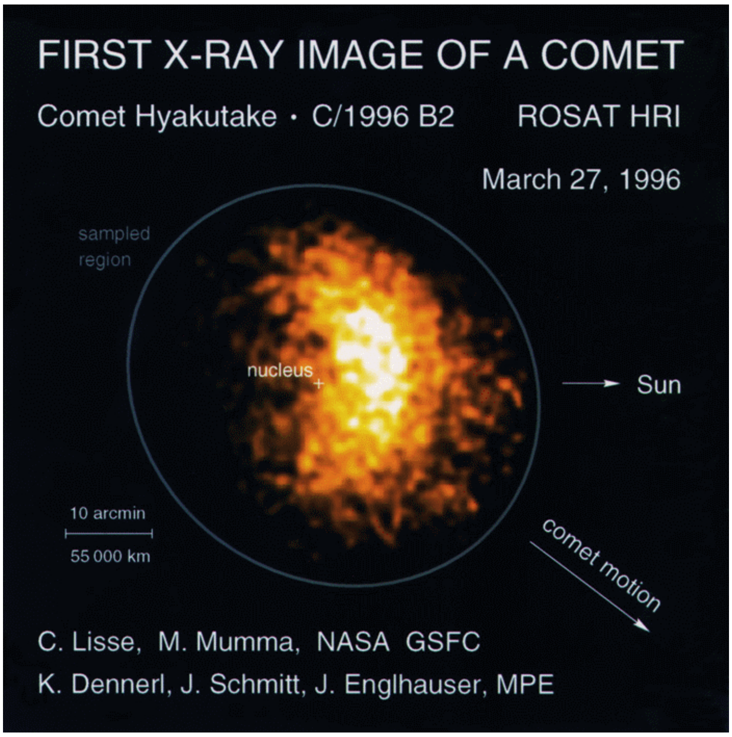

FIGURE 2.4: X-ray image of comet Hyakutake observed by the High Resolution Imager (HRI) onboard ROSAT. X-rays arise from a crescent-shaped region with a diameter of about 50,000 km on the sunlit side of the comet. The directions toward the Sun and of the comet motion are indicated by the arrows. No significant X-rays are detected from the nucleus marked by the "+" sign. The ellipse represents the instrument field of view.[4]

---

[4] The image is credited by C. Lisse, M. Numma (NASA/GSFC), K. Dennerl, J. Schmidt, and J. Englhauser (MPE): `https://heasarc.gsfc.nasa.gov/Images/rosat/hyakutake.gif`.

The mystery of comet Hyakutake was solved by Cravens (1997). He proposed that the observed soft X-ray emission is a superposition of numerous emission lines due to charge exchange between solar wind ions and cometary neutrals evaporating from its nucleus. The neutral species are mainly composed of H_2O and its dissociation products, e.g., H, OH, and O. The parent molecule, i.e., H_2O, has a short lifetime when exposed to solar UV radiation. Therefore, it can exist only inside, whereas its dissociation products can survive even outside. A high charge state ion abundance amounts to about 0.1% of solar wind densities but solar wind fluxes are relatively high so that its amount is enough to produce soft X-rays. The prediction based on experiences and knowledges of comets, solar winds, and atomic physics successfully reproduced most observed features, e.g., total luminosity and spatial morphology.

Since the first observation of comet Hyakutake, more than 20 comets have been detected with X-ray and EUV observations (Lisse et al., 2004; Krasnopolsky et al., 2004). Cometary X-ray spectra can be used as a probe for monitoring solar wind minor constituents. Their orbits are not restricted to an ecliptic plane and make them ideal experimental sites to investigate compositional signatures originating from various solar wind latitudes (Bodewits et al., 2007). Their spectral features tell us how and where comets are formed because charge exchange induced spectra depend not only on projectile solar wind ions but also on target cometary neutral species (Beiersdorfer et al., 2003; Mullen et al., 2017).

Mars

Chandra detected a faint X-ray halo around Mars (Dennerl, 2002). A high-resolution grating spectrum with XMM-Newton showed signs of emission lines from highly ionized C, N, O, and Ne (Dennerl et al., 2006). This halo originates from charge exchange between solar wind ions and Martin exospheric hydrogen atoms. The Martin exosphere has been investigated with several exploration satellites but its dependence on solar activities is not well known due to technical difficulties in measuring tenuous atmospheres. Suzaku observed Mars at solar minimum (Ishikawa et al., 2011). The past

Chandra and XMM-Newton observations of Mars were performed at solar maximum. Martian X-rays were so faint that it was not even detectable. This result presented an upper limit on Martin exospheric hydrogen distributions at solar minimum.

Venus

The observation of Venus is considerably more challenging. The angular separation of Venus from the Sun is too small for observations with Earth-orbiting satellites. The optical brightness of Venus is too much for X-ray observations. The first Chandra observation of Venus at solar maximum detected fluorescence of solar X-rays but no charge exchange signals were detectable (Dennerl et al., 2002). The second and third Chandra observations were performed at solar minimum (Dennerl, 2008). Fluorescent X-rays were practically absent but charge exchange fluxes were very low.

Jupiter

Chandra observed strong X-ray emission from Jovian aurora regions (Gladstone et al., 2002). A subsequent observation with XMM-Newton revealed its spectral features (Branduardi-Raymont et al., 2004). Bremsstrahlung of electrons precipitating from Jovian magnetosphere is responsible for X-ray emission above 2 keV. Charge exchange is an explanation for X-ray emission at lower energies. Highly charged ions could be supplied not only by solar wind ions but also by Jovian magnetospheric ones via acceleration and subsequent ionization of ambient sulfur and oxygen ions (Branduardi-Raymont et al., 2007). Suzaku detected Jovian diffuse hard X-ray emission due to inverse Compton scattering of solar photons by tens of MeV electrons around Jovian radiation belts (Ezoe et al., 2010a; Numazawa et al., 2019; Numazawa et al., 2021). There were some emission lines from carbon and oxygen ions as well as blended ones from highly ionized Mg, Si, and S. Most of them might originate from Jovian auroral charge exchange processes.

The Moon

Robertson et al. (2009) predicted soft X-ray intensities from charge exchange between solar winds and lunar exospheric neutrals. The predicted intensities are comparable to soft X-ray backgrounds but are strong enough to be observable from Earth. Collier et al. (2014) presented ROSAT observations of lunar limb brightening consistent with signals from lunar charge exchange predictions.

Heliosphere

ROSAT created all-sky soft X-ray maps as shown in Figure 2.5. Diffuse soft X-ray backgrounds are composed of many distinct components. The closest source is an irregularly shaped cavity filled with hot plasma of $\sim 10^6$ K. Cox (1998) proposed heliospheric solar wind plasma interacting with interstellar neutrals as another source of diffuse soft X-ray backgrounds. The entire heliosphere should be absolutely glowing in soft X-rays. Heliospheric charge exchange emitters account for about 25%–50% of the observed soft X-ray background (Cravens, 2000).

2.2 Geocoronal solar wind charge exchange (SWCX)

This section describes the Sun-Earth system and current status of observational and modeling studies of geocoronal SWCX.

2.2.1 The Sun-Earth system

Below we give brief descriptions of solar-terrestrial environment.

The solar wind

The Sun expels a huge amount of charged particles into interplanetary space. The mass loss rate reaches as high as 1×10^9 kg s^{-1} ($\sim 2 \times 10^{-14}$ $M_\odot$ yr^{-1}, where $M_\odot$ is the solar mass). Roughly 0.02% of the total mass loses throughout its main-sequence lifetime of

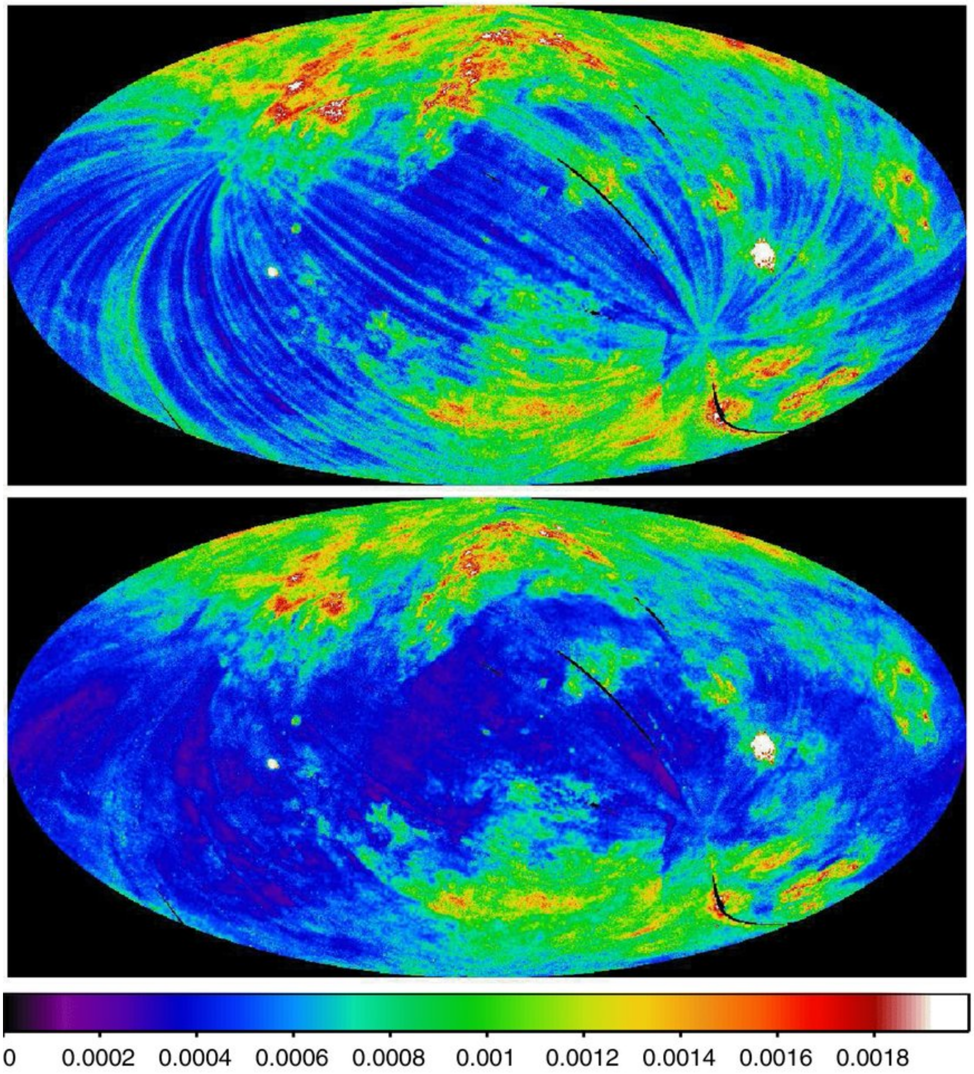

FIGURE 2.5: ROSAT all-sky survey maps of the 1 keV diffuse background before (upper panel) and after (lower panel) removal of the LTEs (Snowden et al., 1994; Snowden et al., 1997). The color bar shows X-ray intensity in units of counts s^{-1} $arcmin^{-2}$. The particle background (Snowden et al., 1992; Plucinsky et al., 1993) and scattered solar X-ray background (Snowden and Freyberg, 1993) have been subtracted in both maps. The maps are displayed in Aitoff-Hammer equal-area projections in Galactic coordinates with the Galactic center at the center and with Galactic longitude increasing to the left. This figure is presented in Snowden et al. (2009).

about 10 billion years. The existence of solar beams was predicted by Biermann (1951) from motions of cometary ion tails. He suggested that solar particles move radially from the Sun with velocities of $\sim$500–1500 km s^{-1}. Parker (1958) provided the first theoretical description of solar beams and named it "solar wind." The solar wind itself was first observed by sounding rockets and exploration satellites in the early 1960s. Many solar wind experiments for measuring its compositional, spatial, and temporal behavior have been conducted.

The solar wind consists primarily of electrons and protons with an admixture of a few percent of alpha particles but much less abundant heavier ions (e.g., C, N, O, Ne, Mg, and Si). These abundances depend on conditions at chromosphere and lower transition regions with temperatures of the order of 10^4 K. A charge state distribution of collisionless plasma is not changed any further near Earth. This is the freezing-in concept of Hundhausen et al. (1968). The charge states of heavier ions depend on conditions at corona with temperatures of the order of 10^6 K. A freezing-in temperature is defined as an electron temperature based on a ratio between any two charge states in ionization and recombination equilibrium. Each element has different ionization and recombination rates. The freezing-in temperature varies by each element. The charge state distribution for ion pairs of the same element is well represented by a single temperature corresponding to an origin of solar winds.

There are fast and slow winds. The former is associated with polar coronal holes which coincide with open magnetic field regions. The latter is associated with solar equator regions known as streamer belts. Figure 2.6 shows a typical morphology of two types of solar winds. The solar atmosphere during solar minimum consists of coronal holes covering polar regions. The rest is covered by solar quiet regions. Such structures are not seen during solar maximum.

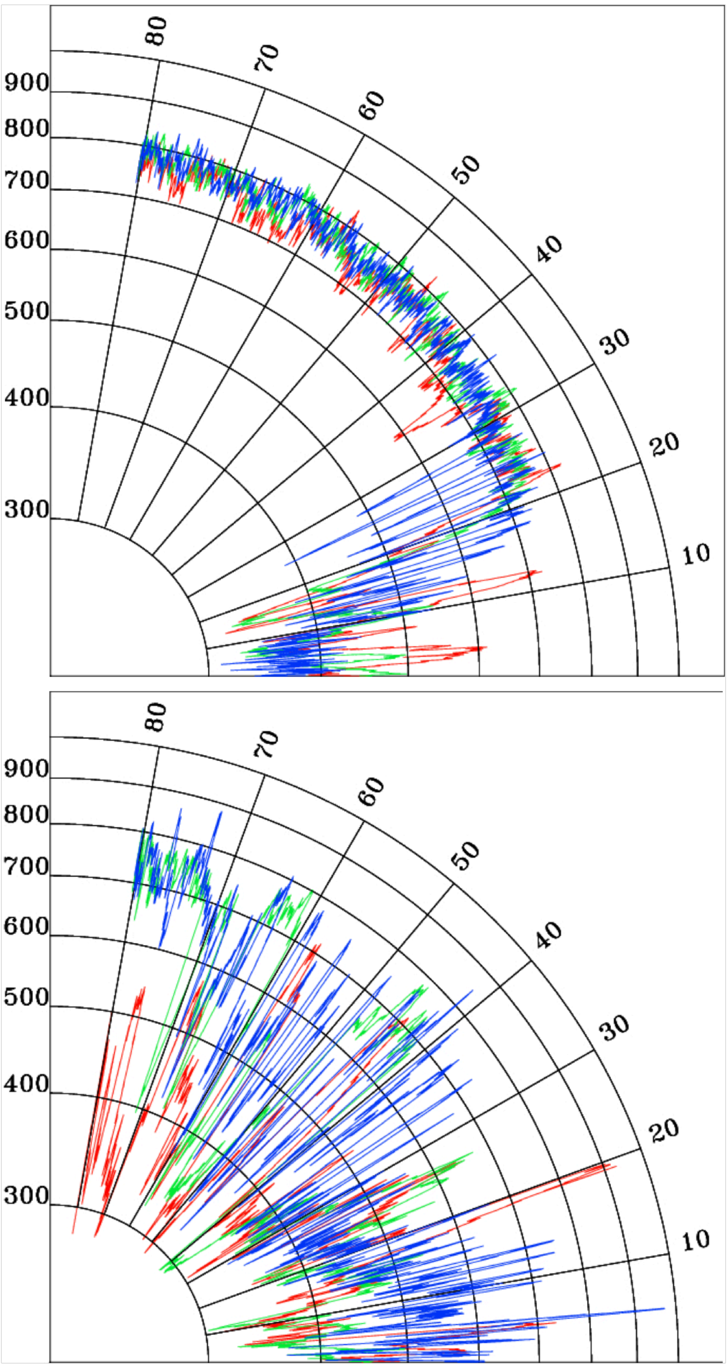

FIGURE 2.6: The Ulysses observations of solar wind morphology. The radial distance is the solar wind velocity marked in km s^{-1}, while the solar latitude is marked in degrees. Top panel: The solar wind velocity as a function of solar latitude for solar minimum. The data extend over three quarter-orbits (indicated by red, green, and blue curves) from day 256 of 1994 to day 349 of 1997. Bottom panel: The solar wind velocity as a function of solar latitude for solar maximum. The data extend over three quarter-orbits from day 329 of 2000 to day 53 of 2004. This figure is presented in Kuntz (2018).

The Earth's magnetosphere

Earth's magnetic fields can be described by a magnetic dipole. This dipole is produced by core of ferrous fluid and Earth's rotation. A region where solar wind dynamic pressure equals to Earth's magnetic pressure is a magnetopause typically located at ~10 R_E. The Earth's magnetosphere becomes an obstacle for supersonic solar winds and forms a bow shock. This shock slows solar winds to subsonic speeds and heats and compresses them at a magnetosheath. There are funnel-shaped regions of Earth's magnetic fields in north and south poles. These regions are called cusps where solar wind particles interact with Earth's upper atmospheres. A schematic of the Earth's magnetosphere is shown in Figure 2.7.

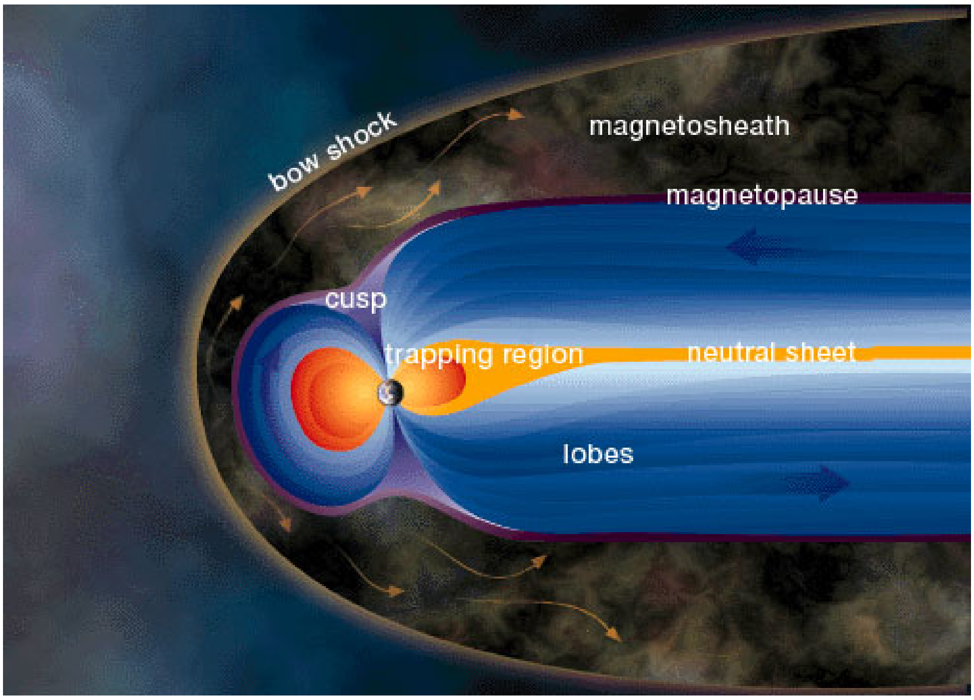

FIGURE 2.7: Schematic of Earth's magnetosphere.[5]

The Earth's exosphere

Above an altitude of ~100 km, Earth's atmospheric composition depends on molecular diffusion, i.e., gravitational settling results in an increase of lighter gases relative to

---

[5] The illustration is obtained from Windows to the Universe, National Earth Science Teachers Association: `https://www.windows2universe.org/earth/Magnetosphere/overview.html`.

heavier ones as altitude increases. The Earth's exosphere is the uppermost atmosphere which is mainly composed of atomic hydrogen. Hydrogen atoms are created by H_2 molecules through the following reactions with hot oxygen atoms: $H_2 + O \rightarrow H + OH$, and then $OH + O \rightarrow O_2 + H$, or $OH + H_2 \rightarrow H_2O + H$.

Exospheric particles with energies greater than gravitational ones and with outward radial velocities can escape to space. The base of the exosphere is defined as "exobase." A mean free path is equal to a so-called scale height. The Earth's exobase is approximately 500 km. Chamberlain (1963) presented an exosphere model based on three different neutral hydrogen populations: ballistic, escaping, and satellite particles. Ballistic particles with velocities less than escaping velocities fall back. Escaping particles flee to space. Particles scattered into closed orbits around Earth are called satellite particles. There are two density layers above the exobase. Lower altitudes are dominated by ballistic particles, while higher altitudes with rare collisions are dominated by satellite particles. The transition between ballistic- and satellite-dominated layers depends on temperatures at the exobase. Hodges Jr. (1994) constructed an exosphere model based on Monte Carlo simulations for ballistic trajectories and collisions. Typical neutral hydrogen density values are estimated to be $\sim$25 cm^{-3} at 10 R_{E}.

Neutral hydrogen atoms scatter solar Lyman-α radiations and produce "geocorona." Earlier studies used Lyman-α column brightnesses measured by Earth observation satellites IMAGE and TWINS (Østgaard et al., 2003; Bailey and Gruntman, 2011; Zoennchen et al., 2010; Zoennchen et al., 2011; Zoennchen et al., 2013; Zoennchen et al., 2015; Zoennchen et al., 2017), giving us exospheric densities at radial distances of 3–8 R_{E}. Optically thin conditions break down below 3 R_{E}. Background intensities exceed geocoronal ones beyond 8–10 R_{E}. The CASSINI spacecraft during swing-by maneuvers at Earth on its way to Saturn provided a unique opportunity for measuring exospheric densities at radial distances of 3–15 R_{E} (Zoennchen et al., 2022). Recent studies using deep space exploration satellites like PROCYON revealed exospheric densities at larger distances up to 60 R_{E} (Kameda et al., 2017; Baliukin et al., 2019).

Solar wind protons undergo charge exchange with exospheric neutral hydrogen atoms to become ENAs. ENA fluxes can be used for measuring exospheric neutral hydrogen densities around 10 R_E (Fuselier et al., 2010; Fuselier et al., 2020; Sibeck et al., 2021). These exospheric densities can also be deduced from soft X-ray observations (Connor and Carter, 2019; Jung et al., 2022). There are various exospheric density profiles as shown in Figure 2.8.

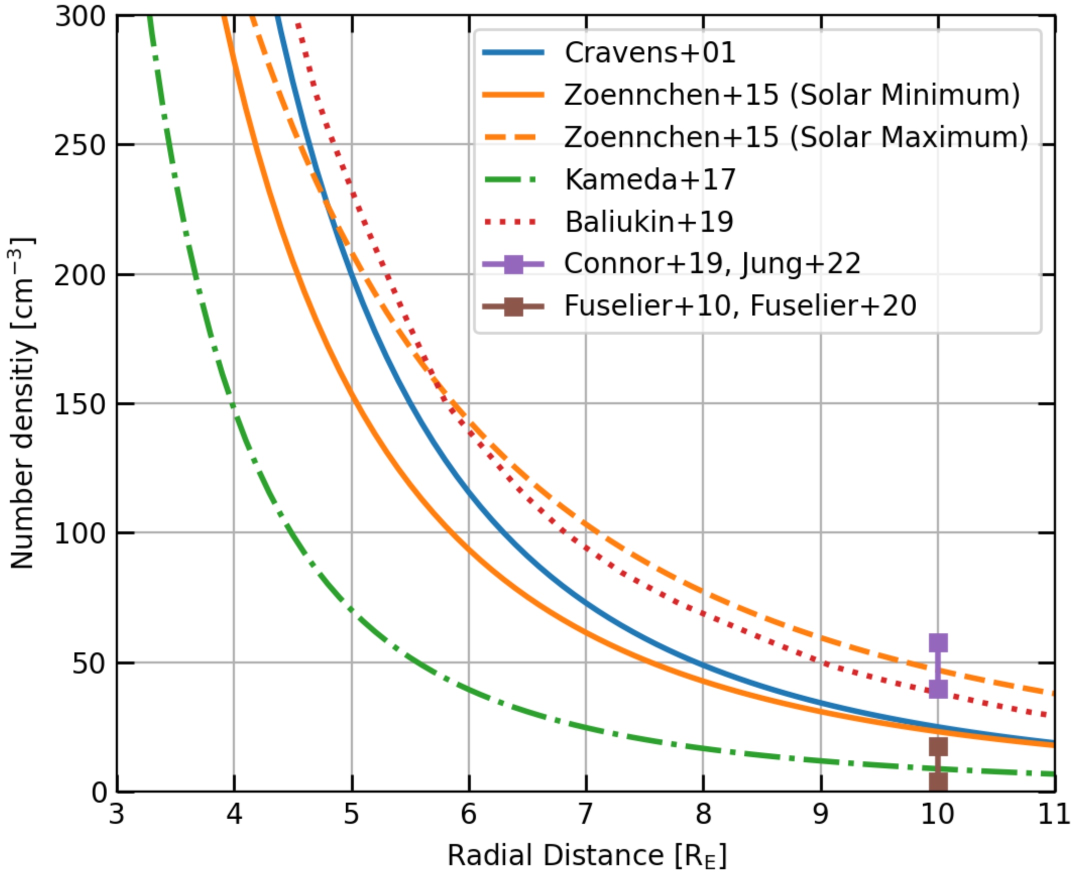

FIGURE 2.8: Comparison between dayside exospheric neutral hydrogen densities obtained from the previous literatures and a simplified formula of Cravens et al. (2001).

2.2.2 Observational and modeling studies

Cox (1998) and Freyberg (1998) suggested that similar reactions on comets operate to produce soft X-rays in the Earth's exosphere or geocorona. This suggestion was directly demonstrated by soft X-ray observations of the Moon. ROSAT produced the first soft X-ray image of the Moon (Schmitt et al., 1991). The image is shown in Figure 2.9. Soft X-rays were observed even on the dark side of the Moon where no scattering and fluorescence of solar X-rays are expected. Chandra detected soft X-ray emission from $\mathrm{O}_{\mathrm{VII}}$ and $\mathrm{O}_{\mathrm{VIII}}$ lines in two sets of observations on the dark side of the Moon (Wargelin et al., 2004).

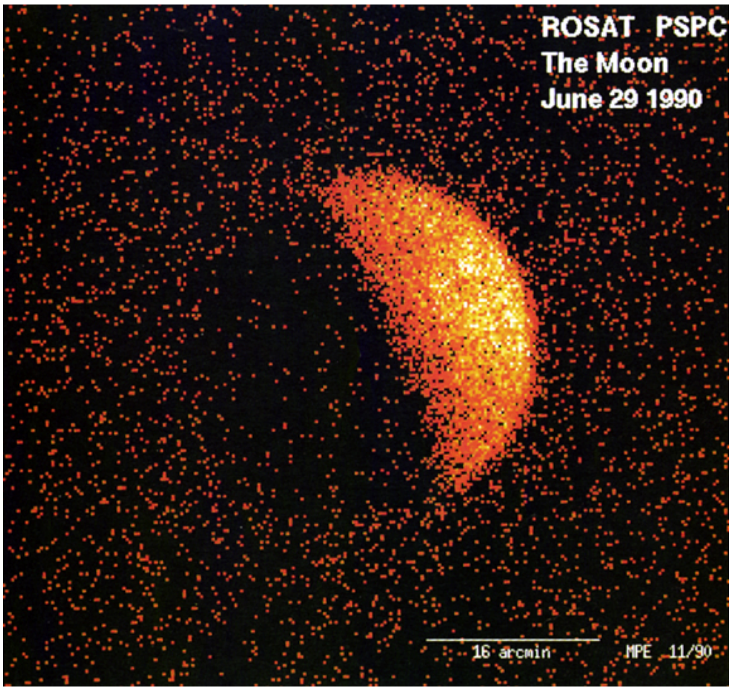

FIGURE 2.9: ROSAT X-ray image of the Moon. Scattering and fluorescence of solar X-rays are clearly visible in the right-side brighter area. Faint X-rays from the left-side dark area or the dark moon are mainly caused by charge exchange processes in cislunar space.[6]

All the soft X-ray observations from Earth-orbiting satellites must contend with a persistent foreground emission from both geocoronal and heliospheric SWCX (see Kuntz, 2018 for more complete discussions of problems posed to astrophysics). The former is typically an order of magnitude weaker than the latter but responds much more quickly (on time scales of less than an hour) to abrupt solar wind changes, thereby producing a sporadic contamination that sometimes reaches the same order of magnitude as the latter or even greater. The latter varies on much longer time scales and more subtle variations. To determine each contribution to astronomical observations,

---

[6] The image is credited by ROSAT/Schmitt et al.: `https://chandra.harvard.edu/photo/2003/moon/moon_rosat.jpg`.

careful checks of background signals combined with simultaneous solar wind observations are indispensable.

Recent X-ray astronomical observations with Chandra, XMM-Newton, and Suzaku have detected numerous SWCX events (e.g., Wargelin et al., 2004; Snowden et al., 2004; Fujimoto et al., 2007). Carter and Sembay (2008) and Carter et al. (2011) systematically searched for geocoronal SWCX events from XMM-Newton archival data. Most of the events occurred during periods when XMM-Newton observed through the sub-solar side of the magnetosheath. Models to simulate a spatial distribution of geocoronal SWCX emission (e.g., Robertson et al., 2006) indicate that the strongest emitters are present in the nose of the magnetosheath and in the magnetospheric cusps owing to dense populations of solar wind plasma and exospheric neutrals as shown in Figure 2.10. Strong SWCX events were sometimes detected even when their line-of-sight directions intersected regions where no strong emissions are expected (e.g., the flanks of the magnetosheath). These cases might originate from heliospheric SWCX events such as CMEs passing through local heliospheric structures. Carter et al. (2010) argued that, although XMM-Newton was not pointed to the regions where the strongest emissions are expected, i.e., neither the nose of the magnetosheath nor the magnetospheric cusps, the strongest, the most spectrally rich case was attributed to a CME passing through the Earth on 2001 October 21.

Carter et al. (2011) attempted to model roughly 100 XMM-Newton observations contaminated with time-variable geocoronal SWCX emission using a set of models to compute positions of the magnetosheath boundaries, i.e., the bow shock and the magnetopause, and to predict solar wind conditions in the near-Earth region (e.g., Spreiter et al., 1966). Approximately 50% of the modeled fluxes agreed with the observed ones within a factor of two. Whittaker et al. (2016) compared results from an magnetohydrodynamics (MHD)-based model with 19 strong SWCX events listed in Carter et al. (2011), giving only 6 cases (approximately 30%) returning count rates within a factor of two of the observed values.

The bulk of these studies attempting to model geocoronal SWCX emission observed

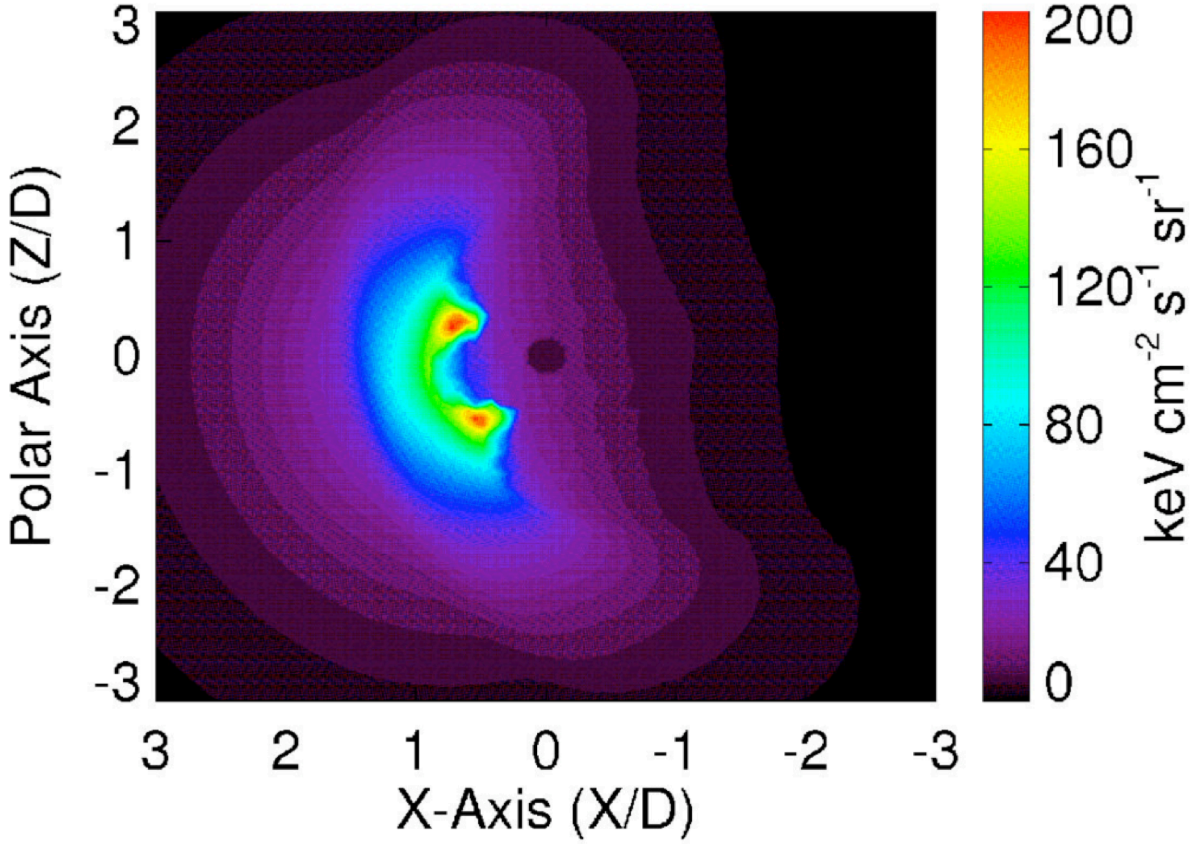

FIGURE 2.10: X-ray intensity map from geocoronal SWCX emission for geomagnetic storm condition (Robertson et al., 2006).

with Chandra and XMM-Newton have been concerned with observations of the bright nose of the magnetosheath from positions that maximize the path length through the magnetosheath (see Kuntz et al., 2015). Models of the magnetosheath have significant difficulties determining distances from the Earth to the noses of the bow shock and the magnetopause. The observer's line of sight might have completely missed the bright nose of the magnetosheath even with an error of 1 R_{E}, which is one of the main reasons for large discrepancies between models and observations. This problem has also been exemplified by comparison of an MHD model with a dozen Chandra SWCX observations (Wargelin et al., 2014).

Fujimoto et al. (2007) and Ezoe et al. (2010b) detected enhanced background events in the directions of the north ecliptic pole and the celestial equator, respectively. These enhancements showed significant temporal correlations with simultaneously observed solar wind fluxes, which is one of the most explicit signatures of geocoronal SWCX events. Ezoe et al. (2011) and Ishikawa et al. (2013) reported strong SWCX events associated with arrivals of increased solar wind fluxes during intense geomagnetic storms. Ishi et al. (2019) found an event in which background signals tracked abrupt solar wind changes due to a CME-induced interplanetary shock and the CME itself. These observed emissions exceeded by an order of magnitude compared to those predicted from upstream solar wind fluxes and exospheric neutral hydrogen column densities (e.g., Ezoe et al., 2010b; Ezoe et al., 2011; Ishikawa et al., 2013).

Compared to observations with Chandra and XMM-Newton, Suzaku can observe geocoronal SWCX emission through line-of-sight directions roughly perpendicular to the surface of the magnetosheath, i.e., the flanks of the magnetosheath. Model uncertainties in the nose of the magnetosheath have smaller effects on their results, e.g., overall fluxes and light curves. Modeling difficulties stem from the fact that the path length through the magnetosheath is much shorter and geocoronal SWCX emission from the flanks of the magnetosheath is intrinsically weaker.

The low-Earth orbit of Suzaku allows us to observe one of the strongest emitters, i.e., the magnetospheric cusps, which is difficult to observe with high-Earth orbit satellites (e.g., Chandra and XMM-Newton) due to Earth avoidance angles. Temporal variations with time scales of several minutes as observed with Suzaku (e.g., Fujimoto et al., 2007) are attributed to abrupt changes in the path length through the near-cusp region during an orbital motion of Suzaku. There are no good models for such geocoronal SWCX events.

Chapter 3

Instrumentation

X-rays from astronomical objects can only be measured from space because the Earth's atmosphere blocks them. Astronomers continue to launch many rockets and satellites devoted to observations of celestial X-ray sources. About thirty X-ray astronomy satellites have been launched. The United States, Russia, Europa, and Japan have launched most of them. There are two large X-ray astronomy satellites, Chandra and XMM-Newton, currently operating in orbit.

Chandra, launched on 1999 July 23, is one of the National Aeronautics and Space Administration (NASA) flagship missions, playing a role in the fleet of "great observatories." It achieves the highest angular resolution and provides us with spectacular images but is not suitable to observe extended X-ray sources like geocoronal SWCX emission because an instrumental background is high due to a high-altitude orbit passing through the Earth's radiation belts.

The X-ray Multi-mirror Mission (called XMM-Newton for short) is the second cornerstone of the European Space Agency (ESA) programme Horizon 2000. It was launched on 1999 December 10. A large effective area gives us spectra with good statistics. XMM-Newton is one of the suitable satellites to detect geocoronal SWCX events. It is placed in a highly elliptical orbit with an apogee of about 115,000 km and a perigee of about 6,000 km. The Earth limb avoidance angle is 42°. The minimum observable altitude is 40,000 km. These constraints make it difficult to observe geocoronal SWCX emission from the near-Earth region.

The Japanese X-ray astronomy satellite Suzaku, operated from 2005 to 2015, provides us with different views unlike the above satellites. A low-attitude orbit allows us to observe geocoronal SWCX emission from the near-Earth region. Suzaku is one of the suitable satellites to detect geocoronal SWCX events thanks to its low and stable instrumental background and good energy resolution and response. The details of Suzaku are described in the following section.

3.1 The Suzaku satellite

Suzaku (Mitsuda et al., 2007) is the fifth in a series of Japanese X-ray astronomy satellites, launched on 2005 July 10. It was managed by the Institute of Space and Astronautical Science of Japan Aerospace Exploration Agency (ISAS/JAXA). The solar paddles and extensible optical bench (EOB) were first deployed after the launch. Its orbit is near-circular with an apogee of 568 km, an orbital inclination of 31.9°, and an orbital period of about 96 minutes. Figure 3.1 shows a schematic view of the Suzaku orbit.

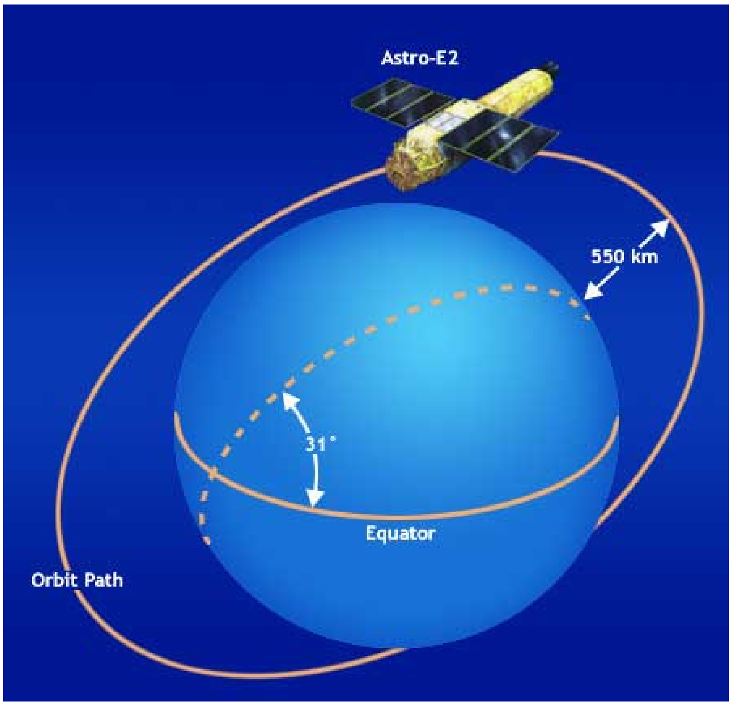

FIGURE 3.1: The 96-minute Suzaku orbit.[1]

---

[1] The image is taken from the Suzaku technical description: `https://heasarc.gsfc.nasa.gov/docs/suzaku/prop_tools/suzaku_td/`.

There are three scientific payloads. The first one is the X-ray Imaging Spectrometer (XIS; Koyama et al., 2007), which covers an energy range of 0.2–12 keV. The second one is the Hard X-ray Detector (HXD; Takahashi et al., 2007), which extends a bandpass with higher energies of 10–600 keV. The HXD data are not used because our target is mainly composed of soft X-rays below 2 keV. The third one is an X-ray microcalorimeter (X-Ray Spectrometer, XRS; Kelley et al., 2007), which has a higher energy resolution in an energy range of 0.3–12 keV. The XRS lost its cryogen in the very early phase and hampered its operation in orbit. The configuration of the above payloads is shown in Figure 3.2. The capabilities of Suzaku are summarized in Table 3.1.

TABLE 3.1: Overview of Suzaku capabilities after Mitsuda et al. (2007).

S/C	Orbital apogee	568 km
	Orbital period	96 min
	Observing efficiency	$\sim$43%
XRT	Focal length	4.75 m
	Field of view	$17'$ at 1.5 keV $13'$ at 8 keV
	Plate scale	$0.724'$ mm^{-1}
	Effective area	440 cm^2 at 1.5 keV 250 cm^2 at 8 keV
	Angular resolution	$2'$ (HPD)
XIS	Field of view	$17.8' \times 17.8'$
	Bandpass	0.2–12 keV
	Pixel grid	1024×1024
	Pixel size	24 μm $\times$ 24 μm
	Energy resolution	$\sim$130 eV at 6 keV (FWHM)
	Effective area (incl. XRT)	330 cm^2 (FI), 370 cm^2 (BI) at 1.5 keV 160 cm^2 (FI), 110 cm^2 (BI) at 8 keV
	Time resolution	8 s (normal mode)

3.1.1 X-Ray Telescope (XRT)

Suzaku has five X-Ray Telescopes (XRTs; Serlemitsos et al., 2007). Four of them (XRT-I0–3) are used for the XIS. The remaining one (XRT-S) is used for the XRS. The XRT

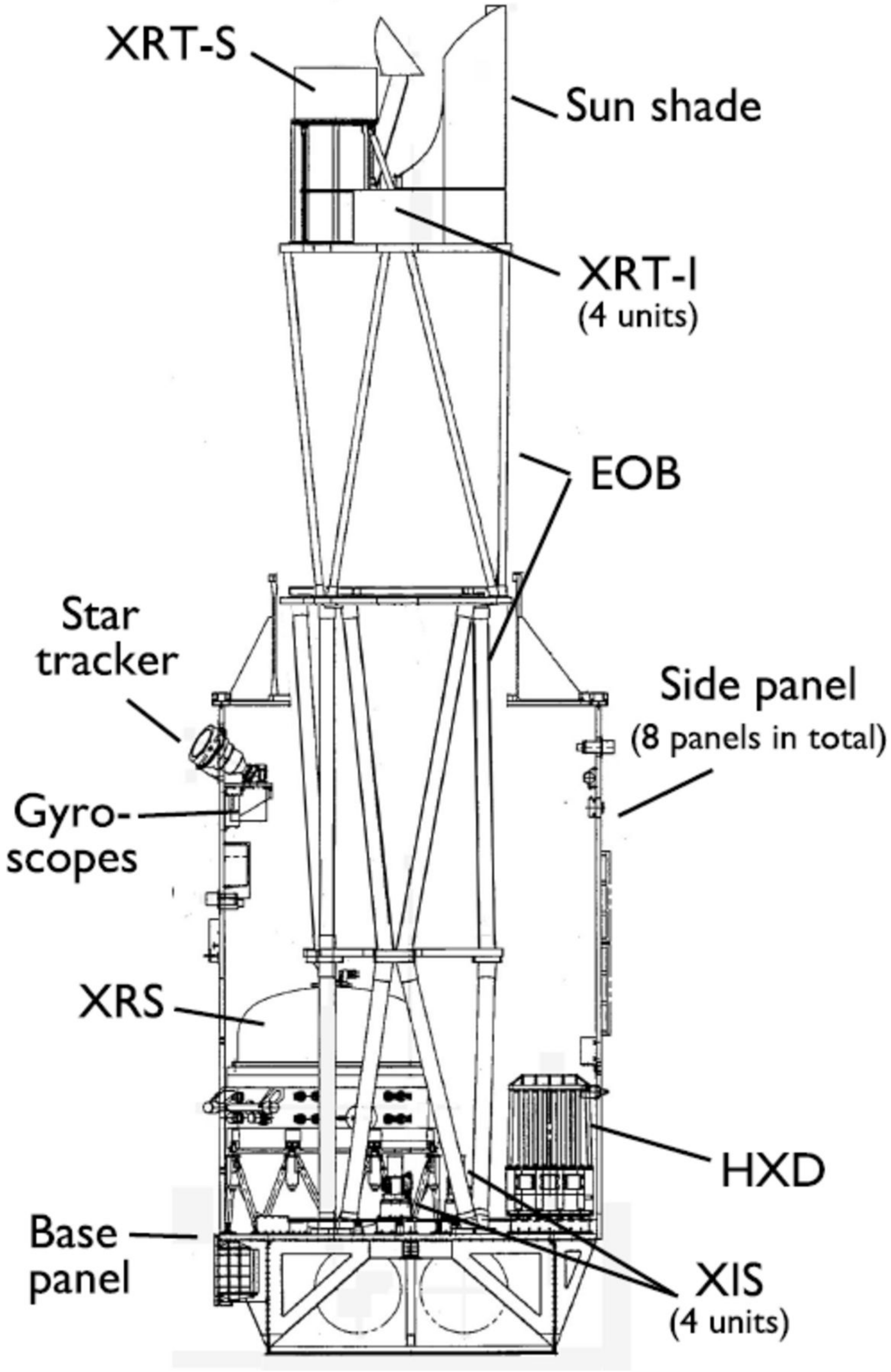

FIGURE 3.2: Side view of Suzaku with internal structures after EOB deployment (Mitsuda et al., 2007).

module consists of closely nested thin-foil plates that reflect X-rays at small grazing angles. It is a cylindrical shape with the following components:

- A thermal shield at the entrance aperture to keep internal temperatures as uniform as possible;
- A pre-collimator mounted on metal rings for elimination of stray lights;
- A primary stage for the first X-ray reflection;
- A secondary stage for the second X-ray reflection;
- A base ring for structural integrity and an interface with the EOB of the spacecraft.

All the above components except for the base ring are constructed in segments with an azimuth angle of 90°. Four quadrants are joined by interconnect couplers and by the top and base rings. The housing is made of aluminum to reduce weight. Each reflector consists of a substrate made of aluminum and an epoxy adhesion layer to bond the reflecting gold surface. Such thin substrates permit high-density nesting and provide a large collecting area with a moderate angular resolution at an energy range of 0.2–12 keV.

Optical axis

Figure 3.3 shows a location of the optical axis of each XRT-I module, showing source positions when an instrument is pointed at the aim point. The calibration data were taken from a series of observations of the Crab Nebula in 2005 August–September. The focal positions are close to the optical center with a deviation of $\sim 1'$. Each optical axis is expected to scatter within an angular range of $\sim 1'$. The field of view overlaps each other.

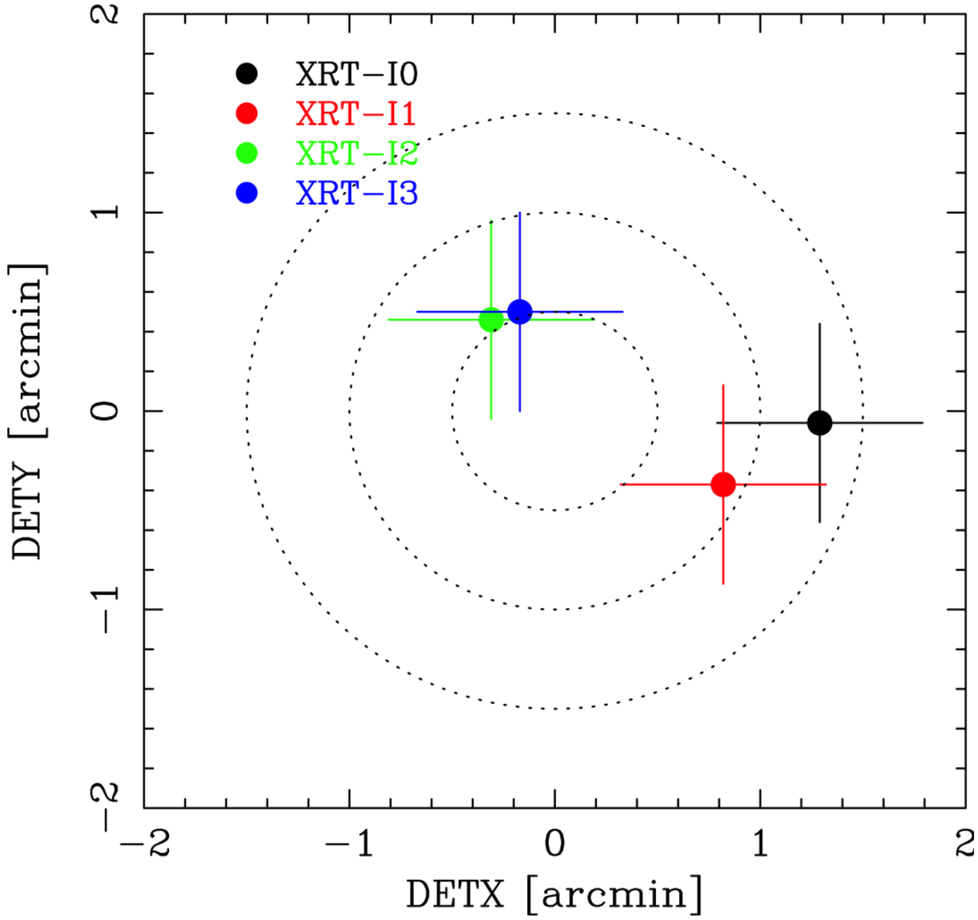

FIGURE 3.3: Focal positions of four XIS sensors when the satellite was pointed at the Crab Nebula in 2005 August–September (Serlemitsos et al., 2007). DETX and DETY indicate the detector coordinate system.

Effective area

The effective area was calibrated in orbit using observations of the Crab Nebula in 2005 September. The XIS sensors were operated in the normal mode with the 0.1 s burst option to avoid pile-up events and telemetry saturations. The hydrogen column density and photon index were estimated to be (0.32–0.33) $\times$ 10^{22} cm^{-2} and 2.09 ± 0.01, respectively. These values are consistent with the standard ones.

Vignetting effect

Suzaku observed the Crab Nebula in 2005 August at different off-axis angles of $0'$, $3.5'$, and $5.7'$. The vignetting effects of the four XRT-I modules were studied. Figure 3.4 shows vignetting curves compared with those calculated by a ray-tracing simulator, providing us with an effective area with an accuracy of $\sim$10%.

Angular resolution

The dwarf nova SS Cygni was observed in 2005 November. This object is a point source with a moderate brightness, e.g., 3.6, 5.9, 3.7, and 3.5 counts s^{-1} for XIS 0, 1, 2, and 3, respectively. Pile-up effects are negligible even at the brightest image center. Figure 3.5 shows X-ray images, point spread functions (PSFs), and encircled-energy fractions (EEFs). The EEF is normalized to unity at the edge. Each half power diameter (HPD) was estimated to be $1.8'$, $2.3'$, $2.0'$, and $2.0'$ for XRT-I0, 1, 2, and 3, respectively. These values are consistent with those from ground-based calibration experiments.

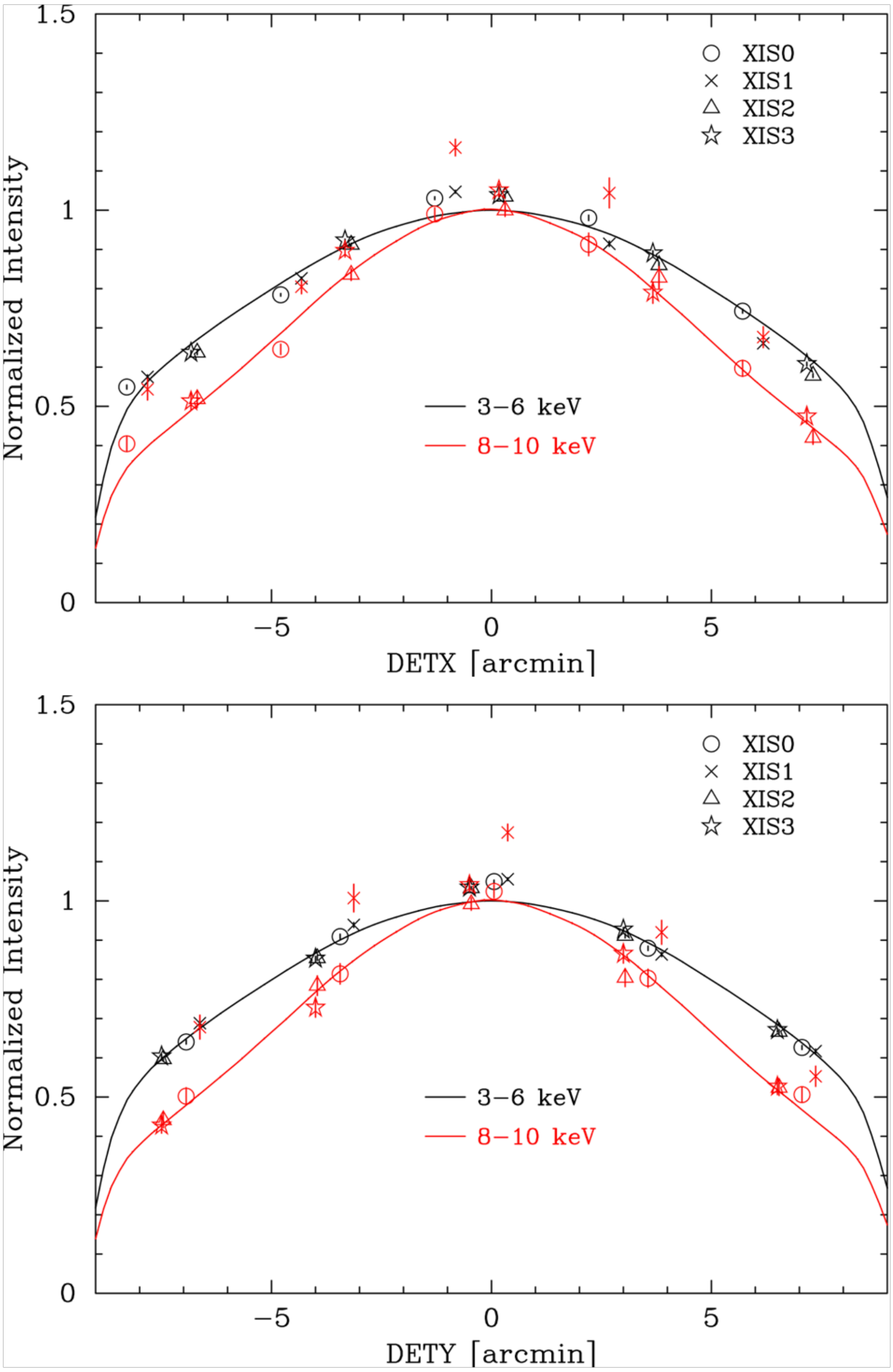

FIGURE 3.4: Vignetting curves of four XRT modules using the Crab Nebula observation in 2005 August (Serlemitsos et al., 2007). The model curves were calculated with a ray-tracing simulator with spectral parameters of $N_{\mathrm{H}} = 0.33 \times 10^{22}$ cm^{-2}, photon index of 2.09, and normalization of 9.845 photons cm^{-2} s^{-1} keV^{-1} at 1 keV.

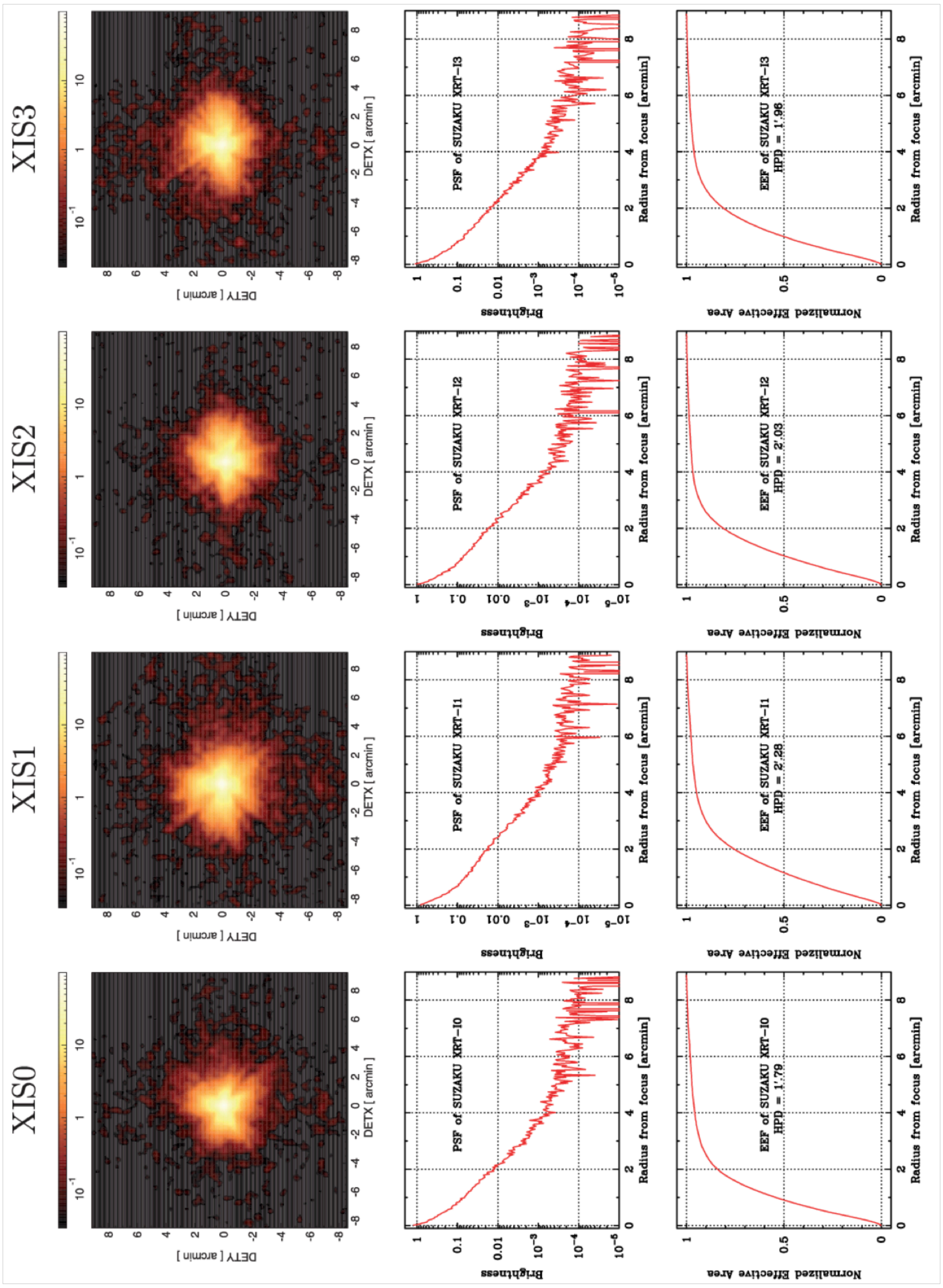

FIGURE 3.5: Image, PSF, and EEF of four XRT-I modules in the focal plane (Serlemitsos et al., 2007). All of the images are binned with 2 × 2 pixels, followed by being smoothed with a Gaussian profile with $\sigma = 3$ pixels.

3.1.2 X-ray Imaging Spectrometer (XIS)

The XIS instrument consists of four sensors: XIS 0, 1, 2, and 3. Each sensor has an X-ray sensitive charge-coupled device (CCD). A surface with a gate structure that transfers charge packets to a readout gate is called "front side." Front-illuminated (FI) CCDs (XIS 0, 2, and 3) detect photons on this side. Absorption of photons passing through such gate structures reduces quantum efficiency at lower energies. A back-illuminated (BI) CCD (XIS 1) receives photons from "back side" with no gate structures and has a higher quantum efficiency below 1 keV. Electrons drift to an opposite gate structure and produce a diffusive spread of an electron cloud which results in a worse energy resolution. Figure 3.6 shows comparisons between total effective areas combined with XRT efficiencies. There are some spectral features originating from elemental compositions, i.e., K-shell absorption edges of oxygen (0.54 keV) and aluminum (1.56 keV) in optical blocking filters and a number of weak M-shell features between 2 and 3 keV due to gold reflectors.

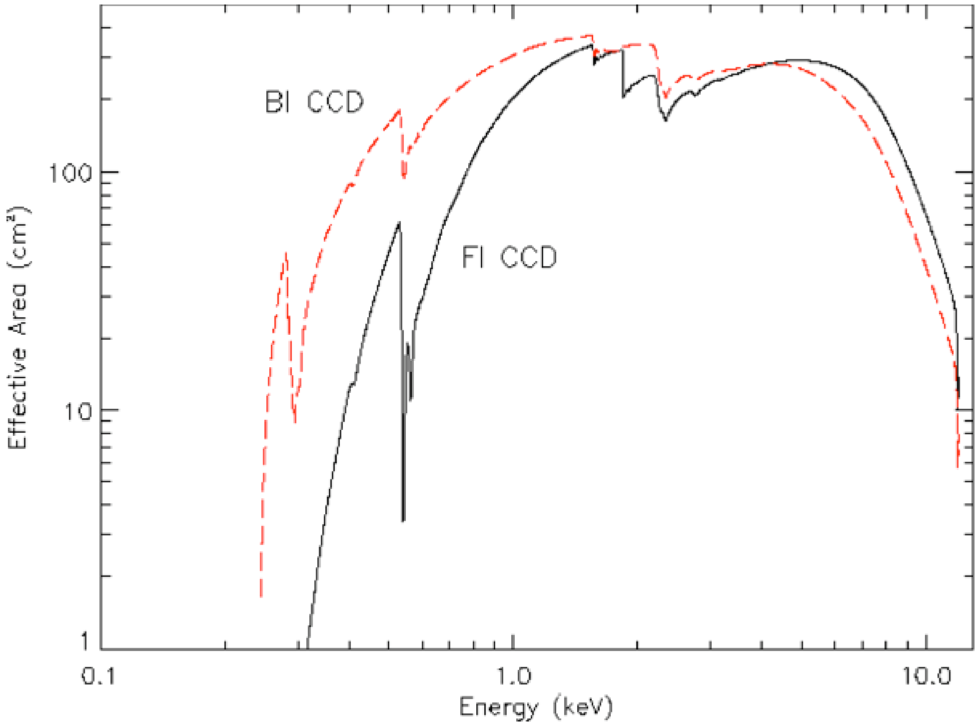

FIGURE 3.6: Effective area of one XRT + XIS system for FI and BI CCDs (Mitsuda et al., 2007).

Filter contamination

To suppress signals from optical and UV photons, optical blocking filters are installed in front of each sensor. It is made of polyimide with a thickness of 1000 Å, which is coated with 400 Å-thick aluminum on one side and with 800 Å-thick one on the opposite side. Quantum efficiency below 2 keV decreases in orbit due to accumulation of contaminated materials. The optical blocking filter is subject to radiation cooling and its low temperature causes such accumulation. Contamination sources are outgassing from a spacecraft's body and consist of several different materials with time-variable compositions. Thickness and chemical composition are monitored by observing standard cosmic X-ray sources and scatted solar X-rays.

Energy response and resolution

An X-ray photon is absorbed on a pixel and is converted to an electric charge which produces a voltage at an analog output. This voltage, i.e., "pulse-height," is proportional to an energy of an incident X-ray photon. A pulse-height distribution function for monochromatic X-rays can not be represented by a single Gaussian model because it has a tail component at lower pulse-height sides. These tail components require a second Gaussian model, i.e., "sub peak component." Electrons are split over a few pixels. Some pixels have pulse-heights lower than a split threshold and are not counted as a signal. A fraction of lower energy tail components of Suzaku/XIS is very small and clear peaks are exhibited. The energy resolution for oxygen Kα lines at 0.525 keV is $\sim$50 eV (FWHM) for XIS 1 and $\sim$40 eV (FWHM) for XIS 0, 2, and 3.

Hot and flickering pixels

Hot pixels always output signals over a threshold of pulse-heights without input signals. Such pixels are not usable for observations and their signals should be disregarded. Hot pixels can be recognized on board and are excluded by standard event detection processes. There are some pixels that intermittently output signals over a threshold of pulse-heights. Such pixels are called flickering pixels. It is difficult to identify flickering pixels on board. These pixels need to be removed during ground pile-line processes. Flickering pixels sometimes cluster around specific columns. This makes it relatively easy to identify them.

Radiation damage

Radiation damage by cosmic particles causes an increase in dark levels and a decrease in charge transfer efficiency. The former is expected to be small due to an operating temperature of -90 °C. The latter is unavoidable. Three ^{55}Fe isotopes are mounted on each sensor in order to calibrate an energy scale in orbit. It emits strong Mn Kα and Kβ lines at 5.9 and 6.5 keV, respectively. Two sources are attached on the sidewalls of the housing and illuminate two corners to monitor charge losses during transfers by gain comparison. The other one is attached on the door and illuminates the entire chip for the initial calibration before opening the door. A chip device of Suzaku/XIS employs space-row charge injection to recover charge transfer efficiency. Periodically injected artificial charges fill radiation-induced traps, preventing electrons produced by X-ray photons from being captured in such charge traps.

Instrumental background

The Suzaku instrumental background mainly originates from cosmic rays and its spectrum consists of a continuum and several emission lines. The continuum component is produced when cosmic rays directly deposit their energies on a chip. Fluorescent X-rays are emitted when cosmic rays interact with a spacecraft's body. The low-Earth orbit of Suzaku provides us with quite stable background levels on time scales of months. The background rate at an energy range of 0.4–12 keV is 0.3–0.6 counts s^{-1} for XIS 1 and 0.1–0.2 counts s^{-1} for XIS 0, 2, and 3.

3.2 Solar wind monitoring satellites

To obtain information on solar wind plasma and interplanetary magnetic fields, we utilized two solar wind monitoring satellites, WIND and ACE, currently orbiting around the Lagrangian point L_1 between the Sun and Earth (about 1.5 million km from Earth).

3.2.1 WIND

WIND, launched on 1994 November 1, is the first spacecraft in the Global Geospace Science initiative and part of the International Solar-Terrestrial Physics program. Figure 3.7 shows an orbit after the launch. The WIND spacecraft was first placed in a “double lunar swing-by” orbit for the first nine months of operation and was then inserted into a “halo” orbit around the Lagrangian point L_1 between the Sun and Earth taking some detours.

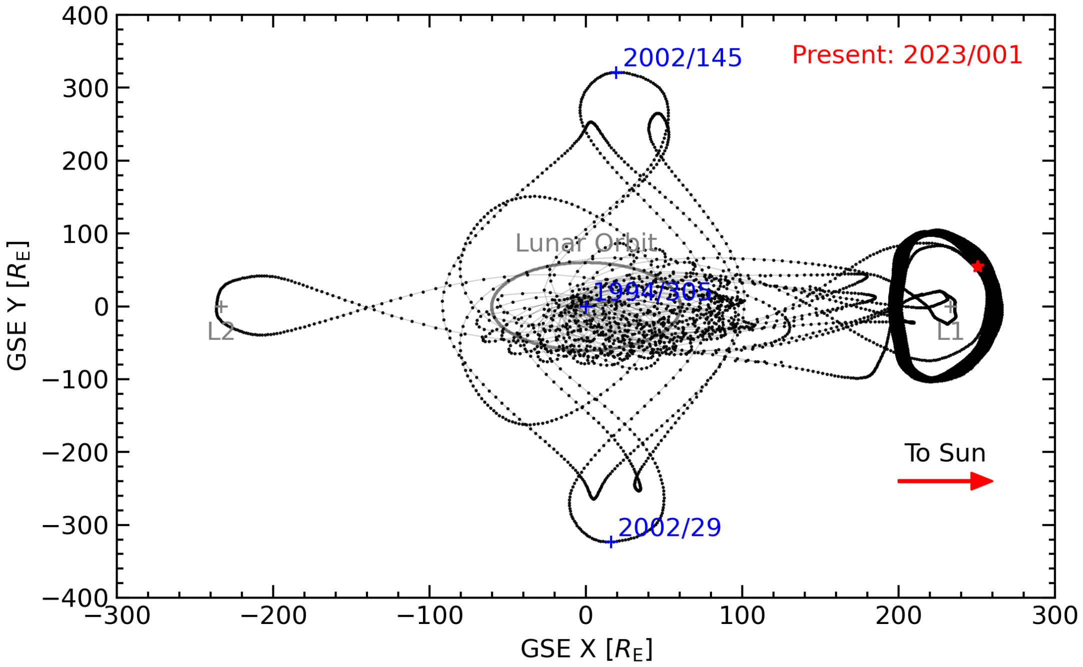

FIGURE 3.7: The WIND orbit after the launch.

Solar Wind Experiment (SWE)

The Solar Wind Experiment (SWE; Ogilvie et al., 1995) measures ions and electrons in solar winds, which allows scientists to determine solar wind velocity, density, and temperature and to reveal properties of plasma and its pivotal roles in transfers of mass, momentum, and energy from the Sun to Earth. It consists of a vector electron and ion spectrometer (VEIS), a strahl sensor, and two Faraday cup (FC) sensors. The VEIS determines a distribution function of ions and electrons at energy and charge ranges from 7 V to 24.8 kV. The strahl sensor characterizes any magnetic field aligned beams, i.e., “strahl,” in solar wind electron velocity distributions at energy and charge ranges from 5 V to 5 kV. The FC measures solar wind protons and alpha particles at energy and charge ranges up to 8 kV. It is particularly suited for measurements of flowing supersonic plasma to obtain information on velocity, density, and temperature.

Magnetic Field Investigation (MFI)

The Magnetic Field Investigation (MFI) provides large-scale structures and fluctuations in solar wind’s magnetic fields. Such magnetic fields transport energies and accelerate particles. Magnetic field observations are important for studying solar wind-magnetosphere coupling processes.

3.2.2 ACE

The Advanced Composition Explorer (ACE) is an explorer mission that was managed by the Office of Space Science Mission and Payload Development Division of NASA/GSFC. It was launched on 1997 August 25 from the Kennedy Space Center in Florida. Figure 3.8 shows an orbit after the launch.

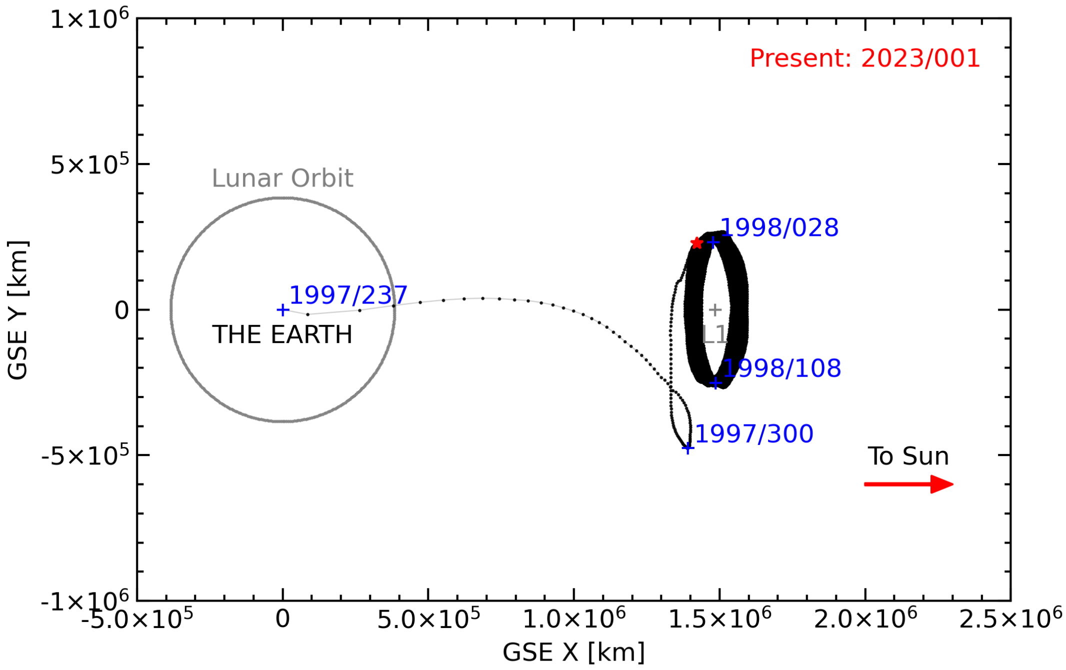

FIGURE 3.8: The ACE orbit after the launch.

Solar Wind Ion Composition Spectrometer (SWICS)

The Solar Wind Ion Composition Spectrometer (SWICS; Gloeckler et al., 1998) is an instrument optimized for measurements of chemical and isotopic composition of solar particles. It is a time-of-flight mass spectrometer that measures energy per charge, time-of-flight, and residual energy. This allows us to estimate speed, mass per charge, charge, and mass for each ion. Its operation is based on techniques of particle identification using a combination of electrostatic deflection, post-acceleration, time-of-flight, and energy measurement. Figure 3.9 shows the principle of operation illustrating the functions of five basic sensors:

- Ions of kinetic energy E, mass M, and charge state Q enter a sensor through a collimator that selects proper entrance trajectories of particles.

- The electrostatic deflection analyzer acts as a UV trap and an energy per charge (E/Q) filter, allowing only ions within a given energy per charge interval (determined by a stepped deflection voltage) to enter the time-of-flight versus energy

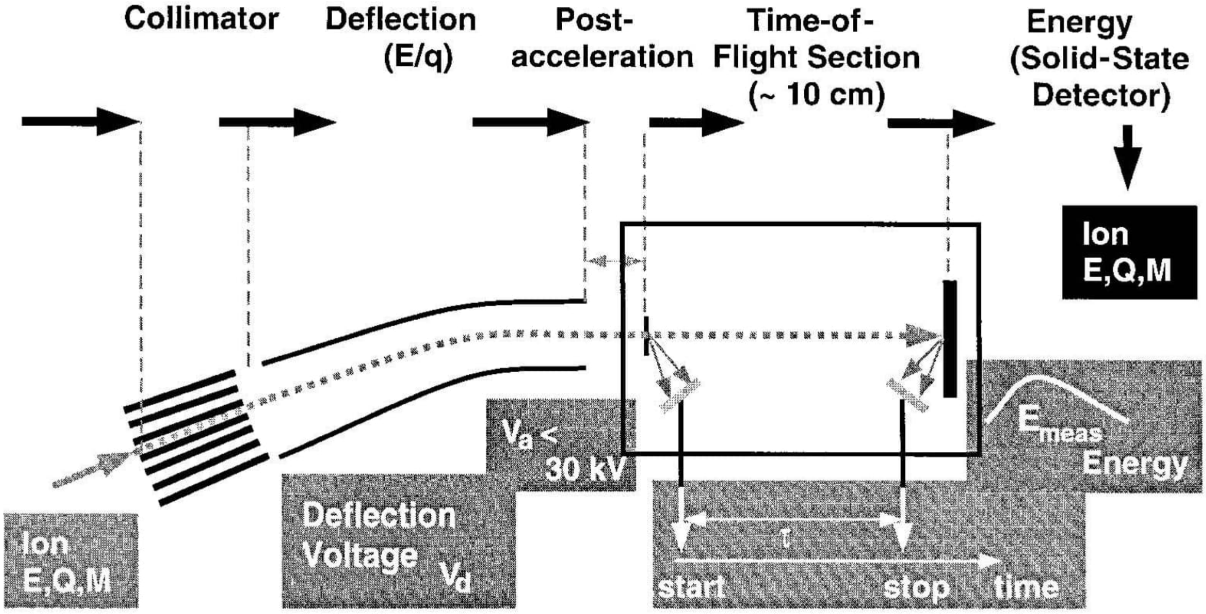

FIGURE 3.9: Principle of the time-of-flight mass spectrometer with ACE/SWICS (Gloeckler et al., 1998).

system.

- Ions are post-accelerated by up to 30 kV before entering the time-of-flight versus energy system. The gained energy is sufficient to be adequately measured by the solid-state detectors which typically have energy thresholds of 25–35 keV. An energy measurement is required for determining the mass composition of an ion population. Ions with energies below $\sim$30 keV must be accelerated if their mass is to be identified.

- The speed of each ion is determined by measuring the travel time τ of the particle between the start and stop detectors separated by a distance of 10 cm in the time-of-flight system.

- The particle identification is completed by measuring the residual energy of the ions in a conventional low-noise solid-state detector.

From simultaneous measurements of the time-of-flight τ, and residual energy E_{meas}, and a knowledge of E/Q and the post-acceleration voltage U_{a}, we can determine mass (M), charge state (Q), incident energy (E), and incident speed (V_{ion}) of each ion as follows:

$$
\begin{aligned}
M &= 2(\tau/d)^2(E_{\mathrm{meas}}/\alpha), & (3.1)\\
Q &= \frac{E_{\mathrm{meas}}/\alpha}{(U_{\mathrm{a}} + E/Q)\cdot\beta} \approx (E_{\mathrm{meas}}/\alpha)/U_{\mathrm{a}}, & (3.2)\\
M/Q &= 2(\tau/d)^2(U_{\mathrm{a}} + E/Q)\beta \approx 2(\tau/d)^2 U_{\mathrm{a}}, & (3.3)\\
E_{\mathrm{ion}} &= Q\cdot(E/Q), & (3.4)\\
V_{\mathrm{ion}} &= 438\cdot[(E/Q)/(M/Q)]^2, & (3.5)
\end{aligned}
$$

where d is the flight path, β takes account of the small energy loss of ions in the thin foil of the start-time detector, and α is the nuclear defect in solid state detectors. The units of V_{ion} are km s^{-1} when E/Q is in keV e^{-1} and M/Q is in amu e^{-1}. The approximate expressions for Q and M/Q hold for typical solar wind ions.

Solar Wind Electron, Proton & Alpha Monitor (SWEPAM)

The Solar Wind Electron, Proton & Alpha Monitor (SWEPAM; McComas et al., 1998) measures solar wind electrons and ion fluxes as functions of directions and energies, providing information on solar wind conditions every minute and real-time solar wind data continuously telemetered to the ground for space weather purposes. Electrons and ions are measured by separate sensors. The electron sensor has an energy range of 1–1350 eV. The ion sensor measures particle energies between 0.26 and 36 keV q^{-1}. Both sensors use an electrostatic analyzer with a fan-shaped field of view and measure energy per charge of each particle by bending flight paths. Its field of view is swept in all solar wind directions by spacecraft rotations.

Magnetometer (MAG)

The Magnetometer (MAG) measures interplanetary magnetic field directions and magnitudes as a function of time. Except for minor modifications, it is a flight spare on the WIND spacecraft.

Chapter 4

Geocoronal SWCX observations

This chapter gives descriptions of our observational data and filtering procedures.

4.1 Observational data

Our observational data consist of the five Suzaku detections of bright geocoronal SWCX events listed in Table 4.1. These observations showed clear temporal variations in soft X-ray backgrounds which are established as time-variable components of geocoronal SWCX emission in the past studies (Fujimoto et al., 2007; Ezoe et al., 2010b; Ezoe et al., 2011; Ishikawa et al., 2013; Ishi et al., 2019). Those of heliospheric SWCX emission are expected to be constant during observations of several hours to a couple of days. Therefore, we can extract only geocoronal SWCX emission.

TABLE 4.1: Suzaku observation log of five bright geocoronal SWCX events.

ID	ObsID	Date	Target name	Target coordinates (RA, Dec)$_{\mathrm{J2000.0}}$	Effective exposure (ks)	TDX area (arcmin^2)
1[*]	100009010	2005 August 23–24	PSR B1509−58	(228.4837°, −59.1356°)	60.7	44.4
2[†]	100014010	2005 August 31	1E0102.2−7219	(16.0100°, −72.0333°)	24.3	71.0
3[‡]	100018010	2005 September 2–4	North Ecliptic Pole	(272.8000°, 66.0000°)	106.2	227.3
4[§]	500009010	2005 October 28–30	Galactic Ridge	(281.0000°, −4.0700°)	93.4	198.8
5[‖]	508072010	2013 April 11–15	0509−67.5	(77.3927°, −67.5253°)	157.4	174.7

[*] Ezoe et al. (2011).

[†] Ishikawa et al. (2013).

[‡] Fujimoto et al. (2007).

[§] Ezoe et al. (2010b).

[‖] Ishi et al. (2019).

The observational parameters are summarized in Table 4.1. The solar activity during the first four observations (ObsIDs: 100009010, 100014010, 100018010, and 500009010) was approaching its minimum, the end of the 23rd solar cycle, while that during the last observation (ObsID: 508072010) was around the maximum of the 24th solar cycle. Hereafter, we call these observations ID1–5 as defined in Table 4.1.

There is another bright SWCX event detected with Suzaku as reported in Asakura et al. (2021). It consists of a set of two observations on 2005 September 11–13 and 2006 January 26–27. The former spectrum contained a series of enhanced emission lines from highly charged ions in CMEs, while the latter one did not. Their solar activities and line-of-sight directions relative to a stream of interstellar neutrals, i.e., the downwind gravitational focusing cone of interstellar helium atoms, are different, resulting in a potentially different heliospheric SWCX contribution to each observation. Considering significant difficulties predicting solar wind propagations and interstellar neutral distributions on large spatial scales, we did not use this event for comparison.

Figure 4.1 shows average line-of-sight directions in geocentric solar ecliptic (GSE) coordinates during each observation. These line-of-sight directions passed through a variety of regions in the Earth's magnetosphere, i.e., the dusk side of the mid-latitude magnetosheath (ID1), the night side of the high-latitude magnetosheath (ID2), the northern polar cusp (ID3), the day side of the low-latitude magnetosheath (ID4), and the southern polar cusp (ID5). The Suzaku solar-angle constraint had been tightened from $65°$–$115°$ to $70°$–$110°$ during the Suzaku AO-7 cycle (2012 April–2013 March) due to the solar panel degradation in power output. The former applied to the observations of ID1–4, while the latter to that of ID5. This change may influence scattering of solar X-rays to each observation. Therefore, we quantitatively check this possibility later in Subsection 4.2.2.

We used only XIS 1 data because it is more sensitive to soft X-rays than the other detectors (XIS 0, 2, and 3). Figure 4.2 shows an XIS 1 image in the 0.2–1 keV band during each observation. To minimize contamination from bright X-ray source(s) in the field of view of ID1, 2, and 5, we chose triangle or polygon regions located at

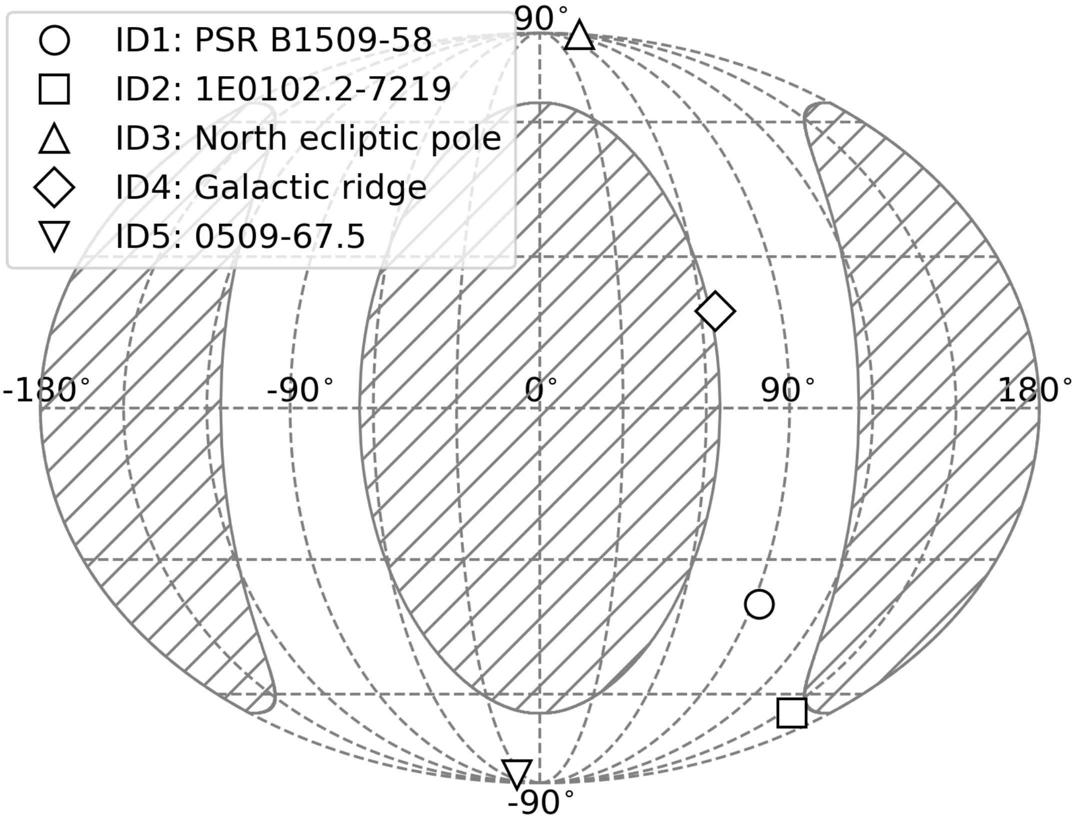

FIGURE 4.1: Average line-of-sight directions in the GSE coordinate system during the observations of ID1–5. The hatched regions mark the Sun angle range prohibited in Suzaku observations outside 65°–115°.

the corners of each field of view for the following light curve and spectral analyses. Hereafter, we call these regions terrestrial diffuse X-ray (TDX) regions. For those of ID3 and 4, we defined a circular region with a radius of $8.5'$ as the TDX region by considering well-calibrated radial profiles of contamination distributions on optical blocking filters. There are two sources emitting hard X-rays above 2 keV in the field of view of ID4 (see Ebisawa et al., 2008). Therefore, we excluded these sources or two circular regions with radii of $2'$ and $2.5'$ from the TDX region. The total areas of each TDX region are summarized in Table 4.1.

4.2 Filtering procedures

Using the HEAsoft version 6.27.2 package, we performed data analysis from cleaned event files screened through the Suzaku final pipeline processing version 3.0.22.43 and 3.0.22.44, both reprocessed after the end of satellite operations in 2015. Events were filtered by standard screening criteria, which remove high-background intervals mainly during passages through the South Atlantic Anomaly and through regions of low geomagnetic cut-off-rigidities.

4.2.1 Mitigation of non X-ray backgrounds

Hot and flickering pixels were removed with the latest calibration database but the number of noise pixels cumulatively increased in the later phase of the Suzaku mission, resulting in an increased non X-ray background (NXB) level. For the data of ID5 observed in 2013, we excluded noise events by a cumulative flickering pixel map identified by the calibration team of Suzaku/XIS. For those of ID1–4 observed in 2005, soon after the launch of the satellite, we did not exclude such events because such pixels were not identified at that time.

Although XIS 1 kept a spectral resolution good enough in the early observation, it became worse due to radiation damage by cosmic particles. To rejuvenate its spectral resolution by filling charge traps with artificially injected charges, spaced-row charge

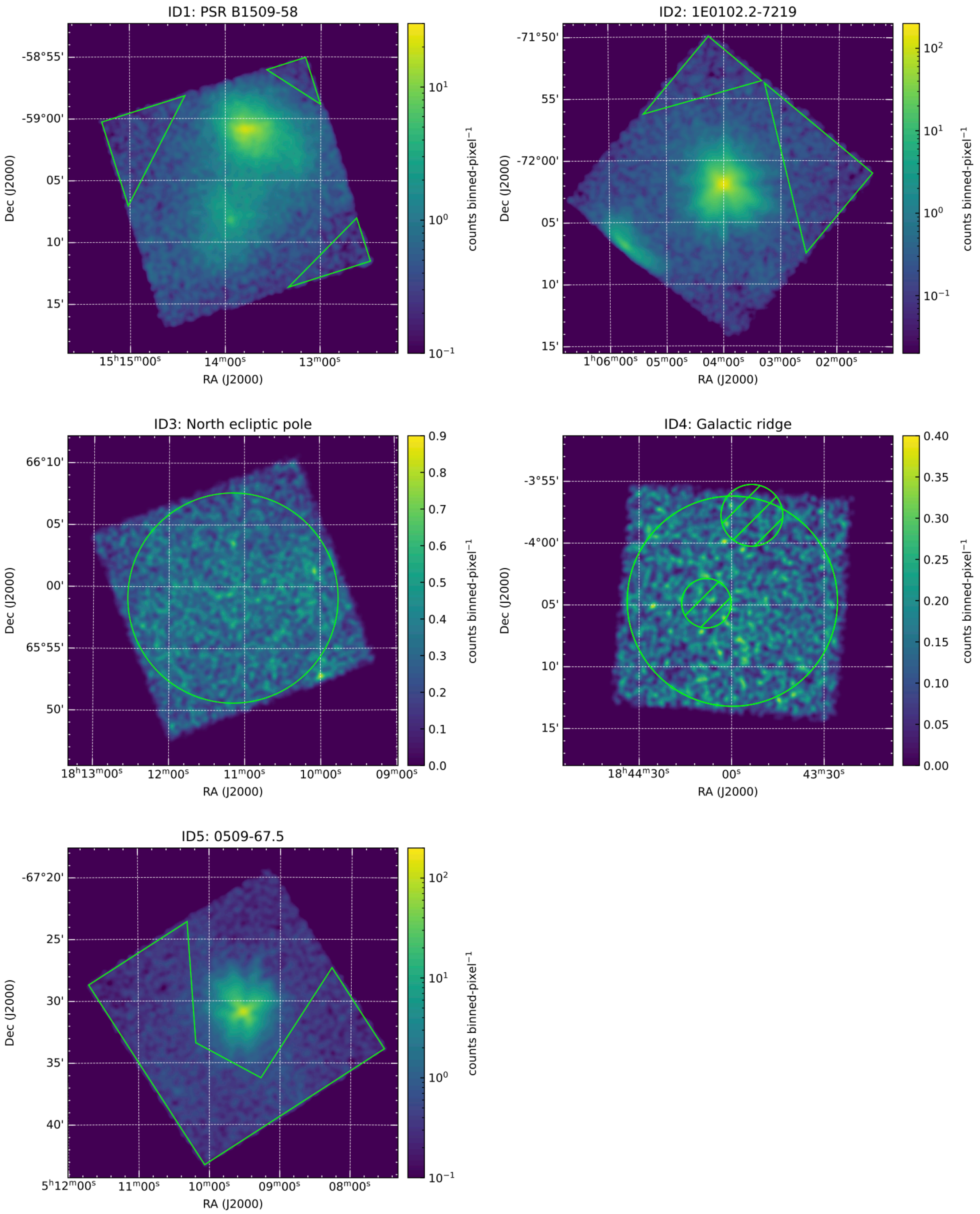

FIGURE 4.2: XIS 1 0.2–1 keV images of ID1–5. The images are binned in 4×4 pixels and smoothed by a Gaussian kernel of $\sigma = 2.5$ binned-pixels. The green triangle, circle, and polygon regions except for the hatched circle ones are used for light curve and spectral analyses.

injection had been performed since 2006. For the observation of ID5, we removed not only the first but also second rows adjacent to charge injected ones to avoid leaked events due to an increased charge injection from 2 to 6 keV after 2011.

The above additional screening of ID5 resulted in an improved signal-to-noise ratio in soft bands below 1 keV. The effective area of the TDX region decreased by $\sim$6%, while the NXB rate in the 0.2–1 keV band derived from the night-Earth database (Tawa et al., 2008) was suppressed by $\sim$19%.

4.2.2 Removal of scattered solar X-rays

The interaction between solar X-rays and neutral oxygen atoms or molecules in the Earth's atmosphere produces a fluorescent emission line at 0.525 keV. This line sometimes appears even after excluding periods where elevation angles from the Earth rim (ELV) and the bright-Earth rim (DYE_ELV) are less than 5° and 20°, respectively (e.g., Sekiya et al., 2014).

For each observation, we checked spectra extracted from the TDX region at different ELV values of 5° (default criterion), 10°, 20°, and 30°. The observations of ID1 and 5 showed a strong neutral oxygen emission line. This line became negligible when the ELV value was changed from 5° to 10°. Therefore, we adapted the ELV value of 10°. The exposure times of ID1 and 5 decreased by $\sim$1% and $\sim$10%, respectively. The default criterion was applied to the other observations because no significant neutral oxygen emission line was observed. The exposure times of ID1–5 are summarized in Table 4.1.

We also checked spectra at different DYE_ELV values of 20° (default criterion), 30°, 40°, 50°, and 60°. The neutral oxygen emission lines of ID1 and 5 became negligible when the DYE_ELV values were set to 30° and 40°, respectively, reducing the exposure times by $\sim$14% and $\sim$38%. Considering a significant loss of the exposure time, we decided to change the ELV value rather than the DYE_ELV value.

Chapter 5

Analysis

This chapter describes our analysis procedures for geocoronal SWCX observations.

5.1 Light curves

For each observation, we plot X-ray light curves extracted from the TDX region in the 0.5–0.7 keV band in Figures 5.1–5.5. This band contains O $_{\rm VII}$ and O $_{\rm VIII}$ emission lines often seen in geocoronal SWCX events. The 0.5–0.7 keV count rate shows two features. One is a sudden enhancement during the observations of ID1, 3, and 5. The other is a gradual one during those of ID2 and 4. There appear to be some increases just before the sudden ones of ID1, 3, and 5. These temporal variations should be related to solar wind and geomagnetic events as mentioned later in Subsections 5.1.1 and 5.1.2.

Hereafter, we define the *stable*, *pre-flare*, and *flare* periods as indicated by the black bars in Figures 5.1–5.5. The average rates or the total counts divided by the exposure time during each period are shown in Table 5.1. That of ID1 increased by a factor of $\sim$3 during the *pre-flare* period, while those of ID3 and 5 increased by $\sim$34% and $\sim$20% from the *stable* period to the *pre-flare* period, respectively. That of ID1 increased by a factor of $\sim$4 during the *flare* period, while those of ID2–5 increased by a factor of $\sim$2 during the *flare* period.

For comparison, we then plot X-ray light curves in the 2.5–5 keV band. This band

TABLE 5.1: XIS 1 count rates extracted from the TDX region.*

ID	Energy band	*Stable*	*Pre-flare*	*Flare*
1	0.5–0.7 keV	0.12 ± 0.01	0.34 ± 0.05	0.53 ± 0.02
	2.5–5 keV	0.47 ± 0.02	0.57 ± 0.07	1.39 ± 0.04
2	0.5–0.7 keV	0.31 ± 0.02	–	0.67 ± 0.03
	2.5–5 keV	0.17 ± 0.02	–	0.52 ± 0.02
3	0.5–0.7 keV	0.20 ± 0.01	0.27 ± 0.01	0.36 ± 0.01
	2.5–5 keV	0.19 ± 0.01	0.22 ± 0.01	0.27 ± 0.01
4	0.5–0.7 keV	0.07 ± 0.01	–	0.12 ± 0.01
	2.5–5 keV	0.37 ± 0.01	–	0.39 ± 0.01
5	0.5–0.7 keV	0.17 ± 0.01	0.20 ± 0.01	0.33 ± 0.01
	2.5–5 keV	0.12 ± 0.01	0.11 ± 0.01	0.12 ± 0.01

* In units of 10^{-3} counts s^{-1} $arcmin^{-2}$.

is composed of a non-SWCX continuum, e.g., originating from enhanced particle backgrounds. The 2.5–5 keV count rate shows some abrupt changes during the observations of ID1–3 but less variabilities during those of ID4 and 5. These changes were consistent with passages through regions of low geomagnetic cut-off-rigidities. The average rates are shown in Table 5.1. That of ID1 increased by ∼23% from the *stable* period to the *pre-flare* period and by a factor of ∼3 during the *flare* period. That of ID2 increased by a factor of ∼3 during the *flare* period, while that of ID3 increased by ∼14% and ∼40% from the *stable* period to the *pre-flare* and *flare* periods, respectively. Those of ID4 and 5 were almost constant during each period. There remain some increases, e.g., by a factor of ∼2 during the *flare* period of ID1 and 2, even after excluding periods where geomagnetic cut-off-rigidities are less than 8 GV, which is stricter than the default value of 4 GV. This indicates that more particles penetrate into the low-Earth orbit through the Earth's magnetosphere. The soft bands of ID1–3 may be affected by such particle-induced backgrounds. Therefore, we quantitatively check their spectral contributions later in Subsection 5.2.3.

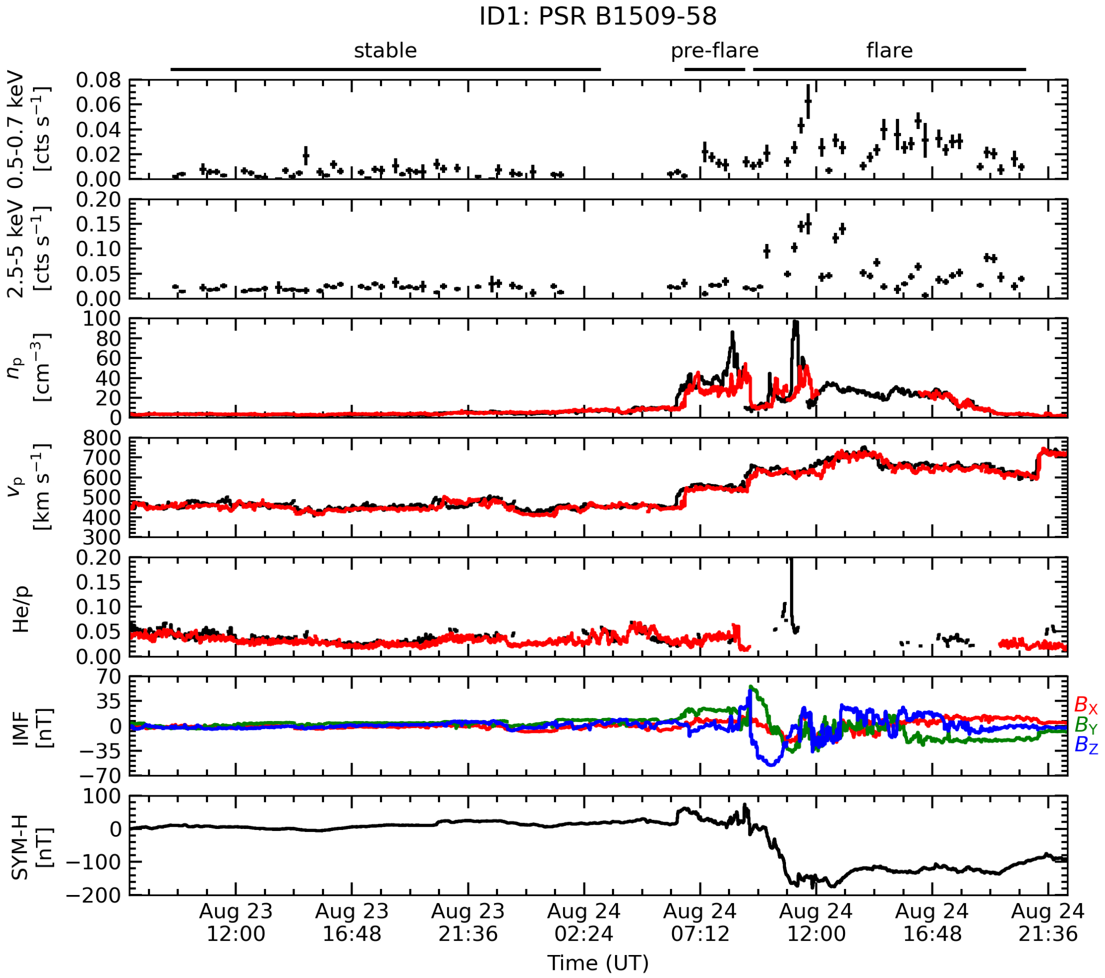

FIGURE 5.1: XIS 1 0.5–0.7 and 2.5–5 keV light curves extracted from the TDX region of ID1, solar wind proton density $n_{\rm p}$, velocity $v_{\rm p}$, helium to proton ratio He/p, IMF $B_{\rm X}$, $B_{\rm Y}$, and $B_{\rm Z}$ in GSM coordinates, and SYM-H index as functions of times in UT. The vertical errors are 1σ significance. The solar wind parameters were taken from the WIND and ACE satellites (black and red). The IMF components were taken from the ACE satellite. The WIND and ACE data were time-shifted to the near-Earth region. The SYM-H index was taken from the World Data Center for Geomagnetism, Kyoto.

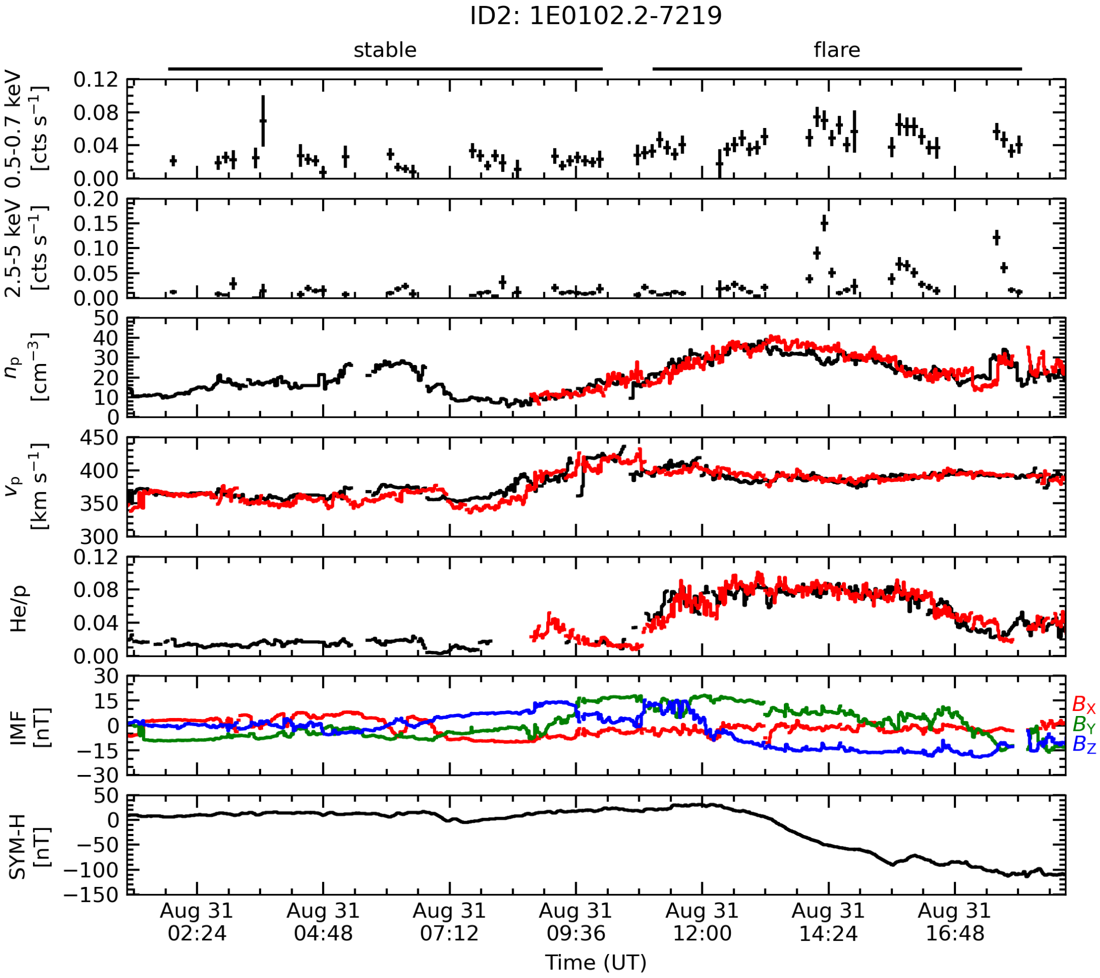

FIGURE 5.2: Same as Figure 5.1, but for ID2.

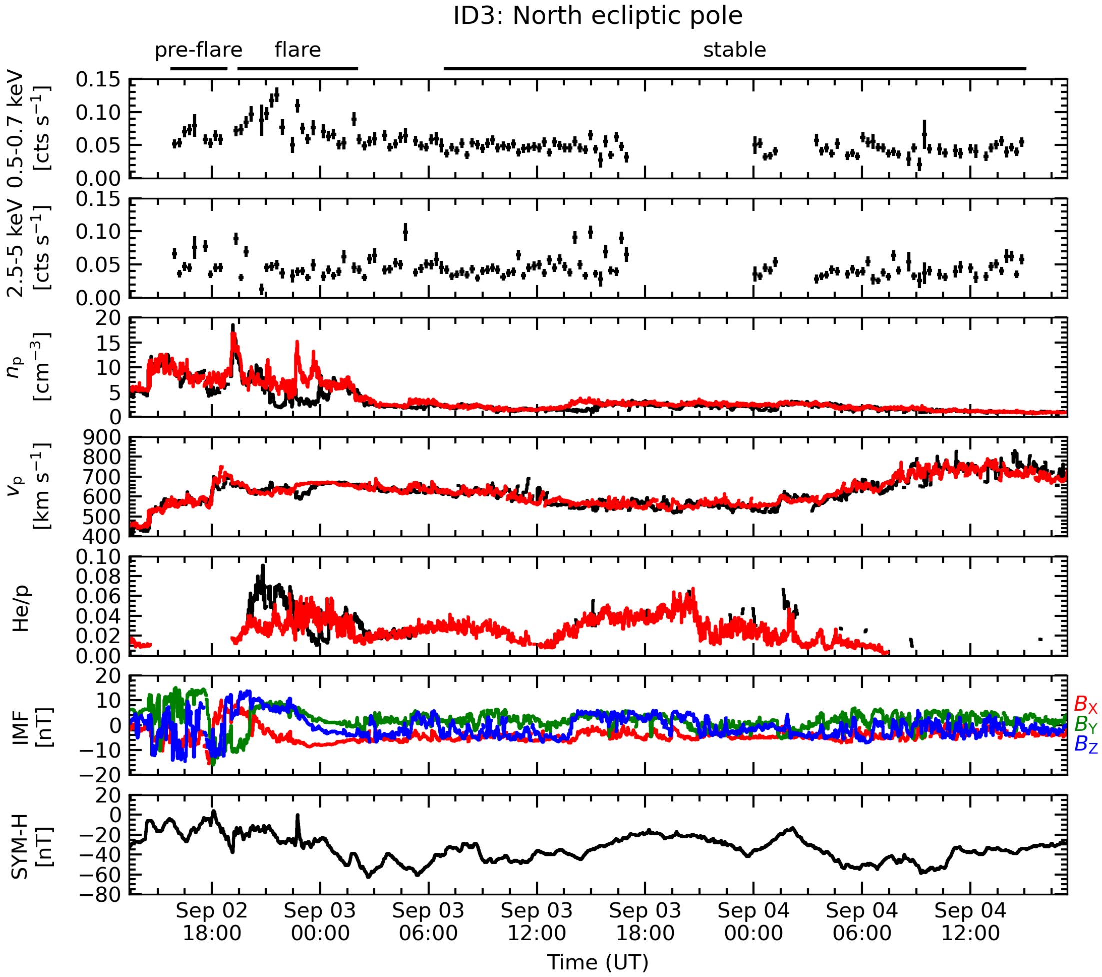
ID3: North ecliptic pole

FIGURE 5.3: Same as in Figure 5.1, but for ID3.

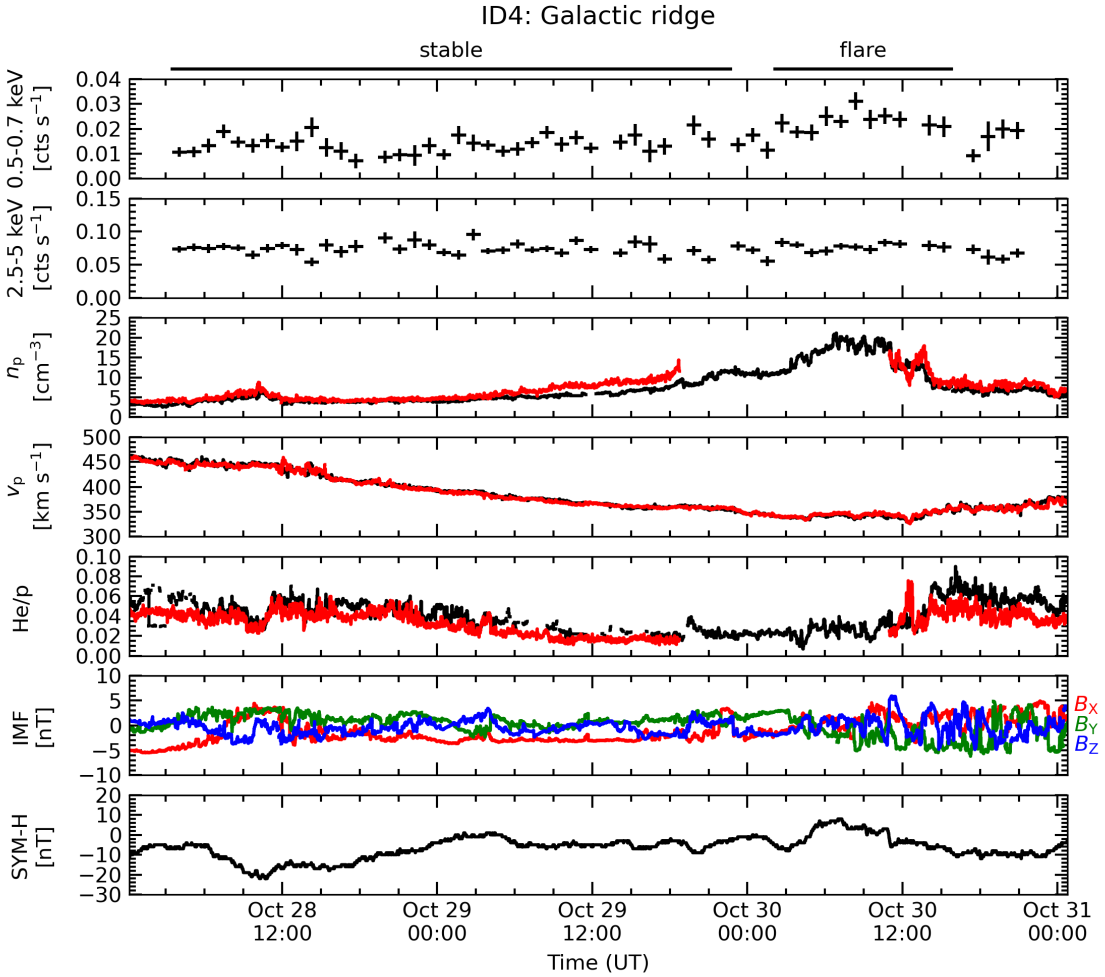

FIGURE 5.4: Same as in Figure 5.1, but for ID4.

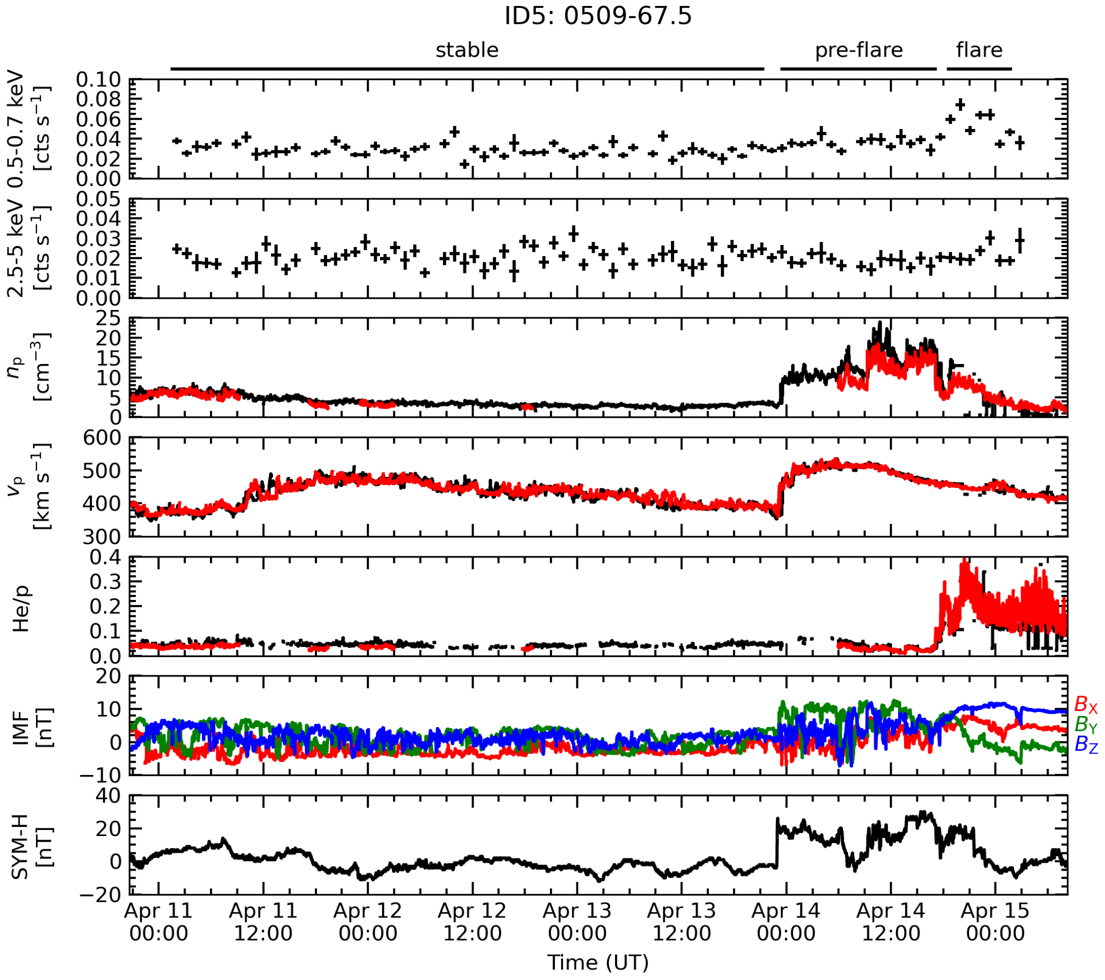

FIGURE 5.5: Same as Figure 5.1, but for ID5.

5.1.1 Solar activities

In Figures 5.1–5.5, we plot three representative solar wind parameters, proton density, velocity, and helium to proton ratio, and interplanetary magnetic field (IMF) components, B_X, B_Y, and B_Z, in geocentric solar magnetic (GSM) coordinates. These data were taken from the WIND and ACE satellites orbiting around the Lagrangian point L_1 between the Sun and Earth and were shifted in time to account for solar wind propagations between the L_1 point to the near-Earth region using the same method described in the OMNIWeb data documentation. The solar wind phase front was assumed to be perpendicular to the ecliptic plane. The orientation of the phase front relative to the Sun–Earth line was determined from an intermediate geometrical consideration between co-rotation and convection. The estimated propagation times were consistent with those obtained from the OMNIWeb data products.

The proton density and velocity show discontinuous changes related to arrivals of CME-induced interplanetary shocks during the observations of ID1, 3, and 5. The velocity rises much further during the second half one of ID3, likely due to higher solar wind streams from a coronal hole. The density shows some increases during those of ID2 and 4, while the velocity increases during that of ID2 but decreases during that of ID4. The former is probably associated with co-rotating interaction regions. The latter might originate from solar wind inter-stream flows. The enhanced helium to proton ratio during those of ID1, 3, and 5 should be related with unusual element and ion abundances within CMEs (e.g., Richardson and Cane, 2004).

The IMF of ID3 and 5 shows intense fluctuations just after the interplanetary shocks and smoothly rotating components of magnetic clouds during the passages of the CME itself. That of ID1 shows no fluctuations within the turbulent sheath but smooth magnetic fields within the magnetic cloud.

5.1.2 Geomagnetic activities

We plot the SYM-H index provided by the World Data Center for Geomagnetism, Kyoto, Japan, which is a measure of geomagnetic disturbances at mid-latitudes, similar to the disturbance storm time (Dst) index but with a much higher time resolution. Negative values indicate that a geomagnetic storm is in progress with an enhanced westward ring current around the Earth (see Kanekal and Miyoshi, 2021).

The SYM-H index reached less than -100 nT on 2005 August 24 and 2005 August 31, i.e., during the observations of ID1 and 2, which is classified as a major geomagnetic storm. These storms are associated with increased solar wind velocities and enhanced southward magnetic fields. That of ID3 experienced a moderate storm with minimum values of -50 nT on 2005 September 3–4. This storm is probably due to higher velocities but no southward magnetic fields within the magnetic cloud. No fluctuations of magnetic fields and lower velocities resulted in less deflections during that of ID4. There were no dramatic decreases because magnetic fields remained northward within the magnetic cloud with lower velocities during that of ID5. The compression of the magnetopause resulted in positive values and changes just after the interplanetary shocks of ID1, 3, and 5.

5.2 Spectra

We extracted spectra from the TDX region during the *stable*, *pre-flare*, and *flare* periods. These spectra include instrument and sky backgrounds. The former remains almost constant during each observation thanks to the low-Earth orbit of Suzaku. The latter consists mainly of diffuse Galactic and extragalactic emissions. Their spectral features do not vary temporally. Therefore, we assumed background components to be constant during each observation.

5.2.1 *Pre-flare* periods

Figure 5.6 shows spectra produced by subtracting the *stable* period from the *pre-flare* period, representing enhanced components during the *pre-flare* period. These spectra contained oxygen emission lines between 0.5 and 0.7 keV. There were some emission lines constituted of highly ionized carbon and nitrogen below 0.5 keV. We fitted each spectrum with a theoretical model constructed by Bodewits et al. (2007). This model includes cross sections for transition lines from highly charged ions (C_{V}, C_{VI}, N_{VI}, $\mathrm{N}_{\mathrm{VII}}$, $\mathrm{O}_{\mathrm{VII}}$, and $\mathrm{O}_{\mathrm{VIII}}$) in collision with atomic hydrogen for several velocities. The normalization of the principal transition with the largest cross section in each ion was considered to be a free parameter, while those of the other transitions were fixed according to the relative cross sections of each principal transition. For each spectral fitting, we adopted a collision velocity of 600 km s^{-1}, which is close to average solar wind velocities during the *pre-flare* period. We added an extra Gaussian to reproduce the lowest-energy emission line around 0.25 keV. The best-fit parameters are summarized in Table 5.2.

5.2.2 *Flare* periods

We subtracted the *stable* period from the *flare* period. Figures 5.7 and 5.8 show the resultant spectra for individual observations. These spectra contained a series of emission lines from highly ionized carbon, nitrogen, and oxygen between 0.3 and 0.7 keV. We fitted each spectrum with the Bodewits model and one or two extra Gaussians around 0.25 keV. We adopted a collision velocity of 400 km s^{-1} for the spectral fittings of ID2, 4, and 5 and that of 600 km s^{-1} for those of ID1 and 3. The spectra of ID3 and 5 showed some excess emission lines from highly ionized neon, magnesium, and silicon above 0.7 keV. Therefore, we added 14 narrow Gaussians detected by Carter et al. (2010), representing such emission lines between 0.7 and 2 keV. The other ones showed no significant excess emission lines above 1 keV. The best-fit parameters are summarized in Table 5.3.

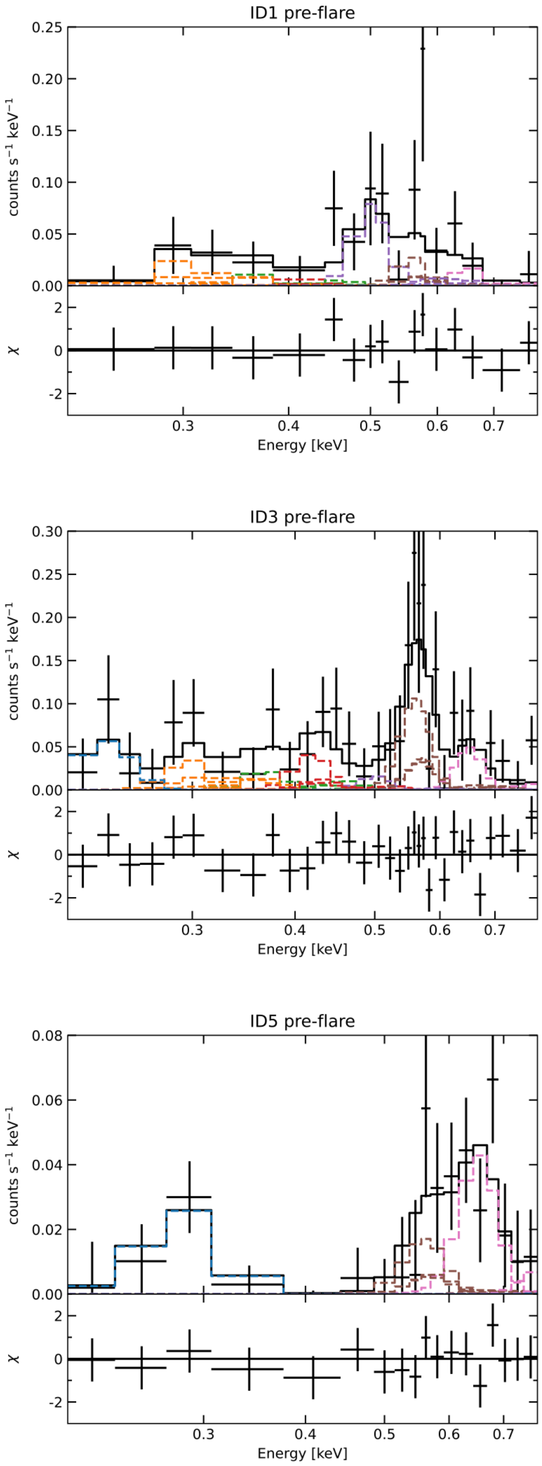

FIGURE 5.6: XIS 1 spectra during the *pre-flare* period of ID1, 3, and 5. The *stable* spectrum during each observation is subtracted as a background. The Bodewits model and a narrow Gaussian reproducing the lowest-energy line are used. Their parameters are listed in Table 5.2.

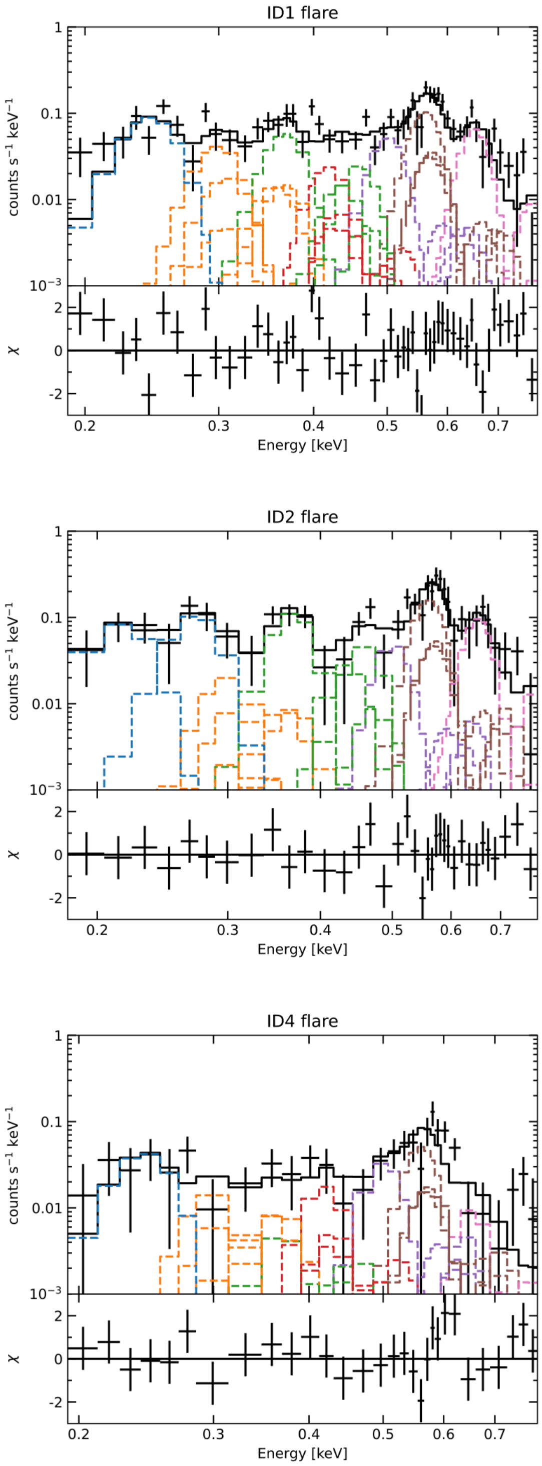

FIGURE 5.7: XIS 1 spectra during the *flare* period of ID1, 2, and 4. The *stable* spectrum during each observation is subtracted as a background. The Bodewits model and one or two narrow Gaussians reproducing the lowest-energy lines are used. Their parameters are listed in Table 5.3.

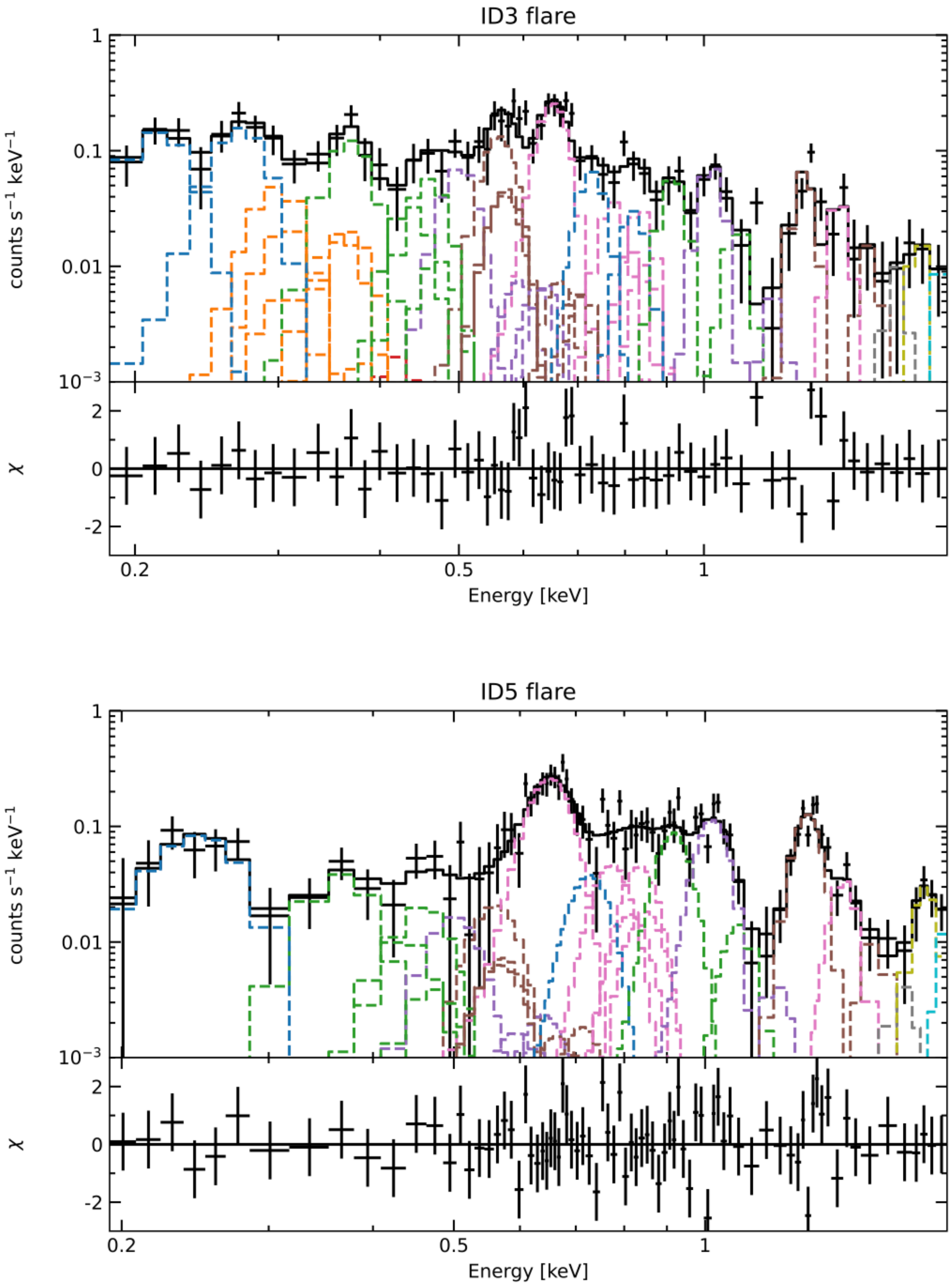

FIGURE 5.8: XIS 1 spectra during the *flare* period of ID3 and 5. The *stable* spectrum during each observation is subtracted as a background. The Bodewits model, one or two narrow Gaussians reproducing the lowest-energy lines, and 14 narrow Gaussians reproducing emission lines at higher energies are used. Their parameters are listed in Table 5.3.

TABLE 5.2: Best-fitting parameters of the spectra shown in Figure 5.6.*

		ID1	ID3	ID5
C band lines	E_c †	–	236^{+16}_{-49}	283^{+2}_{-21}
	Norm.‡	–	4.7 ± 4.5	$5.9^{+3.4}_{-3.5}$
C V (299 eV)	Norm.‡	128 ± 106	28 ± 20	–
C VI (367 eV)	Norm.‡	7.8 (<25.2)	2.2 (<5.5)	–
N VI (420 eV)	Norm.‡	3.9 (<13.7)	2.9 ± 2.1	–
N VII (500 eV)	Norm.‡	19 ± 11	0.56 (<2.03)	–
O VII (561 eV)	Norm.‡	11 (<23)	5.9 ± 2.1	5.6 ± 3.9
O VIII (653 eV)	Norm.‡	4.2 (<12.0)	1.5 ± 1.3	5.8 ± 2.3
χ^2/d.o.f		10.32/11	24.62/25	7.97/14
Power-law	Photon index Γ	–	$0.35^{+0.68}_{-0.35}$	–
	Norm.§	–	1.0 ± 0.5	–
χ^2/d.o.f		–	22.46/33	–

* All the line widths are fixed at 0 eV.

† E_c is the line center energy in units of eV.

‡ Normalization in units of photons s^{-1} cm^{-2} str^{-1}.

§ Normalization in units of photons s^{-1} cm^{-2} str^{-1} keV^{-1} at 1 keV.

TABLE 5.3: Best-fitting parameters of the spectra shown in Figures 5.7 and 5.8.*

		ID1	ID2	ID3	ID4	ID5
C band lines	E_c	244^{+6}_{-8}	216^{+8}_{-14}	213^{+4}_{-6}	242^{+14}_{-20}	246^{+6}_{-8}
	Norm.	44 ± 10	40 ± 19	20 ± 6	$5.0^{+2.7}_{-2.8}$	38 ± 11
C band lines	E_c	–	271^{+6}_{-11}	268^{+5}_{-6}	–	–
	Norm.	–	20 ± 8	7.8 ± 2.3	–	–
C $_{\mathrm{V}}$ (299 eV)	Norm.	191 ± 47	55^{+50}_{-52}	40^{+16}_{-17}	30 ± 18	–
C $_{\mathrm{VI}}$ (367 eV)	Norm.	35^{+8}_{-9}	38 ± 9	12 ± 3	0.89 (<3.32)	25 ± 8
N $_{\mathrm{VI}}$ (420 eV)	Norm.	11 ± 5	–	0.12 (<1.69)	2.1 ± 1.5	–
N $_{\mathrm{VII}}$ (500 eV)	Norm.	13 ± 4	6.7 ± 4.6	2.5 ± 1.2	1.8 ± 0.9	2.9 (<6.5)
O $_{\mathrm{VII}}$ (561 eV)	Norm.	41^{+5}_{-6}	33 ± 6	7.4 ± 1.6	$4.0^{+1.2}_{-1.1}$	6.7 ± 5.2
O $_{\mathrm{VIII}}$ (653 eV)	Norm.	15^{+4}_{-3}	11 ± 5	7.6 ± 1.2	0.41 (<1.04)	34 ± 4
Fe $_{\mathrm{XVII}}$ (730 eV)	Norm.	–	–	1.4 ± 0.6	–	2.9 ± 1.9
Fe $_{\mathrm{XVII}}$ (820 eV)	Norm.	–	–	0.55 ± 0.49	–	–
Fe $_{\mathrm{XVIII}}$ (870 eV)	Norm.	–	–	–	–	–
Ne $_{\mathrm{IX}}$ (920 eV)	Norm.	–	–	1.0 ± 0.4	–	4.5 ± 1.2
Fe $_{\mathrm{XX}}$ (960 eV)	Norm.	–	–	–	–	–
Ne $_{\mathrm{X}}$ (1022 eV)	Norm.	–	–	1.3 ± 0.4	–	5.2 ± 0.9
Ne $_{\mathrm{IX}}$ (1100 eV)	Norm.	–	–	0.37 ± 0.30	–	0.62 ± 0.60
Ne $_{\mathrm{X}}$ (1220 eV)	Norm.	–	–	0.10 (<0.35)	–	0.18 (<0.67)
Mg $_{\mathrm{XI}}$ (1330 eV)	Norm.	–	–	1.1 ± 0.3	–	5.1 ± 0.7
Mg $_{\mathrm{XII}}$ (1470 eV)	Norm.	–	–	0.64 ± 0.29	–	1.4 ± 0.5
Mg $_{\mathrm{XI}}$ (1600 eV)	Norm.	–	–	0.35 ± 0.29	–	0.55 ± 0.42
Al $_{\mathrm{XIII}}$ (1730 eV)	Norm.	–	–	0.22 (<0.52)	–	0.22 (<0.64)
Si $_{\mathrm{XIII}}$ (1850 eV)	Norm.	–	–	0.39 ± 0.27	–	1.4 ± 0.5
Si $_{\mathrm{XIV}}$ (2000 eV)	Norm.	–	–	0.31 (<0.66)	–	1.2 ± 1.1
χ^2/d.o.f		77.95/44	23.17/27	49.22/43	27.86/22	77.41/66
Power-law	Photon index Γ	-0.20 ± 0.05	$0.04^{+0.10}_{-0.09}$	$0.19^{+0.16}_{-0.13}$	–	–
	Norm.	25 ± 2	10 ± 1	2.4 ± 0.4	–	–
χ^2/d.o.f		161.82/157	39.92/32	27.33/19	–	–

* Definitions of parameters are the same as in Table 5.2.

5.2.3 Particle backgrounds

The spectra of ID1–3 have a potential influence of enhanced particle backgrounds. Similar particle-induced backgrounds have been observed in past geocoronal SWCX events most probably due to soft protons funneled by the telescope onto the detector as described in Carter et al. (2010). These particles can produce spectrally featureless signals in the wide band and throughout the entire field of view. Therefore, we fitted each spectrum with a power-law model. The spectrum during the *pre-flare* period of ID1 showed no significant excess components in the 1–5 keV band due to poor photon statistics (on an exposure time of $\sim$3 ks). Those during the *flare* period of ID1 and 2 had some excess components in the 1–5 keV band, while those during the *pre-flare* and *flare* periods of ID3 had some excess components in the 1–5 and 2–5 keV bands, respectively. The other ones showed no significant excess components in the hard band. The fitting results are summarized in Tables 5.2 and 5.3.

The above power-law continuum shows a correlation between its spectral hardness and intensity, which becomes harder and stronger during intense geomagnetic storms as shown in Figure 5.9. This supports the idea that the enhanced particle populations in the Earth's magnetosphere during geomagnetic storms penetrate into an observer's line of sight through closed magnetic field lines (e.g., Walsh et al., 2014).

We then extrapolated the above power-law continuum into the soft bands of ID1–3. The normalizations of $\mathrm{O\,{\scriptstyle VII}}$ and $\mathrm{O\,{\scriptstyle VIII}}$ emission lines during the *pre-flare* period of ID3 reduced by $\sim$2% and $\sim$11%, respectively, while those during the *flare* periods of ID1–3 by $\sim$6% and $\sim$18%, $\sim$3% and $\sim$13%, and $\sim$3% and $\sim$4%. These reductions are within the 90% confidence range listed in Tables 5.2 and 5.3. The enhanced particle backgrounds are almost negligible in the soft bands of ID1–3.

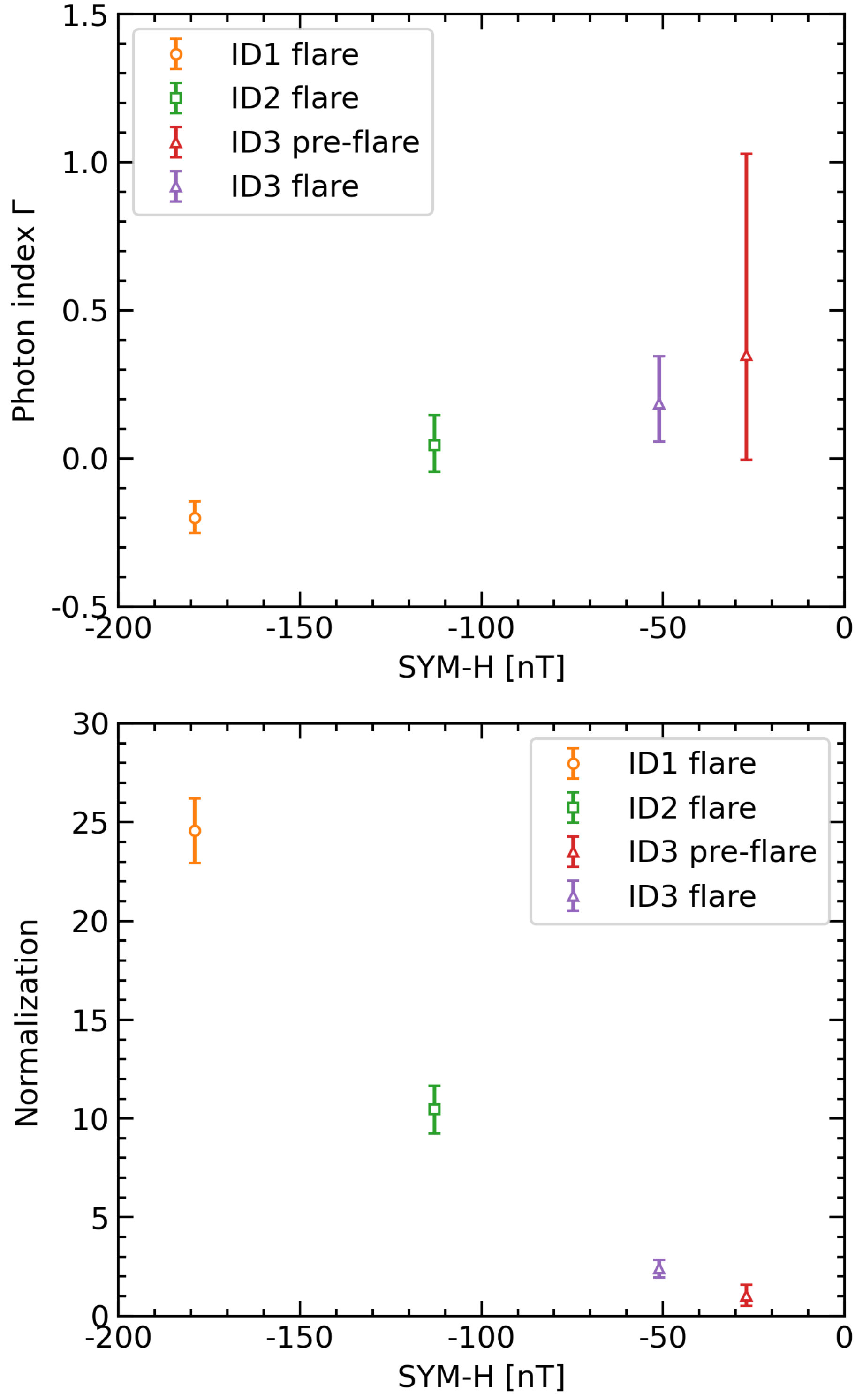

FIGURE 5.9: Comparisons between minimum values of SYM-H index and power-law model parameters listed in Tables 5.2 and 5.3.

Chapter 6

Geocoronal SWCX model

This chapter describes how to model geocoronal SWCX emission. This emission can be estimated from integral of emissivities along an observer's line of sight. For a single ion species, its intensity is expressed by the following equation:

$$I_{\mathrm{SWCX}} = \frac{1}{4\pi} \int n_{\mathrm{H}}\, n_{\mathrm{ion}}\, v_{\mathrm{ion}}\, \alpha\, ds, \tag{6.1}$$

where n_{H} is the density of the neutral hydrogen atom in the Earth's exosphere, n_{ion} and v_{ion} correspond to the density and the velocity of the solar wind ion species of interest, α accounts for the charge exchange cross section and transition probability for relevant emission lines, and ds is the step length of integration. Below we explain these parameters.

6.1 Exospheric neutral hydrogen distribution

To describe neutral exospheric densities as a function of radial distances from the Earth, we used the simplified formula of Cravens et al. (2001): $n_{\mathrm{H}} = n_{\mathrm{H0}}\ (10\ R_{\mathrm{E}}/r)^3$ with $n_{\mathrm{H0}} = 25\ \mathrm{cm}^{-3}$, which is an approximation of results from Monte Carlo simulations for several values of insolation at solstice and equinox (Hodges Jr., 1994). The Hodges model is compatible with some measurements of hydrogen distributions using Lyman-α column brightnesses from the night side of the Earth (e.g., Østgaard et al., 2003).

There are several models of exospheric densities deduced from remote observations using Lyman-α (e.g., Bailey and Gruntman, 2011; Baliukin et al., 2019), energetic neutral atoms (e.g., Fuselier et al., 2010), and soft X-rays (e.g., Connor and Carter, 2019), showing various densities ranging roughly from 5 to 50 cm^{-3} at 10 R_{E}. The simplified formula that we adopted is an intermediate of these different models. We tested each model and found that these uncertainties can change line intensities by a factor of $\sim$2–3.

6.2 Solar wind ion data

The O VII emission lines are produced by O^{7+} ions undergoing charge exchange to become O^{6+} ions in excited states, while the O VIII emission lines are produced by O^{8+} ions. These ion densities can be deduced from that of solar wind proton multiplied by helium to proton ratio, oxygen to helium ratio, and oxygen charge state fraction of interest:

$$n_{\mathrm{O^{q+}}} = n_{\mathrm{p}} \left[\frac{\mathrm{He}}{\mathrm{p}}\right] \left[\frac{\mathrm{O}}{\mathrm{He}}\right] \left[\frac{\mathrm{O^{q+}}}{\mathrm{O}}\right], \tag{6.2}$$

where the proton density can be obtained from the OMNIWeb data products where cross-calibration issues between WIND/SWE and ACE/SWEPAM have already been handled.

The He/p ratio can be taken from WIND/SWE and ACE/SWEPAM. The ACE/SWEPAM He/p ratio suffers from a significant problem (see “Important Notes” of the OMNIWeb data documentation). The WIND/SWE He/p ratio may be more appropriate.

The other parameters are only available from ACE/SWICS. We used SWICS 1.1 level 2 version 4.09 data processed on 2015 June 8. The instrument team of ACE/SWICS estimated uncertainties of 30% for most parameters (see release notes). Below we describe solar wind ion data during each observation.

- ID1: The WIND/SWE He/p ratio was sparse during most of the observation except for a part of the *stable* period. The ACE/SWEPAM He/p ratio was lacking during the *flare* period. Therefore, we used the ACE/SWICS He/p ratio during the entire observation. The ACE/SWICS O/He ratio and oxygen charge state fractions were available.

- ID2: The WIND/SWE He/p ratio was lacking during a part of the *stable* period. Therefore, we used the ACE/SWEPAM He/p ratio during a part of the *stable* period. The ACE/SWICS He/p ratio was used during periods where the ACE/SWEPAM He/p ratio was not available. The ACE/SWICS O/He ratio and oxygen charge state fractions were available.

- ID3: The WIND/SWE He/p ratio was sparse during most of the observation except for the *flare* period. Therefore, we used the ACE/SWEPAM He/p ratio during most of the observation except for the *flare* period. The ACE/SWICS He/p ratio was used during periods where the ACE/SWEPAM He/p ratio was not available. The ACE/SWICS O/He ratio and oxygen charge state fractions were available.

- ID4: The WIND/SWE He/p ratio was available during the entire observation. The ACE/SWICS O/He ratio and oxygen charge state fractions were available.

- ID5: The WIND/SWE He/p ratio was sparse during the *flare* period. Therefore, we used the ACE SWEPAM He/p ratio during the *flare* period. The ACE/SWICS O/He ratio and oxygen charge state fractions were not available after hardware anomalies altered instrumental operational states on 2011 August 23. We thus refer to slow (442 km s^{-1}) and fast (810 km s^{-1}) solar wind ion abundances listed in Schwadron and Cravens (2000). The solar wind velocity ranged roughly from 400 to 500 km s^{-1} during the entire observation. Therefore, we used the slow solar wind values. The He/O ratio was assumed to be 78. The O^{7+}/O and O^{8+}/O ratios were set to 0.20 and 0.07, respectively.

The remaining parameter is oxygen ion velocities. These ion velocities were assumed to be the same as the proton values. Thermal velocities were added in quadrature to them:

$$v_{\mathrm{O}^{q+}} \simeq \sqrt{v_{\mathrm{p}}^{2} + \frac{3k_{\mathrm{B}}T_{\mathrm{p}}}{m_{\mathrm{p}}}}, \tag{6.3}$$

where k_{B} is the Boltzmann constant, T_{p} is the proton temperature, and m_{p} is the proton mass. The proton velocity and temperature can be obtained from the OMNIWeb data products.

6.3 Charge exchange cross section

Charge exchange cross sections and line yields for each transition of O^{7+} (seven transitions) and O^{8+} (five transitions) ions were taken from Bodewits et al. (2007). To obtain values corresponding to a particular collision velocity, we interpolated the tabled values for the five ones (200, 400, 600, 800, and 1000 km s^{-1}). Total cross sections for $\mathrm{O}_{\mathrm{VII}}$ and $\mathrm{O}_{\mathrm{VIII}}$ emission lines are shown in Figure 6.1. The former is almost constant but the latter strongly depends on collision velocities. Bodewits et al. (2007) estimated uncertainties to be approximately 20%.

6.4 Line of sight integration

Magnetosheath plasma populations are responsible for soft X-ray emitters, while magnetospheric ones contain few highly charged ions required to produce soft X-rays. Therefore, we assumed relevant ion densities to be zero inside the magnetopause and outside the bow shock. The magnetopause and bow shock positions were determined from empirical models of Shue et al. (1998) and Merka et al. (2005), respectively. The former is parametrized by the IMF B_Z component in GSM coordinates and the solar wind dynamic pressure, while the latter is parametrized by the upstream Alfvénic

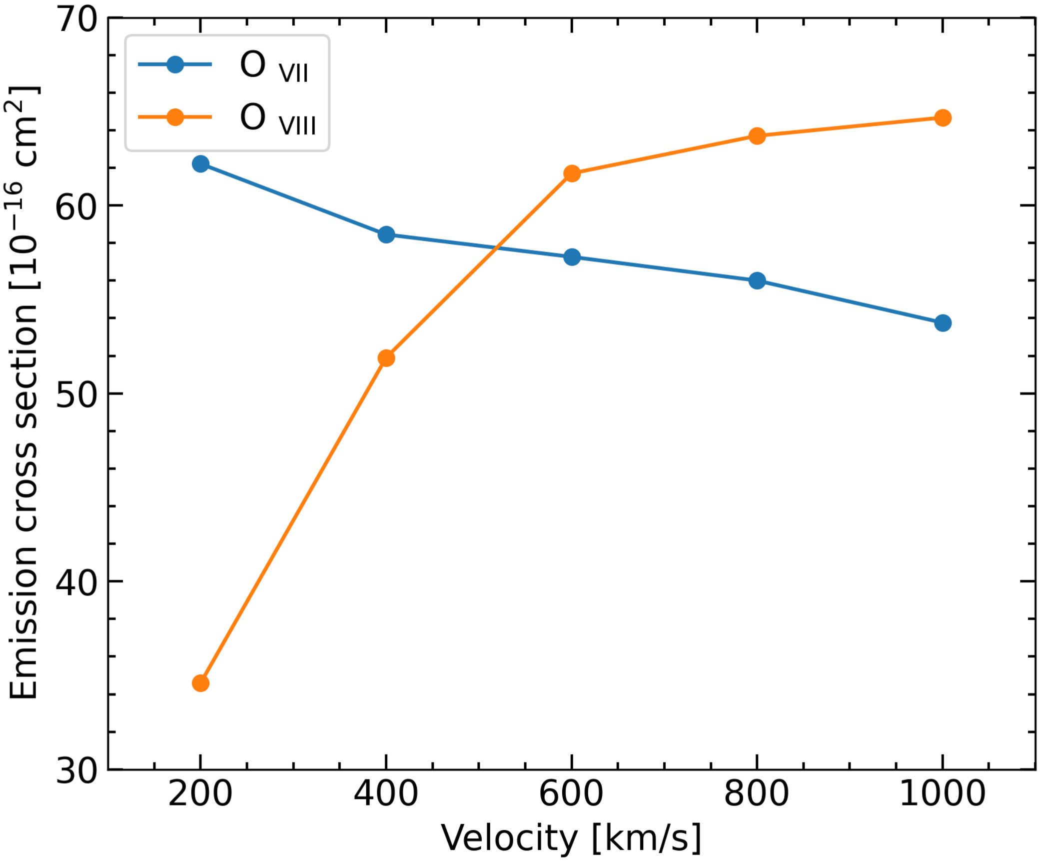

FIGURE 6.1: Total cross sections for O VII and O VIII emission lines after Bodewits et al. (2007).

Mach number. Both models represent average positions for particular solar wind parameters so that abrupt changes, e.g., the interplanetary shock-induced impulses of ID1, 3, and 5, are not easy to consider.

The magnetospheric cusp is a narrow throat of magnetic field lines poleward of the last closed field line on the day side of the Earth. These magnetic field lines are open and allow solar wind plasma to enter deep into the near-Earth region with higher exospheric densities (e.g., Walsh et al., 2016). The magnetopause model does not take into account cusp geometries. Therefore, we used the Earth's magnetic field model (Tsyganenko and Sitnov, 2005 and references therein) to examine whether magnetic field lines along line of sights are closed, open but connected to the north or south poles, or not connected to Earth. The Tsyganenko model is a semi-empirical best-fit representation for the Earth's magnetic field. Its input parameters are the solar wind dynamic pressure, the Dst index, the IMF B_Y and B_Z components in GSM coordinates, and a set of variable weight coefficients provided by TS05 web repository. We traced magnetic field lines along an observer's line of sight and determined points whose magnetic fields are open to the day side of the Earth, i.e., cusp regions where solar wind plasma can exist.

Figure 6.2 shows configuration of our modeled magnetopause, bow shock, and magnetic field lines during the observation of ID3. We thus integrate emissivities at magnetosheath and cusp regions along an observer's line of sight. The solar wind plasma is being shocked downstream of the bow shock. We considered this effect using the Rankine–Hugoniot equations. The polytropic index was set to 1.46 (e.g., Totten et al., 1995). The shocked solar wind plasma was assumed to be uniformly distributed at each integral point along an observer's line of sight.

Provided that magnetic field models have few uncertainties, our model uncertainties are dominated mainly by an exospheric neutral hydrogen distribution model and then by solar wind ion data and charge exchange cross sections. The summed uncertainty is a factor of $\sim$3–5.

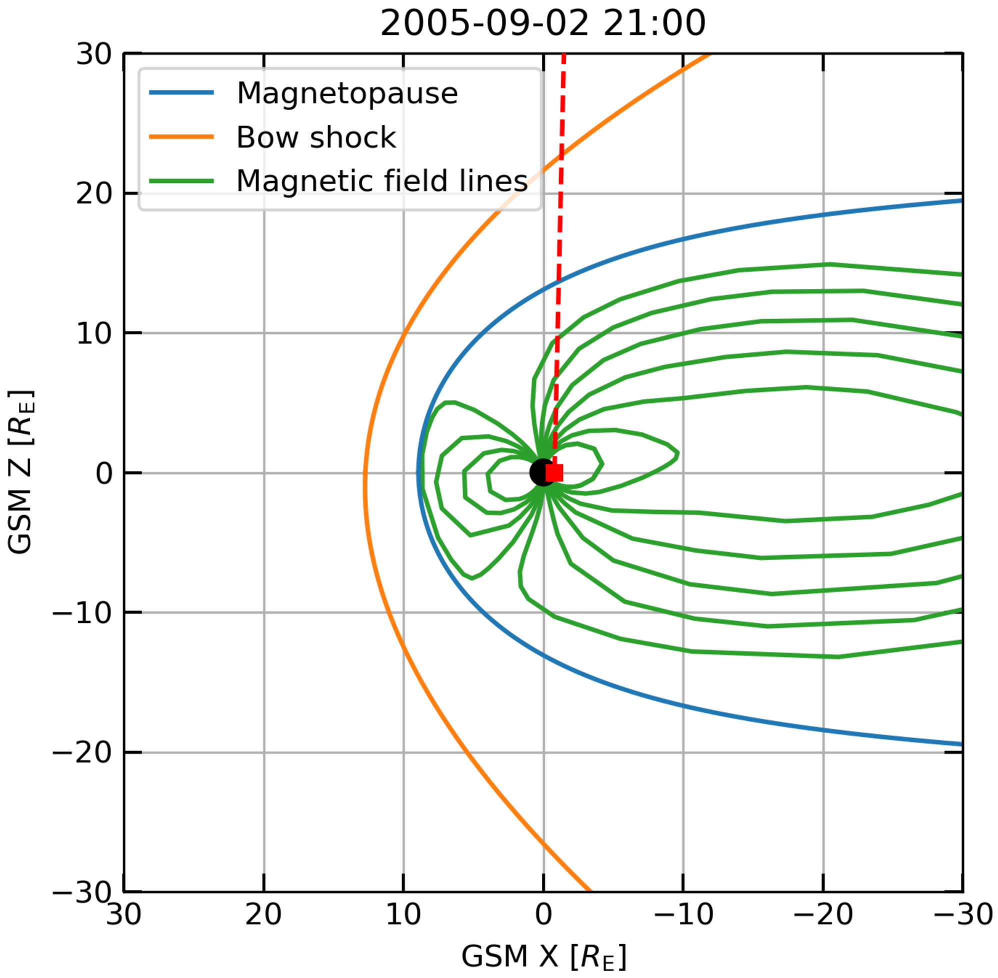

FIGURE 6.2: Example of modeled magnetospheric configuration in GSM XZ plane. The blue, orange, and green lines indicate magnetopause, bow shock, and magnetic field lines. The red square and dotted line represent Suzaku position and line-of-sight direction.

Chapter 7

Discussion

This chapter gives comparison between our observational results and model predictions.

7.1 Average line fluxes

To examine our model accuracy, we estimated average line fluxes during each observation. Table 7.1 gives modeled intensities of O$_{\rm VII}$ and O$_{\rm VIII}$ emission lines during the *stable*, *pre-flare*, and *flare* periods. For comparison with the observed values shown in Tables 5.2 and 5.3, we subtracted the modeled line fluxes during the *stable* period from those during the *pre-flare* and *flare* periods. Figures 7.1 and 7.2 show comparisons and ratios between the observed and modeled intensities for the O$_{\rm VII}$ and O$_{\rm VIII}$ line fluxes during each observation.

7.1.1 O$_{\rm VII}$ emission lines

For the O$_{\rm VII}$ line flux, considering our model uncertainties of a factor of ∼3–5, we found that the model reproduced the data except for the result of ID2. This indicates that our model is useful for estimating the contribution of the O$_{\rm VII}$ emission line. The observation of ID2 may be affected by solar wind injections into the inner magnetosphere during intense geomagnetic storms. Ebihara et al. (2009) suggested that high-charge state oxygen ions were transported to the inner magnetosphere from the night

TABLE 7.1: Model prediction of average line fluxes.[*]

ID	Emission line	*Stable*	*Pre-flare*	*Pre-flare − Stable*[†]	*Flare*	*Flare − Stable*[†]
1	O VII	0.22	9.52	9.30	22.53	22.31
				(11)		(41)
	O VIII	0.005	0.831	0.826	3.709	3.704
				(4.2)		(15)
2	O VII	0.87	–	–	6.88	6.01
				(–)		(33)
	O VIII	0.023	–	–	0.088	0.065
				(–)		(11)
3	O VII	0.16	3.26	3.10	5.91	5.75
				(5.9)		(7.4)
	O VIII	0.006	0.159	0.153	0.268	0.261
				(1.5)		(7.6)
4	O VII	0.47	–	–	7.42	6.95
				(–)		(4.0)
	O VIII	0.011	–	–	0.014	0.003
				(–)		(0.41)
5	O VII	1.73	11.46	9.73	13.62	11.89
				(5.6)		(6.7)
	O VIII	0.35	2.86	2.50	2.65	2.30
				(5.8)		(34)

[*] In units of photons s^{-1} cm^{-2} str^{-1}.
[†] Observed values are shown in parentheses.

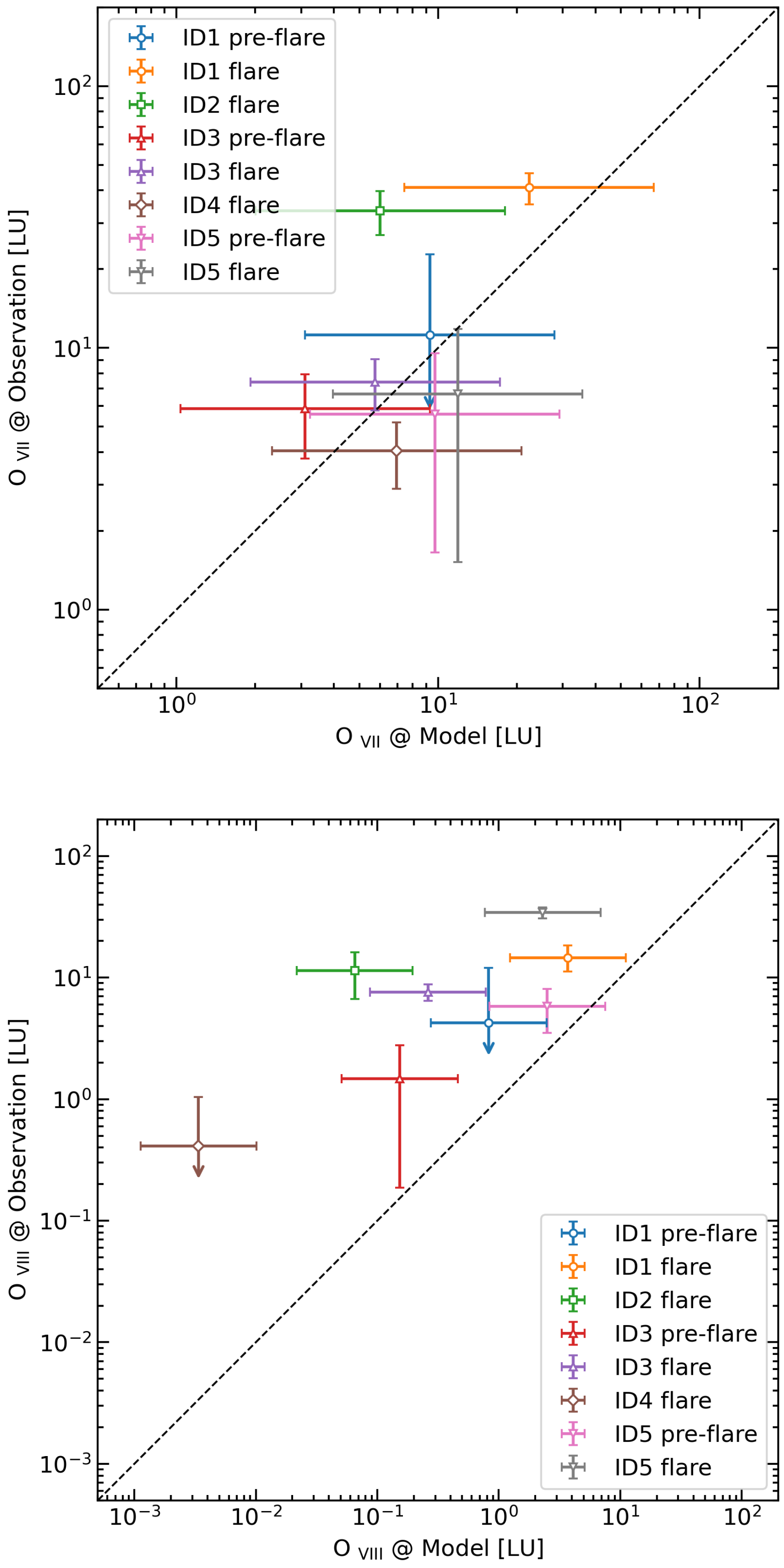

FIGURE 7.1: Comparisons between observation and model for O VII and O VIII line fluxes. The horizontal errors come from model uncertainties of a factor of three.

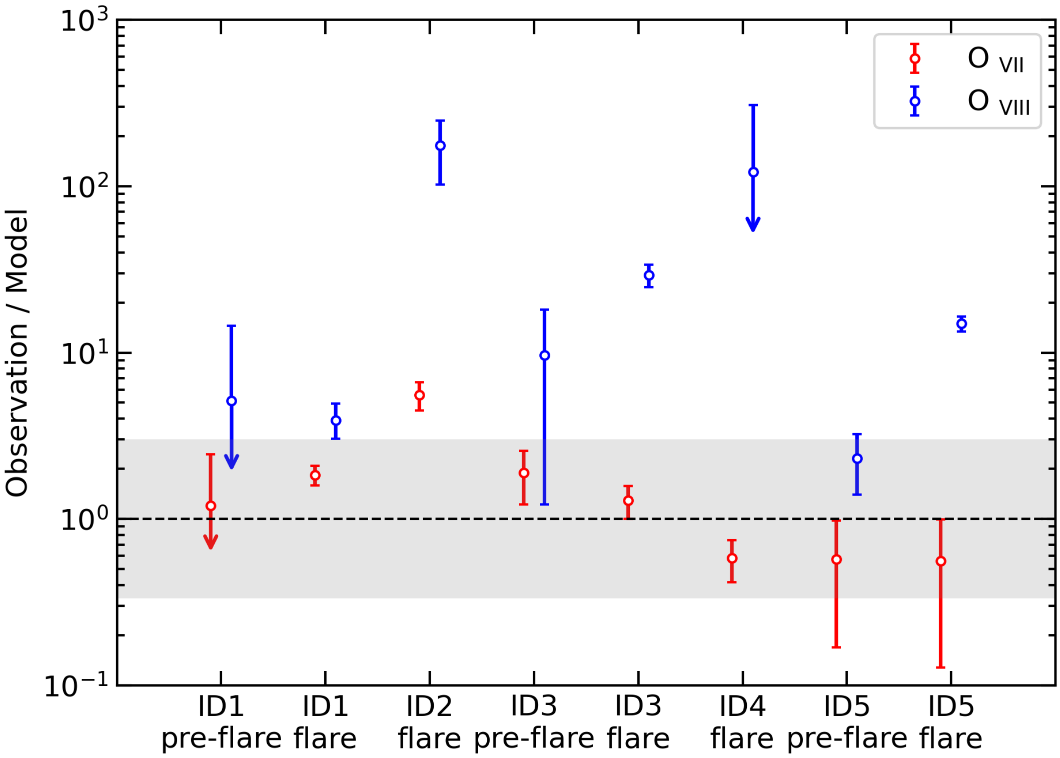

FIGURE 7.2: Ratio of observation to model for O VII and O VIII line fluxes. The black shaded area indicates a ratio within a factor of three.

side of the high-latitude magnetopause during intense geomagnetic storms. This situation seems consistent with our Suzaku observation whose line-of-sight direction was toward the night side of the high-latitude magnetosheath during a major geomagnetic storm reaching less than -100 nT. O^{7+} ions not only in the magnetosheath but also in the inner magnetosphere may be responsible for soft X-ray emitters. On the other hand, abrupt increases of exospheric hydrogen densities during geomagnetic storms have been reported (e.g., Bailey and Gruntman, 2013; Kuwabara et al., 2017). Exospheric responses to geomagnetic storms may also have some responsibilities.

7.1.2 O VIII emission lines

The O VIII line flux was more underestimated compared to the O VII line flux. Even considering our model uncertainties, such large discrepancies can not be explained. This suggests that further uncertainties exist in solar wind ion abundances. The measurement accuracy of O^{8+} ions may be worse than that of O^{7+} ions due to poor counting statistics. Figure 7.3 shows a comparison between the O^{8+}/O^{7+} ion ratio measured by ACE/SWICS and the O VIII/O VII flux ratio deduced from geocoronal SWCX spectra during each observation. The ratios of the Suzaku spectra tend to be larger than those of ACE/SWICS. This supports the idea that O^{8+} ions may be poorly measured by ACE/SWICS. The other reason probably stems from velocity-dependent cross sections for O VIII emission lines. The Kronos cross sections differ from those of Bodewits et al. (2007).

7.2 Modeled light curves

We simulated O VII and O VIII light curves in units of LU. Figures 7.4–7.8 show results of ID1–5. We plot X-ray light curves extracted from the TDX region in the 0.52–0.6 and 0.6–0.7 keV bands along with solar wind proton flux, oxygen to proton ratio, and oxygen ion fractions. The count rate was converted into the line flux per solid angle using the area of the TDX region and the spectral fitting result during the *flare* period.

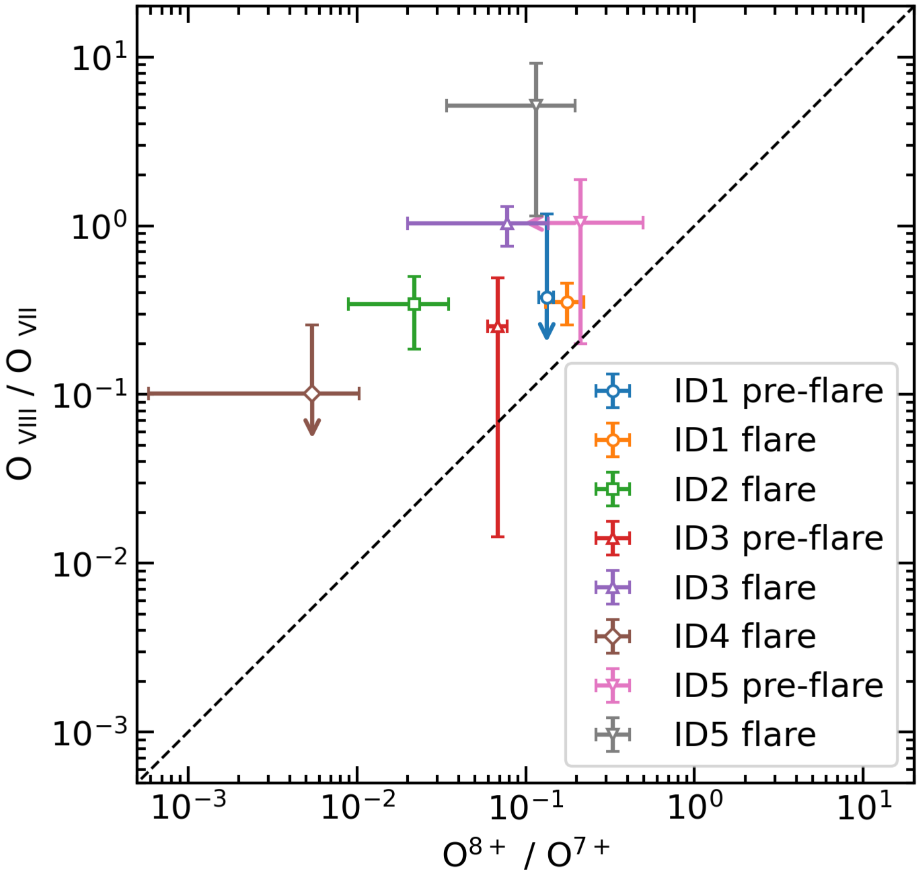

FIGURE 7.3: Comparison between O^{8+}/O^{7+} ion ratio measured by ACE/SWICS and $\mathrm{O\,VIII}/\mathrm{O\,VII}$ flux ratio deduced from geocoronal SWCX spectra.

The modeled light curves with a time bin of 256 s were binned into the same bin of the observed ones and scaled by the ratio between the observed and modeled intensities during the *flare* period. The background flux was estimated from the average rate during the *stable* period.

The above scaled model reproduced the observed temporal variations in the 0.52–0.6 and 0.6–0.7 keV bands except for those during the *pre-flare* period of ID5. This indicates that our model is capable for predicting the O VII and O VIII light curves. The discrepancies of ID5 are most probably due to constant oxygen ion fractions. The time-variable oxygen ion fluxes deduced from an empirical equation improve such discrepancies but its scaling factors become worse as discussed later in Subsection 7.3.2.

In Figures 7.9–7.13, we plot enlarged views with shorter time bins during the *pre-flare* and *flare* period. There are some spike bins due to line-of-sight directions passing through the near-cusp region, e.g., within 3 R_{E}, during the orbital motion of Suzaku. These spikes were reproduced by our scaled model. This supports the idea that the strongest emitters are present in polar cusps and geocoronal SWCX emission is useful for capturing cusp geometries and motions. Below we describe the result for each observation.

- ID1: The O VII and O VIII light curves vary due to increased solar wind proton flux and oxygen ion fractions. The oxygen to proton ratio increases but has fewer contributions to the observed temporal variations. There are some spike bins due to the line of sight direction passing through the southern polar cusp.

- ID2: The O VII and O VIII light curves vary due to increased solar wind proton flux and oxygen to proton ratio. The oxygen ion fractions decrease during the *flare* period. There are some spike bins due to the line of sight direction passing through the southern polar cusp.

- ID3: The O VII and O VIII light curves vary due to increased solar wind proton flux and oxygen to proton ratio. The $\mathrm{O}^{7+}/\mathrm{O}$ ratio increases and has further contributions to the observed temporal variations during the *flare* period. The $\mathrm{O}^{8+}/\mathrm{O}$

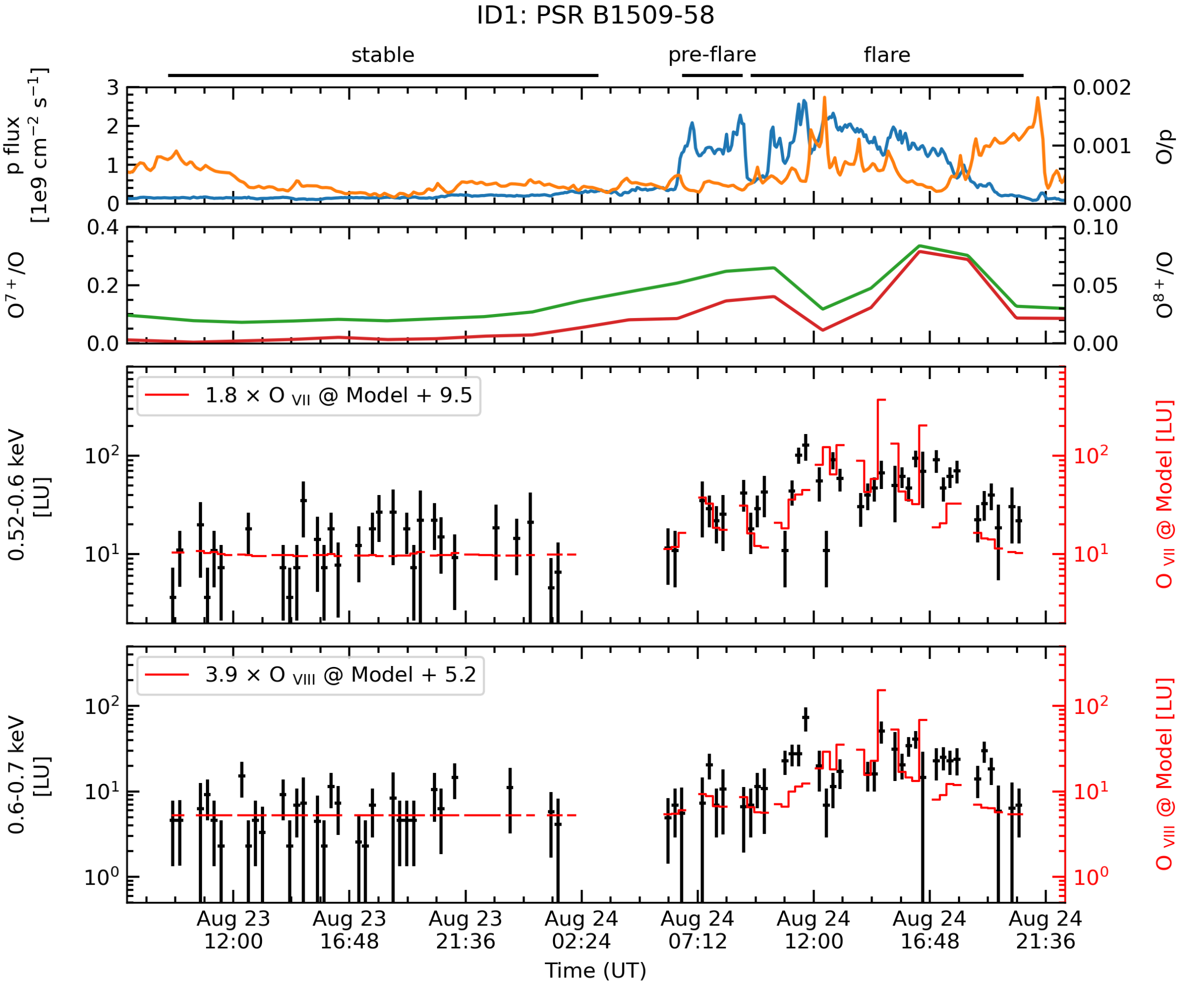

FIGURE 7.4: Solar wind proton flux (blue), oxygen to proton ratio (orange), oxygen charge state fractions for O^{7+} (green) and O^{8+} ions (red), XIS 1 0.52–0.6 and 0.6–0.7 keV light curves extracted from the TDX region of ID1 (black), and model light curves of ID1 for O VII and O VIII emission lines (red). The numbers in boxes indicate scaling factors and background levels in units of LU.

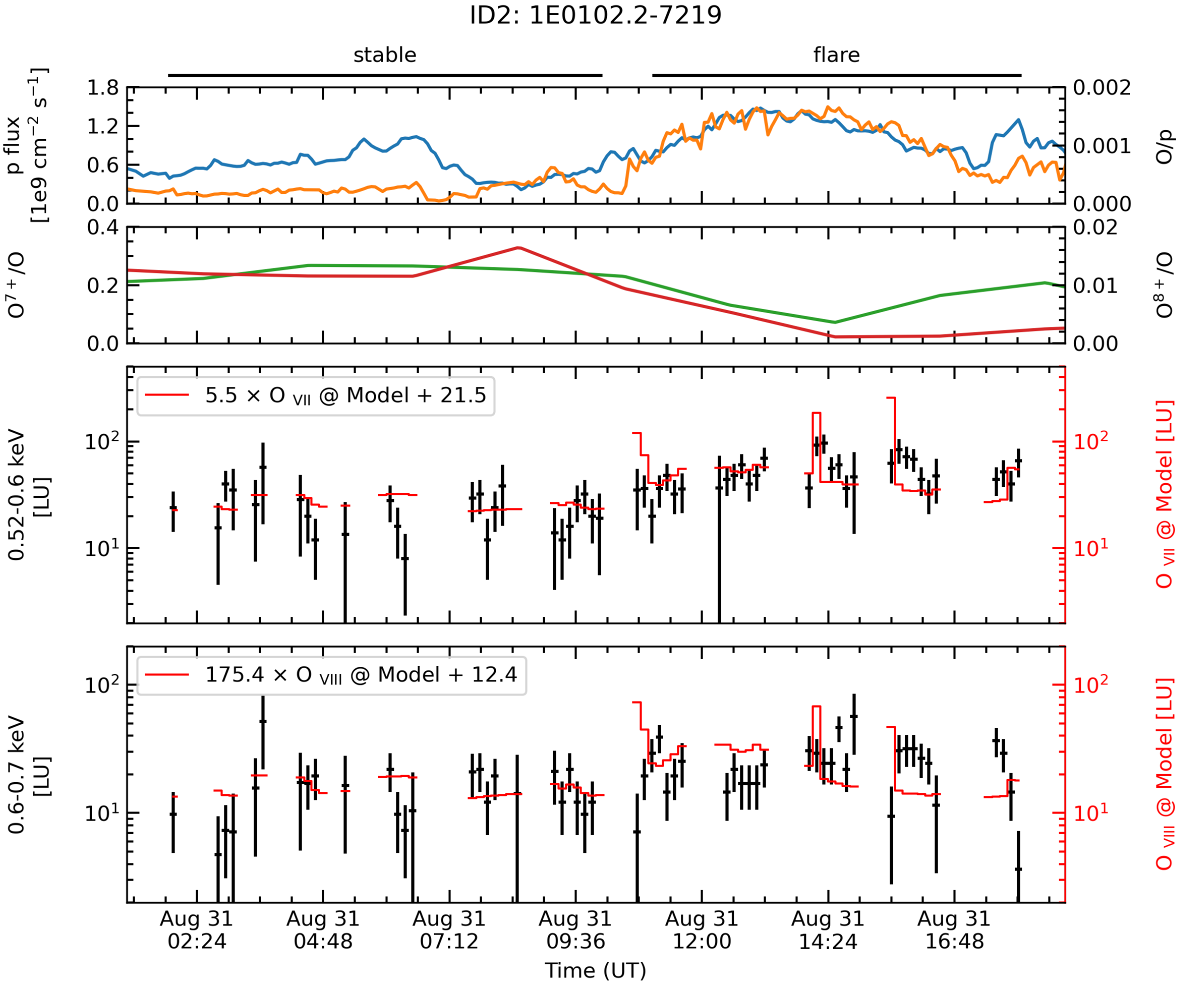

FIGURE 7.5: Same as Figure 7.4, but for ID2.

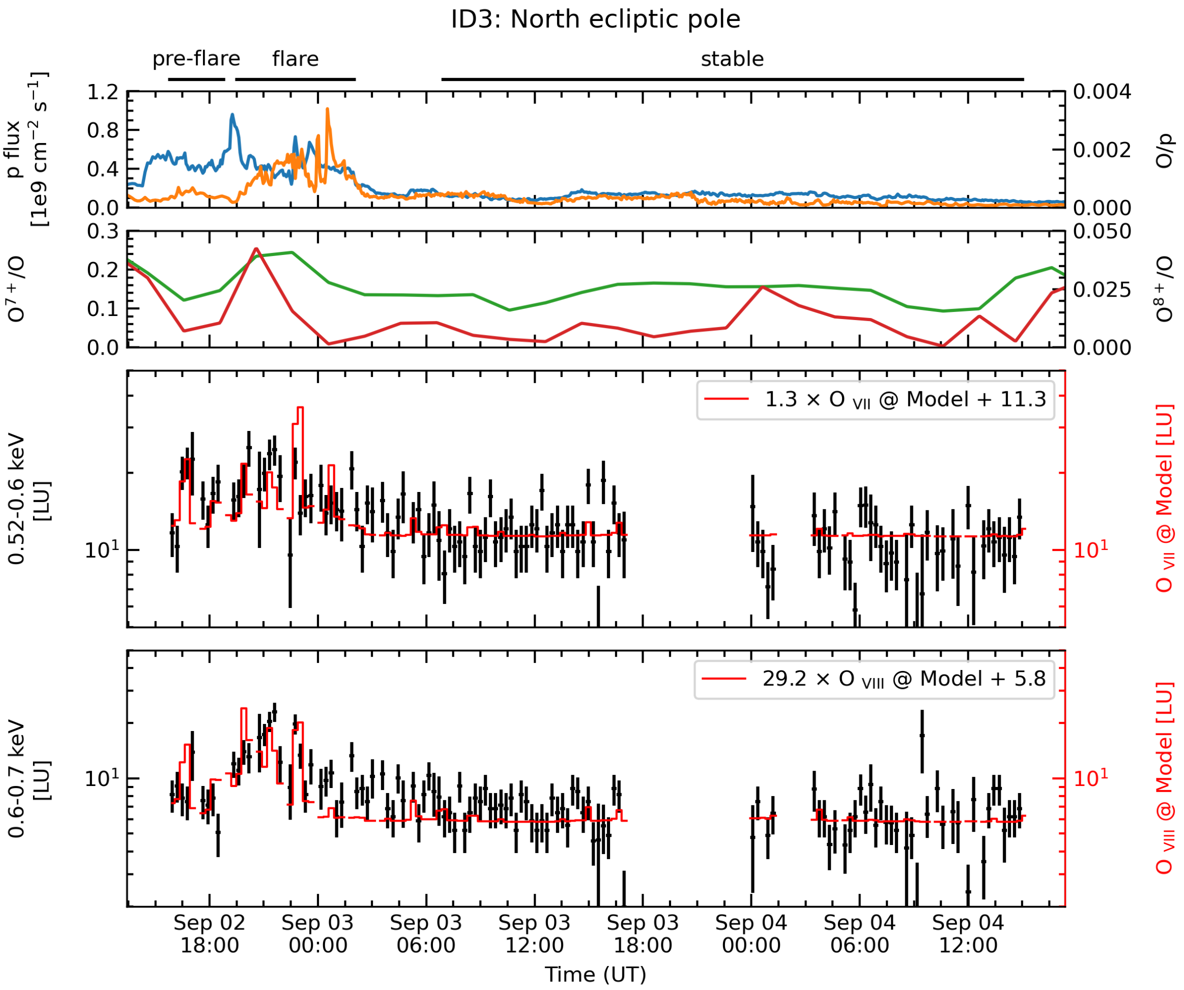

FIGURE 7.6: Same as Figure 7.4, but for ID3.

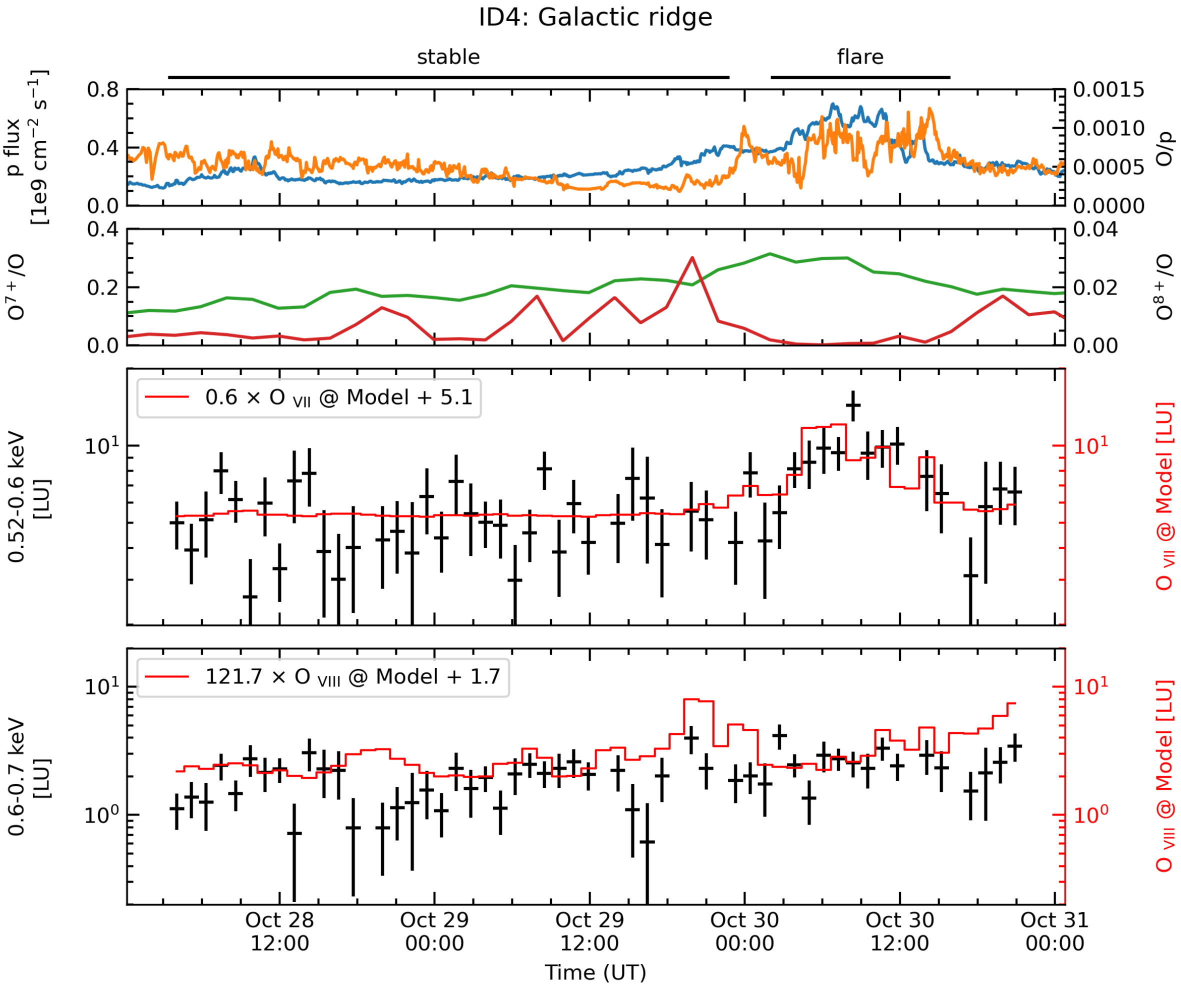

FIGURE 7.7: Same as Figure 7.4, but for ID4.

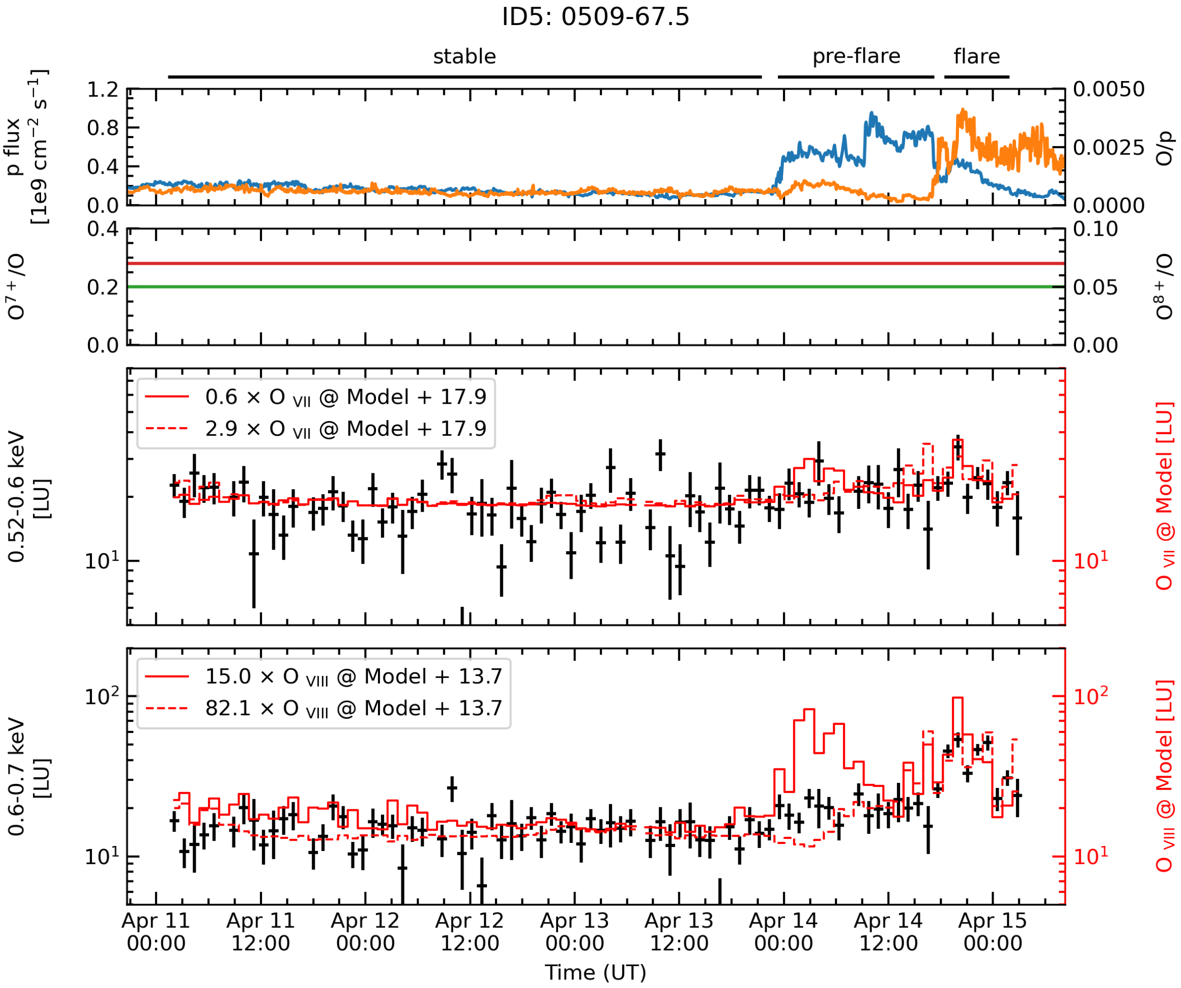

FIGURE 7.8: Same as Figure 7.4, but for ID5. Note that the solid and dotted lines represent model light curves using constant oxygen charge state fractions (Schwadron and Cravens, 2000) and time-variable oxygen ion fluxes deduced from an empirical equation (Kaaret et al., 2020).

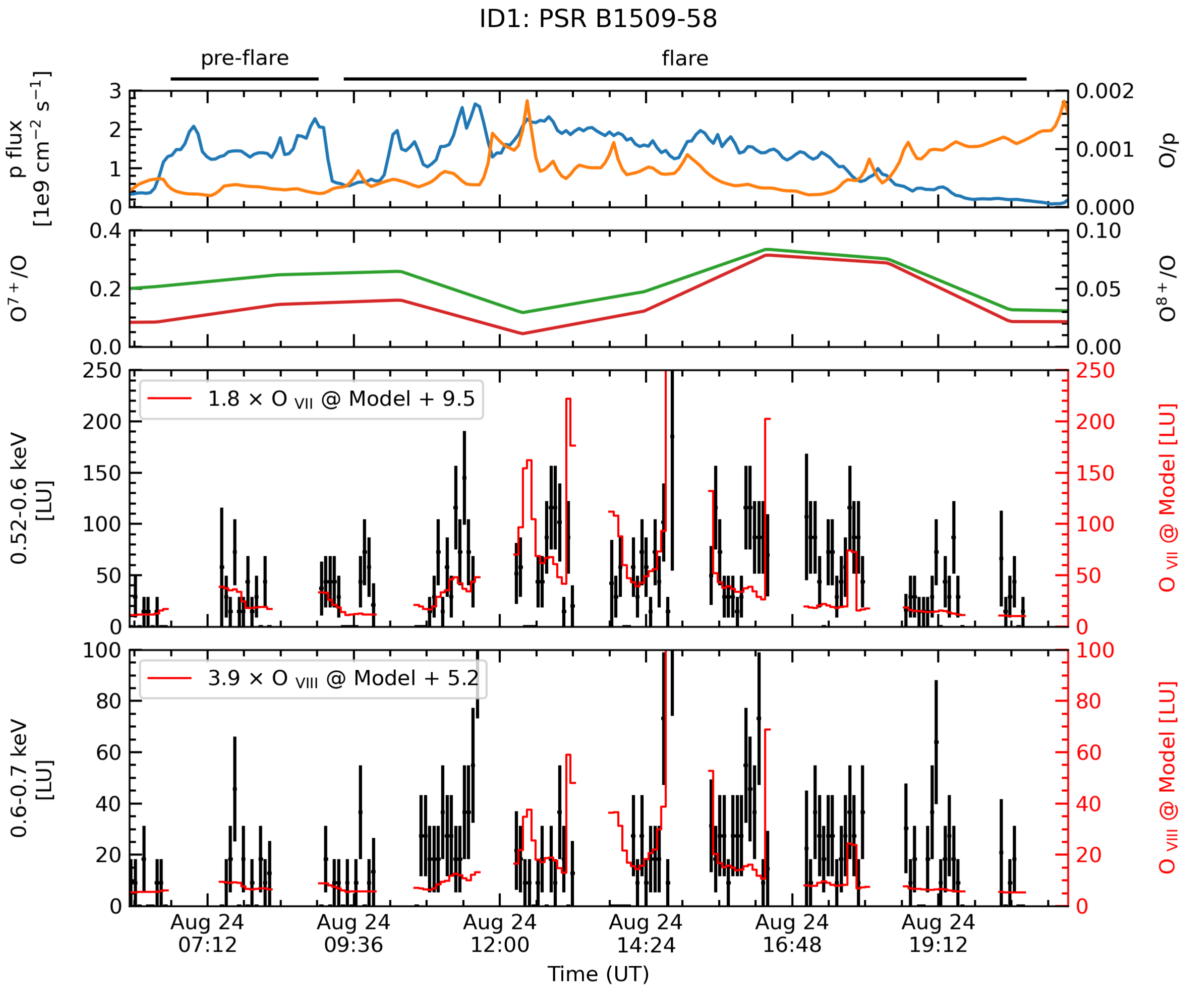

FIGURE 7.9: Enlarged view during the *pre-flare* and *flare* periods of Figure 7.4. The time bin is much shorter.

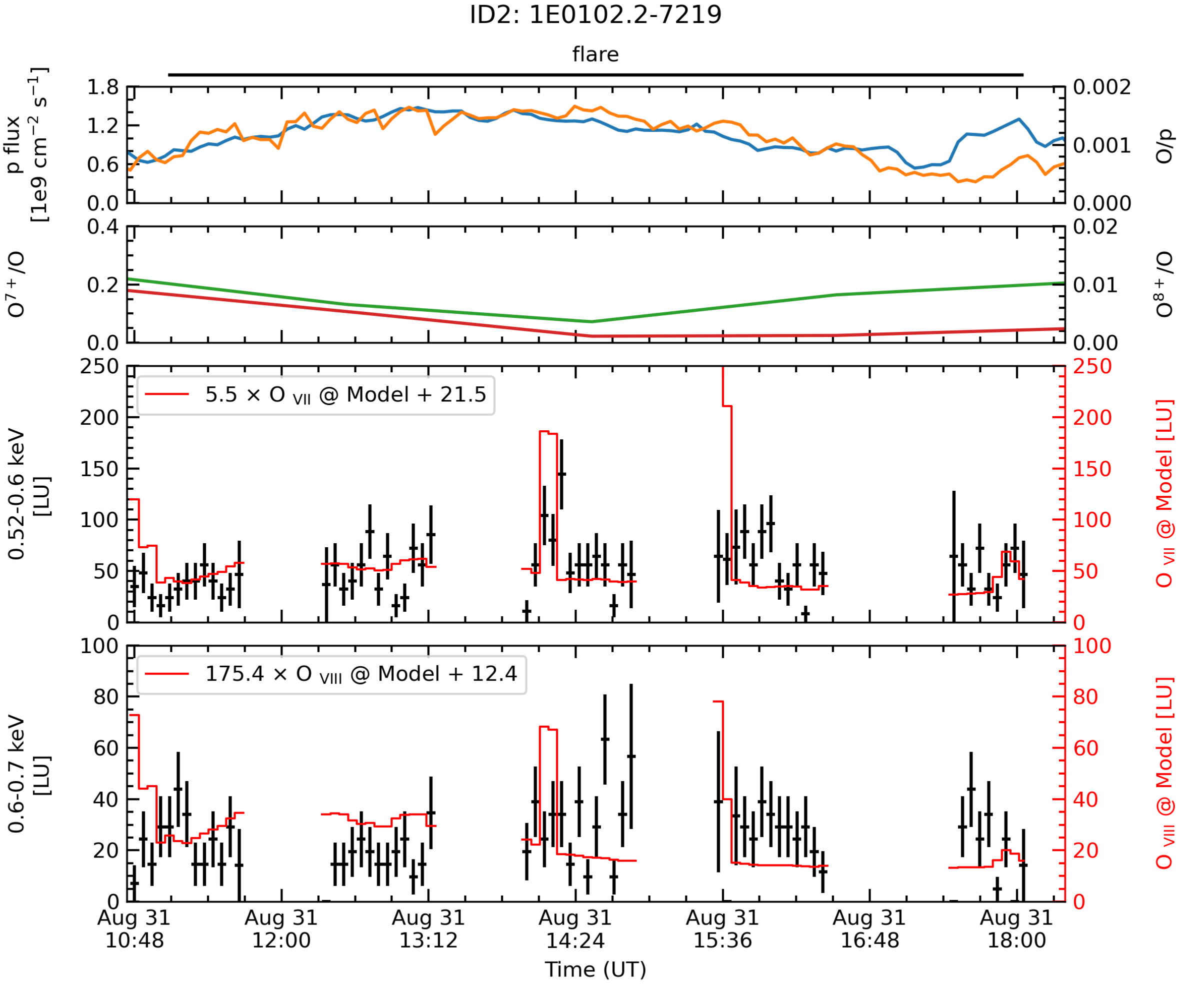

FIGURE 7.10: Enlarged view during the *flare* period of Figure 7.5. The time bin is much shorter.

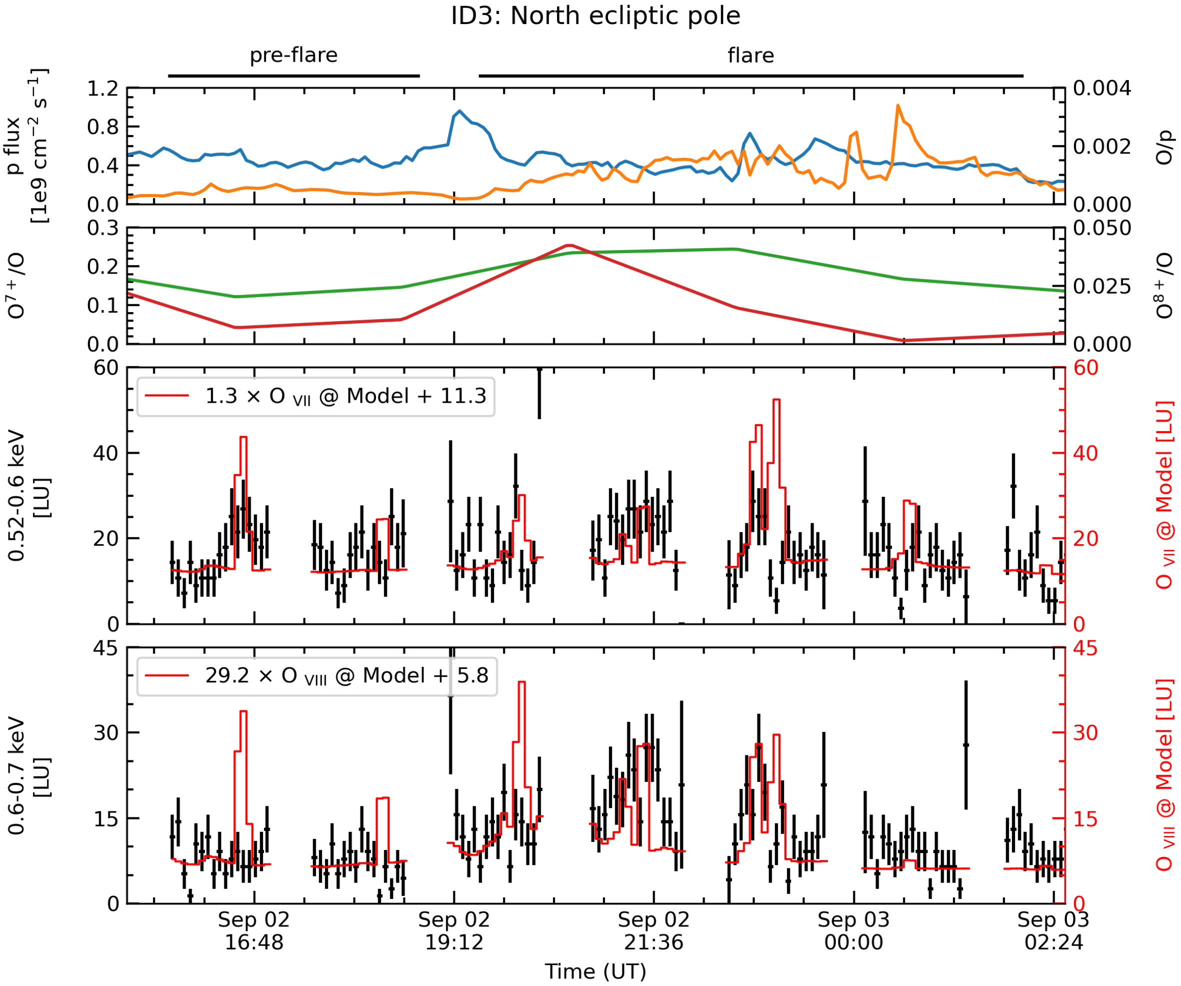

FIGURE 7.11: Enlarged view during the *pre-flare* and *flare* periods of Figure 7.6. The time bin is much shorter.

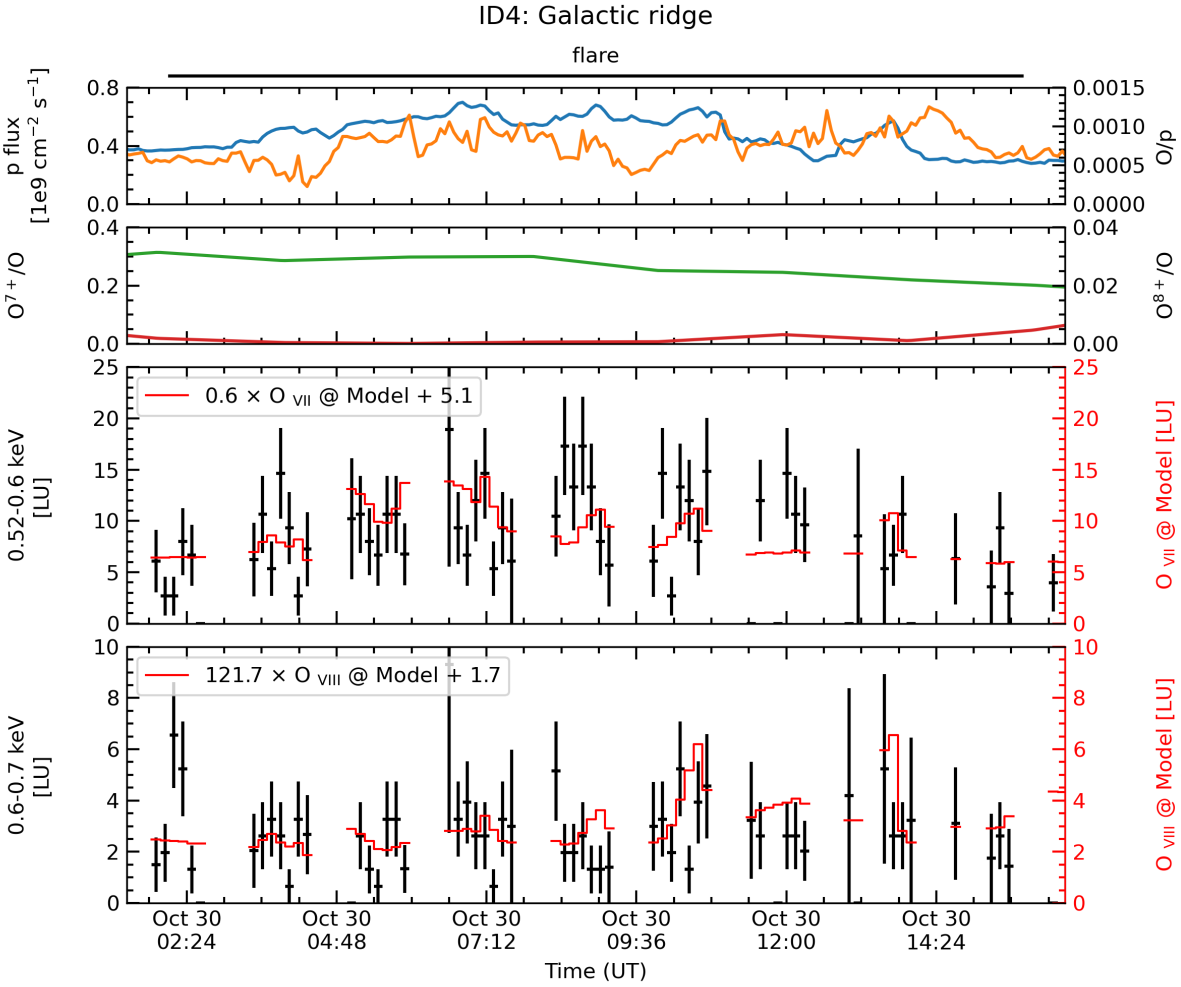

FIGURE 7.12: Enlarged view during the *flare* period of Figure 7.7. The time bin is much shorter.

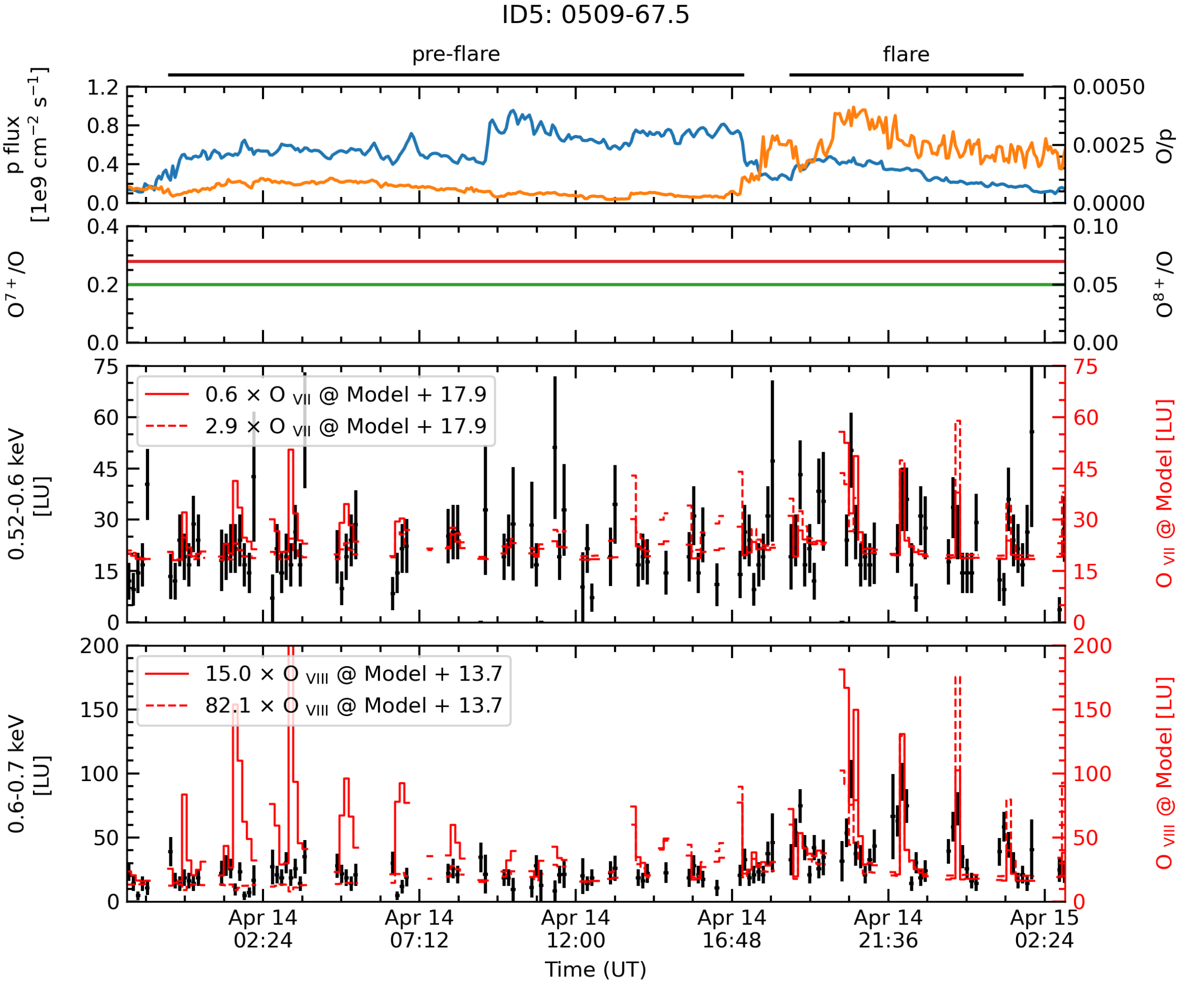

FIGURE 7.13: Enlarged view during the *pre-flare* and *flare* periods of Figure 7.8. The time bin is much shorter.

ratio has less variabilities during the entire observation. There are a lot of spike bins due to the line of sight direction passing through the northern polar cusp.

- ID4: The O VII light curve varies due to increased solar wind proton flux and oxygen to proton ratio. The O^{7+}/O ratio increased but the O^{8+}/O decreased during the *flare* period. There are no spike bins because the line-of-sight direction was toward the flanks of the magnetosheath.
- ID5: The O VII and O VIII light curves vary due to increased solar wind proton flux and oxygen to proton ratio. The oxygen ion fractions have some contributions to the observed temporal variations during the *pre-flare* and *flare* periods. There are a lot of spike bins due to the line of sight direction passing through the southern polar cusp.

7.3 Model validation

Below we validate our modeling procedures.

7.3.1 Comparison with MHD model

To check a possible effect due to our simplified magnetosheath model, we tested an MHD model for the observation of ID4. Most MHD simulations have some difficulties handling the near-cusp region, e.g., within 3 R_E. This observation whose line-of-sight direction was toward the flanks of the magnetosheath is a good example to verify our model. We adopted Block-Adaptive-Tree Solar Wind Roe-Type Upwind Scheme (Tóth et al., 2005; Tóth et al., 2012), available via the Community Coordinated Modeling Center facility through their public Runs on Request system, and downloaded an output file that had been run for other projects relevant to our Suzaku observation whose run name is "David_Sibeck_123011_1." This output covers from 12:00 UT on 2005 October 29 to 12:00 UT on 2005 October 30, corresponding roughly to the last half of the *stable* period and the first half of the *flare* period. The O VII line fluxes during the above periods were estimated to be 0.50 and 4.14 LU. These values are $\sim$1.4 and $\sim$2 times smaller than those obtained from our model during the corresponding periods, i.e., 0.72 and 8.10 LU, respectively. The O VIII line fluxes were 0.027 and 0.008 LU, which are $\sim$1.2 and $\sim$1.6 times smaller than our model values, i.e., 0.031 and 0.012 LU, respectively. The O VII line flux becomes more consistent with the observed value, while the O VIII line flux remains more underestimated.

7.3.2 Estimation of oxygen ion fluxes

To estimate more accurate solar wind ion fluxes for the observation of ID5, we tested an empirical equation of Kaaret et al. (2020). This equation is based on the analysis of the stacked data before the anomalies of ACE/SWICS. The O^{7+} and O^{8+} ion fluxes can be deduced from the O^{7+}/O^{6+} ratio. The O VII line fluxes during the *stable*, *pre-flare*, and *flare* periods were estimated to be 0.60, 1.60, and 2.87 LU, respectively. These values are $\sim$3, $\sim$7, and $\sim$5 times smaller than our model values. Those during the *pre-flare* and *flare* periods subtracted by that during the *stable* period were 1.00 and 2.28 LU, respectively, which agree with the observed values within a factor of $\sim$6 and $\sim$3. These differences become more significant than those obtained from our model. The O VIII line fluxes during the *stable*, *pre-flare*, and *flare* periods were 0.010, 0.080, and 0.429 LU, respectively, which are $\sim$35, $\sim$36, and $\sim$6 times smaller than our model values. Those during the *pre-flare* and *flare* periods subtracted by that during the *stable* period were 0.070 and 0.419 LU, respectively, which are $\sim$83 and $\sim$82 times smaller than the observed values. There remain more significant differences compared with our model results.

7.3.3 Contribution from heliospheric SWCX emission

The remaining concern is a potential contribution from heliospheric SWCX emission. The line-of-sight direction of Suzaku becomes parallel to the local Parker spiral, i.e., the orientation of the phase front near the Earth, and has a long pass length of ∼1 AU, thereby producing potentially significant heliospheric SWCX contributions with time scales similar to geocoronal SWCX emission. Kuntz et al. (2015) and Kuntz (2018) provided maps of temporal variabilities from heliospheric SWCX emission and their correlations with local solar wind fluxes near equator regions. The line-of-sight directions of ID1 and 4 were toward the near-equator region whose temporal variability and correlation are relatively high but not strong. Using the Parker spiral equations (Parker, 1958), we estimated the pass length of ID1 and 4 to be ∼0.4 and ∼0.2 AU, respectively. The line-of-sight directions of ID2, 3, and 5 were toward the near-polar region whose path length is ∼0.4 AU. The O_{VII} and O_{VIII} line fluxes were estimated to be 1.09 and 0.60 LU, respectively, assuming slow solar wind parameters and cross sections for hydrogen and helium atoms (Koutroumpa et al., 2006 and references therein), atomic hydrogen and helium densities of 0.001 and 0.005 cm^{-3} near the Earth (e.g., Cravens et al., 2001), and a path length of 0.2 AU. Those were 0.19 and 0.00 LU for fast solar wind values. The local Parker spiral contributions for O_{VII} and O_{VIII} emission lines were estimated to be 0.90 and 0.60 LU, respectively, considering the difference between uniformly high and low emissivities originating from slow and fast solar winds. The O_{VII} line flux is ∼4–46 times smaller than the observed values during the observations of ID1–5, while the O_{VIII} line flux is ∼0.7–57 times smaller. Although an accurate estimate of the local Parker spiral contribution needs more accurate solar wind propagations and interstellar neutral distributions, the bright SWCX events we analyzed are dominated mainly by geocoronal SWCX emission.

7.4 Future prospects

We need more data to calibrate our model and to reduce uncertainties problematic for astronomical observations. Our geocoronal SWCX database (e.g., Ishi et al., 2017) will be used for further validation in combination with an MHD model developed by Matsumoto and Miyoshi (2022). Future high-resolution and high-sensitivity X-ray spectroscopy missions such as XRISM and Athena will provide us with more SWCX events and more detailed information such as solar wind compositions, kinematics, and charge exchange processes as demonstrated in the X-ray micro-calorimeter instrument onboard Hitomi (e.g, Ezoe et al., 2021). On the other hand, geocoronal SWCX emission is suggested to be used to X-ray imaging of the Earth's magnetosphere as planned in future missions such as SMILE and GEO-X.

Chapter 8

Conclusion

In this thesis, we have built an empirical model to predict time-variable geocoronal SWCX emission and have examined the model in the five Suzaku observations of the bright geocoronal SWCX events. We re-analyzed the Suzaku data so that line intensities of geocoronal SWCX emission are accurately extracted in the same manner. For model comparison, we focused on the strong O $_{\rm VII}$ and O $_{\rm VIII}$ emission lines seen in the 0.5–0.7 keV band.

In the modeling, we took into account time-variable solar wind ion fluxes and abundances using the WIND and ACE data. To describe exospheric neutral hydrogen distributions, we adopted a simple formula built by Cravens et al. (2001). Charge exchange cross sections were taken from values shown in Bodewits et al. (2007), which are based on ground experiments and theoretical predictions. The magnetopause and bow shock positions were determined from the empirical models of Shue et al. (1998) and Merka et al. (2005), respectively. To consider the line-of-sight direction passing through the near-cusp region during the orbital motion of Suzaku, we traced the magnetic field lines along the observer's line of sight using the magnetic field model of Tsyganenko and Sitnov (2005). The decelerated and heated solar wind plasma downstream of the bow shock was represented by the Rankine–Hugoniot equations.

Using the model, we estimated the O $_{\rm VII}$ line flux and found that the model agreed with the data except for one case in which the line-of-sight direction was toward the night side of the high-latitude magnetosheath and the major geomagnetic storm was observed. The solar wind injection into the inner magnetosphere may contribute to geocoronal SWCX emission. The O VIII line flux was not consistent with the data in all the five cases. These discrepancies can not be explained even considering possible model uncertainties. This suggests that further uncertainties exist in the solar wind ion data concerning highly stripped ion states. We simulated geocoronal SWCX light curves and found that the modeled light curves after scaling are consistent with the data including some spike behaviors due to the line-of-sight direction passing through the near-cusp regions associated with the low-Earth orbit.

Although more SWCX events are needed to examine such tendencies, this model can provide a new estimation of geocoronal SWCX emission including light curves for future X-ray astronomy missions as well as X-ray imaging missions of the Earth's magnetosphere.

Bibliography

[1] K. Asakura, H. Matsumoto, K. Okazaki, T. Yoneyama, H. Noda, K. Hayashida, H. Tsunemi, H. Nakajima, S. Katsuda, D. Ishi, and Y. Ezoe, “Suzaku detection of solar wind charge exchange emission from a variety of highly ionized ions in an interplanetary coronal mass ejection”, Publications of the Astronomical Society of Japan **73**, 504–518 (2021).

[2] J. Bailey and M. Gruntman, “Experimental study of exospheric hydrogen atom distributions by Lyman-alpha detectors on the TWINS mission”, Journal of Geophysical Research: Space Physics **116**, A09302 (2011).

[3] J. Bailey and M. Gruntman, “Observations of exosphere variations during geomagnetic storms”, Geophysical Research Letters **40**, 1907–1911 (2013).

[4] I. I. Baliukin, J.-L. Bertaux, E. Quémerais, V. V. Izmodenov, and W. Schmidt, “SWAN/SOHO Lyman-α Mapping: The Hydrogen Geocorona Extends Well Beyond the Moon”, Journal of Geophysical Research: Space Physics **124**, 861–885 (2019).

[5] P. Beiersdorfer, K. R. Boyce, G. V. Brown, H. Chen, S. M. Kahn, R. L. Kelley, M. May, R. E. Olson, F. S. Porter, C. K. Stahle, and W. A. Tillotson, “Laboratory Simulation of Charge Exchange-Produced X-ray Emission from Comets”, Science **300**, 1558–1559 (2003).

[6] L. Biermann, “Kometenschweife und solare Korpuskularstrahlung”, Zeitschrift für Astrophysik **29**, 274 (1951).

[7] D. Bodewits, D. J. Christian, M. Torney, M. Dryer, C. M. Lisse, K. Dennerl, T. H. Zurbuchen, S. J. Wolk, A. G. G. M. Tielens, and R. Hoekstra, "Spectral analysis of the Chandra comet survey", A&A **469**, 1183–1195 (2007).

[8] G. Branduardi-Raymont, A. Bhardwaj, R. F. Elsner, G. R. Gladstone, G. Ramsay, P. Rodriguez, R. Soria, J. H. Waite, Jr, and T. E. Cravens, "A study of Jupiter's aurorae with XMM-Newton", A&A **463**, 761–774 (2007).

[9] G. Branduardi-Raymont, R. F. Elsner, G. R. Gladstone, G. Ramsay, P. Rodriguez, R. Soria, and J. H. Waite, "First observation of Jupiter by XMM-Newton", A&A **424**, 331–337 (2004).

[10] J. A. Carter and S. Sembay, "Identifying XMM-Newton observations affected by solar wind charge exchange. Part I", A&A **489**, 837–848 (2008).

[11] J. A. Carter, S. Sembay, and A. M. Read, "A high charge state coronal mass ejection seen through solar wind charge exchange emission as detected by XMM–Newton", Monthly Notices of the Royal Astronomical Society **402**, 867–878 (2010).

[12] J. A. Carter, S. Sembay, and A. M. Read, "Identifying XMM-Newton observations affected by solar wind charge exchange - Part II", A&A **527**, A115 (2011).

[13] J. W. Chamberlain, "Planetary coronae and atmospheric evaporation", Planetary and Space Science **11**, 901–960 (1963).

[14] M. R. Collier, S. L. Snowden, M. Sarantos, M. Benna, J. A. Carter, T. E. Cravens, W. M. Farrell, S. Fatemi, H. K. Hills, R. R. Hodges, M. Holmström, K. D. Kuntz, F. S. Porter, A. Read, I. P. Robertson, S. F. Sembay, D. G. Sibeck, T. J. Stubbs, P. Travnicek, and B. M. Walsh, "On lunar exospheric column densities and solar wind access beyond the terminator from ROSAT soft X-ray observations of solar wind charge exchange", Journal of Geophysical Research: Planets **119**, 1459–1478 (2014).

[15] H. K. Connor and J. A. Carter, "Exospheric Neutral Hydrogen Density at the Nominal 10 R_E Subsolar Point Deduced From XMM-Newton X-Ray Observations", Journal of Geophysical Research: Space Physics **124**, 1612–1624 (2019).

[16] D. P. Cox, "Modeling the local bubble", The Local Bubble and Beyond Lyman-Spitzer-Colloquium, Vol. 506, edited by D. Breitschwerdt, M. Freyberg, and J. Trümper (1998), pp. 121–131.

[17] T. E. Cravens, "Comet Hyakutake x-ray source: Charge transfer of solar wind heavy ions", Geophysical Research Letters **24**, 105–108 (1997).

[18] T. E. Cravens, I. P. Robertson, and S. L. Snowden, "Temporal variations of geocoronal and heliospheric X-ray emission associated with the solar wind interaction with neutrals", Journal of Geophysical Research: Space Physics **106**, 24883–24892 (2001).

[19] T. E. Cravens, "Heliospheric X-ray Emission Associated with Charge Transfer of the Solar Wind with Interstellar Neutrals", The Astrophysical Journal **532**, L153–L156 (2000).

[20] K. Dennerl, "Discovery of X-rays from Mars with Chandra", A&A **394**, 1119–1128 (2002).

[21] K. Dennerl, V. Burwitz, J. Englhauser, C. Lisse, and S. Wolk, "Discovery of X-rays from Venus with Chandra", A&A **386**, 319–330 (2002).

[22] K. Dennerl, C. M. Lisse, A. Bhardwaj, V. Burwitz, J. Englhauser, H. Gunell, M. Holmström, F. Jansen, V. Kharchenko, and P. M. Rodríguez-Pascual, "First observation of Mars with XMM-Newton - High resolution X-ray spectroscopy with RGS", A&A **451**, 709–722 (2006).

[23] K. Dennerl, "X-rays from Venus observed with Chandra", Planetary and Space Science **56**, 1414–1423 (2008).

[24] Y. Ebihara, S. Kasahara, K. Seki, Y. Miyoshi, T. A. Fritz, J. Chen, M. Grande, and T. H. Zurbuchen, "Simultaneous entry of oxygen ions originating from the Sun and Earth into the inner magnetosphere during magnetic storms", Journal of Geophysical Research: Space Physics **114**, A05219 (2009).

[25] K. Ebisawa, S. Yamauchi, Y. Tanaka, K. Koyama, Y. Ezoe, A. Bamba, M. Kokubun, Y. Hyodo, M. Tsujimoto, and H. Takahashi, "Spectral Study of the Galactic Ridge X-Ray Emission with Suzaku", Publications of the Astronomical Society of Japan **60**, S223–S229 (2008).

[26] Y. Ezoe, K. Ishikawa, T. Ohashi, Y. Miyoshi, N. Terada, Y. Uchiyama, and H. Negoro, "DISCOVERY OF DIFFUSE HARD X-RAY EMISSION AROUND JUPITER WITH SUZAKU", The Astrophysical Journal **709**, L178–L182 (2010).

[27] Y. Ezoe, K. Ebisawa, N. Y. Yamasaki, K. Mitsuda, H. Yoshitake, N. Terada, Y. Miyoshi, and R. Fujimoto, "Time Variability of the Geocoronal Solar-Wind Charge Exchange in the Direction of the Celestial Equator", Publications of the Astronomical Society of Japan **62**, 981–986 (2010).

[28] Y. Ezoe, Y. Miyoshi, H. Yoshitake, K. Mitsuda, N. Terada, S. Oishi, and T. Ohashi, "Enhancement of Terrestrial Diffuse X-Ray Emission Associated with Coronal Mass Ejection and Geomagnetic Storm", Publications of the Astronomical Society of Japan **63**, S691–S704 (2011).

[29] Y. Ezoe, T. Ohashi, and K. Mitsuda, "High-resolution X-ray spectroscopy of astrophysical plasmas with X-ray microcalorimeters", Reviews of Modern Plasma Physics **5**, 4 (2021).

[30] M. J. Freyberg, "On the zero-level of the soft X-ray background", The Local Bubble and Beyond Lyman-Spitzer-Colloquium, Vol. 506, edited by D. Breitschwerdt, M. Freyberg, and J. Trümper (1998), pp. 113–116.

[31] R. Fujimoto, K. Mitsuda, D. McCammon, Y. Takei, M. Bauer, Y. Ishisaki, F. S. Porter, H. Yamaguchi, K. Hayashida, and N. Y. Yamasaki, "Evidence for Solar-Wind Charge-Exchange X-Ray Emission from the Earth's Magnetosheath", Publications of the Astronomical Society of Japan **59**, S133–S140 (2007).

[32] S. A. Fuselier, M. A. Dayeh, A. Galli, H. O. Funsten, N. A. Schwadron, S. M. Petrinec, K. J. Trattner, D. J. McComas, J. L. Burch, S. Toledo-Redondo, J. R. Szalay, and R. J. Strangeway, "Neutral Atom Imaging of the Solar Wind-Magnetosphere-Exosphere Interaction Near the Subsolar Magnetopause", Geophysical Research Letters **47**, e2020GL089362 (2020).

[33] S. A. Fuselier, H. O. Funsten, D. Heirtzler, P. Janzen, H. Kucharek, D. J. McComas, E. Möbius, T. E. Moore, S. M. Petrinec, D. B. Reisenfeld, N. A. Schwadron, K. J. Trattner, and P. Wurz, "Energetic neutral atoms from the Earth's subsolar magnetopause", Geophysical Research Letters **37**, L13101 (2010).

[34] G. R. Gladstone, J. H. Waite, D. Grodent, W. S. Lewis, F. J. Crary, R. F. Elsner, M. C. Weisskopf, T. Majeed, J.-M. Jahn, A. Bhardwaj, J. T. Clarke, D. T. Young, M. K. Dougherty, S. A. Espinosa, and T. E. Cravens, "A pulsating auroral X-ray hot spot on Jupiter", Nature **415**, 1000–1003 (2002).

[35] G. Gloeckler, J. Cain, F. M. Ipavich, E. O. Tums, P. Bedini, L. A. Fisk, T. H. Zurbuchen, P. Bochsler, J. Fischer, R. F. Wimmer-Schweingruber, J. Geiss, and R. Kallenbach, "Investigation of the composition of solar and interstellar matter using solar wind and pickup ion measurements with SWICS and SWIMS on the ACE spacecraft", Space Science Reviews **86**, 497–539 (1998).

[36] A. A. Hasan, F. Eissa, R. Ali, D. R. Schultz, and P. C. Stancil, "State-selective Charge Transfer Studies Relevant to Solar Wind-Comet Interactions", The Astrophysical Journal **560**, L201 (2001).

[37] R. R. Hodges Jr., "Monte Carlo simulation of the terrestrial hydrogen exosphere", Journal of Geophysical Research: Space Physics **99**, 23229–23247 (1994).

[38] A. J. Hundhausen, H. E. Gilbert, and S. J. Bame, “Ionization state of the interplanetary plasma”, Journal of Geophysical Research **73**, 5485–5493 (1968).

[39] D. Ishi, K. Ishikawa, Y. Ezoe, T. Ohashi, Y. Miyoshi, and N. Terada, “A Systematic Search for Solar Wind Charge Exchange Emission from the Earth’s Exosphere with Suzaku”, The X-ray Universe 2017, edited by J.-U. Ness and S. Migliari (2017), p. 103.

[40] D. Ishi, K. Ishikawa, M. Numazawa, Y. Miyoshi, N. Terada, K. Mitsuda, T. Ohashi, and Y. Ezoe, “Suzaku detection of enigmatic geocoronal solar wind charge exchange event associated with coronal mass ejection”, Publications of the Astronomical Society of Japan **71**, 23 (2019).

[41] K. Ishikawa, Y. Ezoe, Y. Miyoshi, N. Terada, K. Mitsuda, and T. Ohashi, “Suzaku Observation of Strong Solar-Wind Charge-Exchange Emission from the Terrestrial Exosphere during a Geomagnetic Storm”, Publications of the Astronomical Society of Japan **65**, 63 (2013).

[42] K. Ishikawa, Y. Ezoe, T. Ohashi, N. Terada, and Y. Futaana, “X-Ray Observation of Mars at Solar Minimum with Suzaku”, Publications of the Astronomical Society of Japan **63**, S705–S712 (2011).

[43] J. Jung, H. K. Connor, J. A. Carter, D. Koutroumpa, C. Pagani, and K. D. Kuntz, “Solar Minimum Exospheric Neutral Density Near the Subsolar Magnetopause Estimated From the XMM Soft X-Ray Observations on 12 November 2008”, Journal of Geophysical Research: Space Physics **127**, e2021JA029676 (2022).

[44] P. Kaaret, D. Koutroumpa, K. D. Kuntz, K. Jahoda, J. Bluem, H. Gulick, E. Hodges-Kluck, D. M. LaRocca, R. Ringuette, and A. Zajczyk, “A disk-dominated and clumpy circumgalactic medium of the Milky Way seen in X-ray emission”, Nature Astronomy **4**, 1072–1077 (2020).

[45] S. Kameda, S. Ikezawa, M. Sato, M. Kuwabara, N. Osada, G. Murakami, K. Yoshioka, I. Yoshikawa, M. Taguchi, R. Funase, S. Sugita, Y. Miyoshi, and M. Fujimoto, "Ecliptic North-South Symmetry of Hydrogen Geocorona", Geophysical Research Letters **44**, 11706–11712 (2017).

[46] S. Kanekal and Y. Miyoshi, "Dynamics of the terrestrial radiation belts: a review of recent results during the VarSITI (Variability of the Sun and Its Terrestrial Impact) era, 2014–2018", Progress in Earth and Planetary Science **8**, 35 (2021).

[47] R. L. Kelley, K. Mitsuda, C. A. Allen, P. Arsenovic, M. D. Audley, T. G. Bialas, K. R. Boyce, R. F. Boyle, S. R. Breon, G. V. Brown, J. Cottam, M. J. DiPirro, R. Fujimoto, T. Furusho, K. C. Gendreau, G. G. Gochar, O. Gonzalez, M. Hirabayashi, S. S. Holt, H. Inoue, M. Ishida, Y. Ishisaki, C. S. Jones, R. Keski-Kuha, C. A. Kilbourne, D. McCammon, U. Morita, S. H. Moseley, B. Mott, K. Narasaki, Y. Ogawara, T. Ohashi, N. Ota, J. S. Panek, F. S. Porter, A. Serlemitsos, P. J. Shirron, G. A. Sneiderman, A. E. Szymkowiak, Y. Takei, J. L. Tveekrem, S. M. Volz, M. Yamamoto, and N. Y. Yamasaki, "The Suzaku High Resolution X-Ray Spectrometer", Publications of the Astronomical Society of Japan **59**, S77–S112 (2007).

[48] D. Koutroumpa, R. Lallement, V. Kharchenko, A. Dalgarno, R. Pepino, V. Izmodenov, and E. Quémerais, "Charge-transfer induced EUV and soft X-ray emissions in the heliosphere", A&A **460**, 289–300 (2006).

[49] K. Koyama, H. Tsunemi, T. Dotani, M. W. Bautz, K. Hayashida, T. G. Tsuru, H. Matsumoto, Y. Ogawara, G. R. Ricker, J. Doty, S. E. Kissel, R. Foster, H. Nakajima, H. Yamaguchi, H. Mori, M. Sakano, K. Hamaguchi, M. Nishiuchi, E. Miyata, K. Torii, M. Namiki, S. Katsuda, D. Matsuura, T. Miyauchi, N. Anabuki, N. Tawa, M. Ozaki, H. Murakami, Y. Maeda, Y. Ichikawa, G. Y. Prigozhin, E. A. Boughan, B. LaMarr, E. D. Miller, B. E. Burke, J. A. Gregory, A. Pillsbury, A. Bamba, J. S. Hiraga, A. Senda, H. Katayama, S. Kitamoto, M. Tsujimoto, T. Kohmura, Y. Tsuboi, and H. Awaki, "X-Ray Imaging Spectrometer (XIS) on Board Suzaku", Publications of the Astronomical Society of Japan **59**, S23–S33 (2007).

[50] V. A. Krasnopolsky, J. B. Greenwood, and P. C. Stancil, “X-ray and extreme ultraviolet emissions from comets”, Space Science Reviews **113**, 271–373 (2004).

[51] K. D. Kuntz, “Solar wind charge exchange: an astrophysical nuisance”, The Astronomy and Astrophysics Review **27**, 1 (2018).

[52] K. D. Kuntz, Y. M. Collado-Vega, M. R. Collier, H. K. Connor, T. E. Cravens, D. Koutroumpa, F. S. Porter, I. P. Robertson, D. G. Sibeck, S. L. Snowden, N. E. Thomas, and B. M. Walsh, “THE SOLAR WIND CHARGE-EXCHANGE PRODUCTION FACTOR FOR HYDROGEN”, The Astrophysical Journal **808**, 143 (2015).

[53] M. Kuwabara, K. Yoshioka, G. Murakami, F. Tsuchiya, T. Kimura, A. Yamazaki, and I. Yoshikawa, “The geocoronal responses to the geomagnetic disturbances”, Journal of Geophysical Research: Space Physics **122**, 1269–1276 (2017).

[54] C. M. Lisse, T. E. Cravens, and K. Dennerl, “X-ray and extreme ultraviolet emission from comets”, Comets II, edited by M. C. Festou, H. U. Keller, and H. A. Weaver (2004), p. 631.

[55] C. M. Lisse, K. Dennerl, J. Englhauser, M. Harden, F. E. Marshall, M. J. Mumma, R. Petre, J. P. Pye, M. J. Ricketts, J. Schmitt, J. Trümper, and R. G. West, “Discovery of X-ray and Extreme Ultraviolet Emission from Comet C/Hyakutake 1996 B2”, Science **274**, 205–209 (1996).

[56] Y. Matsumoto and Y. Miyoshi, “Soft X-Ray Imaging of Magnetopause Reconnection Outflows Under Low Plasma-β Solar Wind Conditions”, Geophysical Research Letters **49**, e2022GL101037 (2022).

[57] D. J. McComas, S. J. Bame, P. Barker, W. C. Feldman, J. L. Phillips, P. Riley, and J. W. Griffee, “Solar Wind Electron Proton Alpha Monitor (SWEPAM) for the Advanced Composition Explorer”, Space Science Reviews **86**, 563–612 (1998).

[58] J. Merka, A. Szabo, J. A. Slavin, and M. Peredo, "Three-dimensional position and shape of the bow shock and their variation with upstream Mach numbers and interplanetary magnetic field orientation", Journal of Geophysical Research: Space Physics **110**, A04202 (2005).

[59] K. Mitsuda, M. Bautz, H. Inoue, R. L. Kelley, K. Koyama, H. Kunieda, K. Makishima, Y. Ogawara, R. Petre, T. Takahashi, H. Tsunemi, N. E. White, N. Anabuki, L. Angelini, K. Arnaud, H. Awaki, A. Bamba, K. Boyce, G. V. Brown, K.-W. Chan, J. Cottam, T. Dotani, J. Doty, K. Ebisawa, Y. Ezoe, A. C. Fabian, E. Figueroa, R. Fujimoto, Y. Fukazawa, T. Furusho, A. Furuzawa, K. Gendreau, R. E. Griffiths, Y. Haba, K. Hamaguchi, I. Harrus, G. Hasinger, I. Hatsukade, K. Hayashida, P. J. Henry, J. S. Hiraga, S. S. Holt, A. Hornschemeier, J. P. Hughes, U. Hwang, M. Ishida, Y. Ishisaki, N. Isobe, M. Itoh, N. Iyomoto, S. M. Kahn, T. Kamae, H. Katagiri, J. Kataoka, H. Katayama, N. Kawai, C. Kilbourne, K. Kinugasa, S. Kissel, S. Kitamoto, M. Kohama, T. Kohmura, M. Kokubun, T. Kotani, J. Kotoku, A. Kubota, G. M. Madejski, Y. Maeda, F. Makino, A. Markowitz, C. Matsumoto, H. Matsumoto, M. Matsuoka, K. Matsushita, D. McCammon, T. Mihara, K. Misaki, E. Miyata, T. Mizuno, K. Mori, H. Mori, M. Morii, H. Moseley, K. Mukai, H. Murakami, T. Murakami, R. Mushotzky, F. Nagase, M. Namiki, H. Negoro, K. Nakazawa, J. A. Nousek, T. Okajima, Y. Ogasaka, T. Ohashi, T. Oshima, N. Ota, M. Ozaki, H. Ozawa, A. N. Parmar, W. D. Pence, F. S. Porter, J. N. Reeves, G. R. Ricker, I. Sakurai, W. T. Sanders, A. Senda, P. Serlemitsos, R. Shibata, Y. Soong, R. Smith, M. Suzuki, A. E. Szymkowiak, H. Takahashi, T. Tamagawa, K. Tamura, T. Tamura, Y. Tanaka, M. Tashiro, Y. Tawara, Y. Terada, Y. Terashima, H. Tomida, K. Torii, Y. Tsuboi, M. Tsujimoto, T. G. Tsuru, M. J. L. Turner, Y. Ueda, S. Ueno, M. Ueno, S. Uno, Y. Urata, S. Watanabe, N. Yamamoto, K. Yamaoka, N. Y. Yamasaki, K. Yamashita, M. Yamauchi, S. Yamauchi, T. Yaqoob, D. Yonetoku, and A. Yoshida, "The X-Ray Observatory Suzaku", Publications of the Astronomical Society of Japan **59**, S1–S7 (2007).

[60] P. D. Mullen, R. S. Cumbee, D. Lyons, L. Gu, J. Kaastra, R. L. Shelton, and P. C. Stancil, "Line Ratios for Solar Wind Charge Exchange with Comets", The Astrophysical Journal **844**, 7 (2017).

[61] M. Numazawa, Y. Ezoe, K. Ishikawa, T. Ohashi, Y. Miyoshi, T. Kimura, Y. Uchiyama, D. Shiota, and G. Branduardi-Raymont, "Suzaku observation of Jupiter's X-rays around solar maximum", Publications of the Astronomical Society of Japan **71**, 93 (2019).

[62] M. Numazawa, Y. Ezoe, T. Ohashi, K. Ishikawa, Y. Miyoshi, D. Shiota, Y. Uchiyama, T. Kimura, and G. Branduardi-Raymont, "Suzaku observations of Jovian diffuse hard X-ray emission", Publications of the Astronomical Society of Japan **73**, 894–911 (2021).

[63] K. W. Ogilvie, D. J. Chornay, R. J. Fritzenreiter, F. Hunsaker, J. Keller, J. Lobell, G. Miller, J. D. Scudder, E. C. Sittler, R. B. Torbert, D. Bodet, G. Needell, A. J. Lazarus, J. T. Steinberg, J. H. Tappan, A. Mavretic, and E. Gergin, "SWE, a comprehensive plasma instrument for the WIND spacecraft", Space Science Reviews **71**, 55–77 (1995).

[64] N. Østgaard, S. B. Mende, H. U. Frey, G. R. Gladstone, and H. Lauche, "Neutral hydrogen density profiles derived from geocoronal imaging", Journal of Geophysical Research: Space Physics **108**, 1300 (2003).

[65] S. Otranto, R. E. Olson, and P. Beiersdorfer, "X-ray emission cross sections following charge exchange by multiply charged ions of astrophysical interest", Phys. Rev. A **73**, 022723 (2006).

[66] E. N. Parker, "Dynamics of the Interplanetary Gas and Magnetic Fields.", The Astrophysical Journal **128**, 664 (1958).

[67] P. P. Plucinsky, S. L. Snowden, U. G. Briel, G. Hasinger, and E. Pfeffermann, "An Updated Calibration of the ROSAT PSPC Particle Background for the Analysis of Diffuse and Extended Sources", The Astrophysical Journal **418**, 519 (1993).

[68] I. G. Richardson and H. V. Cane, "Identification of interplanetary coronal mass ejections at 1 AU using multiple solar wind plasma composition anomalies", Journal of Geophysical Research: Space Physics **109**, A09104 (2004).

[69] I. P. Robertson, M. R. Collier, T. E. Cravens, and M.-C. Fok, "X-ray emission from the terrestrial magnetosheath including the cusps", Journal of Geophysical Research: Space Physics **111**, A12105 (2006).

[70] I. P. Robertson, S. Sembay, T. J. Stubbs, K. D. Kuntz, M. R. Collier, T. E. Cravens, S. L. Snowden, H. K. Hills, F. S. Porter, P. Travnicek, J. A. Carter, and A. M. Read, "Solar wind charge exchange observed through the lunar exosphere", Geophysical Research Letters **36**, L21102 (2009).

[71] H. Ryufuku and T. Watanabe, "Total and partial cross sections for charge transfer in collisions of multicharged ions with atomic hydrogen", Phys. Rev. A **20**, 1828–1837 (1979).

[72] J. H. M. M. Schmitt, S. L. Snowden, B. Aschenbach, G. Hasinger, E. Pfeffermann, P. Predehl, and J. Trümper, "A soft X-ray image of the Moon", Nature **349**, 583–587 (1991).

[73] N. A. Schwadron and T. E. Cravens, "Implications of Solar Wind Composition for Cometary X-Rays", The Astrophysical Journal **544**, 558–566 (2000).

[74] N. Sekiya, N. Y. Yamasaki, K. Mitsuda, and Y. Takei, "O I fluorescent line contamination in soft X-ray diffuse background obtained with Suzaku/XIS", Publications of the Astronomical Society of Japan **66**, L3 (2014).

[75] P. J. Serlemitsos, Y. Soong, K.-W. Chan, T. Okajima, J. P. Lehan, Y. Maeda, K. Itoh, H. Mori, R. Iizuka, A. Itoh, H. Inoue, S. Okada, Y. Yokoyama, Y. Itoh, M. Ebara, R. Nakamura, K. Suzuki, M. Ishida, A. Hayakawa, C. Inoue, S. Okuma, R. Kubota, M. Suzuki, T. Osawa, K. Yamashita, H. Kunieda, Y. Tawara, Y. Ogasaka, A. Furuzawa, K. Tamura, R. Shibata, Y. Haba, M. Naitou, and K. Misaki, "The X-Ray Telescope onboard Suzaku", Publications of the Astronomical Society of Japan **59**, S9–S21 (2007).

[76] J.-H. Shue, P. Song, C. T. Russell, J. T. Steinberg, J. K. Chao, G. Zastenker, O. L. Vaisberg, S. Kokubun, H. J. Singer, T. R. Detman, and H. Kawano, "Magnetopause location under extreme solar wind conditions", Journal of Geophysical Research: Space Physics **103**, 17691–17700 (1998).

[77] D. G. Sibeck, M. R. Collier, and M. V. D. Silveira, "Neutral Densities in the Outer Exosphere Near the Subsolar Magnetopause", Geophysical Research Letters **48**, e2021GL093383 (2021).

[78] S. L. Snowden, M. R. Collier, T. Cravens, K. D. Kuntz, S. T. Lepri, I. Robertson, and L. Tomas, "OBSERVATION OF SOLAR WIND CHARGE EXCHANGE EMISSION FROM EXOSPHERIC MATERIAL IN AND OUTSIDE EARTH'S MAGNETOSHEATH 2008 SEPTEMBER 25", The Astrophysical Journal **691**, 372–381 (2009).

[79] S. L. Snowden, M. R. Collier, and K. D. Kuntz, "XMM-Newton Observation of Solar Wind Charge Exchange Emission", The Astrophysical Journal **610**, 1182–1190 (2004).

[80] S. L. Snowden, R. Egger, M. J. Freyberg, D. McCammon, P. P. Plucinsky, W. T. Sanders, J. H. M. M. Schmitt, J. Trumper, and W. Voges, "ROSAT Survey Diffuse X-Ray Background Maps. II.", The Astrophysical Journal **485**, 125–135 (1997).

[81] S. L. Snowden and M. J. Freyberg, "The Scattered Solar X-Ray Background of the ROSAT PSPC", The Astrophysical Journal **404**, 403 (1993).

[82] S. L. Snowden, D. McCammon, D. N. Burrows, and J. A. Mendenhall, "Analysis Procedures for ROSAT XRT/PSPC Observations of Extended Objects and the Diffuse Background", The Astrophysical Journal **424**, 714 (1994).

[83] S. L. Snowden, P. P. Plucinsky, U. Briel, G. Hasinger, and E. Pfeffermann, "The Particle Background of the ROSAT PSPC", The Astrophysical Journal **393**, 819 (1992).

[84] J. R. Spreiter, A. L. Summers, and A. Y. Alksne, "Hydromagnetic flow around the magnetosphere", Planetary and Space Science **14**, 223–253 (1966).

[85] T. Takahashi, K. Abe, M. Endo, Y. Endo, Y. Ezoe, Y. Fukazawa, M. Hamaya, S. Hirakuri, S. Hong, M. Horii, H. Inoue, N. Isobe, T. Itoh, N. Iyomoto, T. Kamae, D. Kasama, J. Kataoka, H. Kato, M. Kawaharada, N. Kawano, K. Kawashima, S. Kawasoe, T. Kishishita, T. Kitaguchi, Y. Kobayashi, M. Kokubun, J. Kotoku, M. Kouda, A. Kubota, Y. Kuroda, G. Madejski, K. Makishima, K. Masukawa, Y. Matsumoto, T. Mitani, R. Miyawaki, T. Mizuno, K. Mori, M. Mori, M. Murashima, T. Murakami, K. Nakazawa, H. Niko, M. Nomachi, Y. Okada, M. Ohno, K. Oonuki, N. Ota, H. Ozawa, G. Sato, S. Shinoda, M. Sugiho, M. Suzuki, K. Taguchi, H. Takahashi, I. Takahashi, S. Takeda, K.-i. Tamura, T. Tamura, T. Tanaka, C. Tanihata, M. Tashiro, Y. Terada, S. Tominaga, Y. Uchiyama, S. Watanabe, K. Yamaoka, T. Yanagida, and D. Yonetoku, "Hard X-Ray Detector (HXD) on Board Suzaku", Publications of the Astronomical Society of Japan **59**, S35–S51 (2007).

[86] N. Tawa, K. Hayashida, M. Nagai, H. Nakamoto, H. Tsunemi, H. Yamaguchi, Y. Ishisaki, E. D. Miller, T. Mizuno, T. Dotani, M. Ozaki, and H. Katayama, "Reproducibility of Non-X-Ray Background for the X-Ray Imaging Spectrometer aboard Suzaku", Publications of the Astronomical Society of Japan **60**, S11–S24 (2008).

[87] G. Tóth, I. V. Sokolov, T. I. Gombosi, D. R. Chesney, C. R. Clauer, D. L. De Zeeuw, K. C. Hansen, K. J. Kane, W. B. Manchester, R. C. Oehmke, K. G. Powell, A. J. Ridley, I. I. Roussev, Q. F. Stout, O. Volberg, R. A. Wolf, S. Sazykin, A. Chan, B. Yu, and J. Kóta, "Space Weather Modeling Framework: A new tool for the space science community", Journal of Geophysical Research: Space Physics **110**, A12226 (2005).

[88] G. Tóth, B. van der Holst, I. V. Sokolov, D. L. De Zeeuw, T. I. Gombosi, F. Fang, W. B. Manchester, X. Meng, D. Najib, K. G. Powell, Q. F. Stout, A. Glocer, Y.-J.

Ma, and M. Opher, “Adaptive numerical algorithms in space weather modeling”, Journal of Computational Physics **231**, 870–903 (2012).

[89] T. L. Totten, J. W. Freeman, and S. Arya, “An empirical determination of the polytropic index for the free-streaming solar wind using Helios 1 data”, Journal of Geophysical Research: Space Physics **100**, 13–17 (1995).

[90] N. A. Tsyganenko and M. I. Sitnov, “Modeling the dynamics of the inner magnetosphere during strong geomagnetic storms”, Journal of Geophysical Research: Space Physics **110**, A03208 (2005).

[91] B. M. Walsh, K. D. Kuntz, M. R. Collier, D. G. Sibeck, S. L. Snowden, and N. E. Thomas, “Energetic particle impact on X-ray imaging with XMM-Newton”, Space Weather **12**, 387–394 (2014).

[92] B. M. Walsh, J. Niehof, M. R. Collier, D. T. Welling, D. G. Sibeck, F. S. Mozer, T. A. Fritz, and K. D. Kuntz, “Density variations in the Earth’s magnetospheric cusps”, Journal of Geophysical Research: Space Physics **121**, 2131–2142 (2016).

[93] B. J. Wargelin, P Beiersdorfer, and G. V. Brown, “EBIT charge-exchange measurements and astrophysical applications”, Canadian Journal of Physics **86**, 151–169 (2008).

[94] B. J. Wargelin, M. Kornbleuth, P. L. Martin, and M. Juda, “OBSERVATION AND MODELING OF GEOCORONAL CHARGE EXCHANGE X-RAY EMISSION DURING SOLAR WIND GUSTS”, The Astrophysical Journal **796**, 28 (2014).

[95] B. J. Wargelin, M. Markevitch, M. Juda, V. Kharchenko, R. Edgar, and A. Dalgarno, “Chandra Observations of the “Dark” Moon and Geocoronal Solar Wind Charge Transfer”, The Astrophysical Journal **607**, 596–610 (2004).

[96] I. C. Whittaker, S. Sembay, J. A. Carter, A. M. Read, S. E. Milan, and M. Palmroth, “Modeling the magnetospheric X-ray emission from solar wind charge exchange with verification from XMM-Newton observations”, Journal of Geophysical Research: Space Physics **121**, 4158–4179 (2016).

[97] J. H. Zoennchen, J. J. Bailey, U. Nass, M. Gruntman, H. J. Fahr, and J. Goldstein, "The TWINS exospheric neutral H-density distribution under solar minimum conditions", Annales Geophysicae **29**, 2211–2217 (2011).

[98] J. H. Zoennchen, H. K. Connor, J. Jung, U. Nass, and H. J. Fahr, "Terrestrial exospheric dayside H-density profile at 3–15 R_E from UVIS/HDAC and TWINS Lyman-α data combined", Annales Geophysicae **40**, 271–279 (2022).

[99] J. H. Zoennchen, U. Nass, and H. J. Fahr, "Exospheric hydrogen density distributions for equinox and summer solstice observed with TWINS1/2 during solar minimum", Annales Geophysicae **31**, 513–527 (2013).

[100] J. H. Zoennchen, U. Nass, and H. J. Fahr, "Terrestrial exospheric hydrogen density distributions under solar minimum and solar maximum conditions observed by the TWINS stereo mission", Annales Geophysicae **33**, 413–426 (2015).

[101] J. H. Zoennchen, U. Nass, H. J. Fahr, and J. Goldstein, "The response of the H geocorona between 3 and 8 R_e to geomagnetic disturbances studied using TWINS stereo Lyman-α data", Annales Geophysicae **35**, 171–179 (2017).

[102] J. H. Zoennchen, U. Nass, G. Lay, and H. J. Fahr, "3-D-geocoronal hydrogen density derived from TWINS Ly-α-data", Annales Geophysicae **28**, 1221–1228 (2010).

Acknowledgements

Time flies so fast and seven years have passed since I threw open the door of our lab or the Experimental Astrophysics Laboratory at Tokyo Metropolitan University (TMU). I would not have been able to complete this thesis without much support from many people. I would like to express my gratitude here.

First and foremost, I would like to thank my supervisor, Dr. Yuichiro Ezoe. His guidance and encouragement made me grow a lot. I am about to leave my nest as a fledgling. I will never forget what I have learned from him. The last seven years will be food for my next voyage. I owe a debt of gratitude to my thesis committee members, Dr. Yoshitaka Ishisaki and Prof. Yutaka Fujita. Their helpful comments allowed me to raise the quality of this thesis. A fruitful discussion with Prof. Yoshizumi Miyoshi and Prof. Naoki Terada helped me pave the way for this research. Great thanks are due to Dr. Kumi Ishikawa for giving me a lot of basic preparatory knowledge of this field. I would like to offer my special thanks to Dr. Takaya Ohashi for his continued kindness even after retirement. I am so proud to receive my diploma with his name on it as "President of TMU." I would like to show my appreciation to Secretary Yuko Kawakami for processing an enormous amount of paperwork. I owe my gratitude to my co-workers, Dr. Masaki Numazawa, Kasumi Nakamura, Kazuma Takeuchi, Masaru Terada, Dr. Nozomi Nakaniwa, Maiko Fujitani, Dr. Ryota Hayakawa, Koji Nunomura, Ryota Asai, Yusuke Noda, Yohei Yamada, and my dependable juniors. My lab life with them was an irreplaceable time for me. Last but not least, my greatest appreciation goes to my parents for their great help and encouragement over a number of years.

This research was supported by Grant-in-Aid for Japan Society for the Promotion of Science Fellows Grant Number 19J20910.

Daiki ISHI

February 20, 2023